Theses and Dissertations

5-2014

Reconstructions at the Interface in Complex Oxide Heterostructures with Strongly Correlated Electrons

Benjamin Gray
University of Arkansas, Fayetteville

Reconstructions at the Interface in Complex Oxide Heterostructures with Strongly Correlated Electrons

Reconstructions at the Interface in Complex Oxide Heterostructures with Strongly Correlated Electrons

A dissertation submitted in partial fulfillment
of the requirements for the degree of
Doctor of Philosophy in Physics

by

Benjamin Gray
Wichita State University
Bachelor of Science in Physics, 2007
University of Arkansas
Master of Science in Physics, 2010

May 2014
University of Arkansas

This dissertation is approved for recommendation to the Graduate Council.

_____
Dr. Jak Tchakhalian
Dissertation Director

_____   _____
Dr. Laurent Bellaiche   Dr. Douglas Spearot
Committee Member   Committee Member

_____   _____
Dr. William Oliver III   Dr. Paul Thibado
Committee Member   Committee Member

Abstract

Strongly correlated oxides exhibit a rich spectrum of closely competing orders near the localized-itinerant Mott insulator transition leaving their ground states ripe with instabilities susceptible to small perturbations such as lattice distortions, variation in stoichiometry, magnetic and electric fields, etc. As the field of interfacial engineering has matured, these underlying instabilities in the electronic structure of correlated oxides continue to be leveraged to manipulate existing phases or search for emergent ones. The central theme is matching materials across the interface with disparate physical, chemical, electronic, or magnetic structure to harness interfacial reconstructions in the strongly coupled charge, spin, orbital, and lattice degrees of freedom. In this dissertation, we apply the above paradigm to cuprate-manganite and cuprate-titanate interfaces.

We examine ultrathin $YBa_2Cu_3O_7/La_{2/3}Ca_{1/3}MnO_3$ multilayers, where interfacial charge reconstruction modulates the distribution of charge carriers within the superconducting planes and thereby act as dials to tune through the cuprate doping phase diagram. The ultrathin nature of the cuprate layers allows the reconstructed states to be resolved free of a bulk admixture. The depleted carriers are observed to directly enter the CuO_2 planes. With increasing LCMO thickness, magnetic correlations are introduced, and coupling between interfacial Cu and Mn develops.

The reconstructions in spin and electronic degrees of freedom found in cuprate-manganite heterostructures are expected to completely mask all other competing interactions. To this end, $SrTiO_3$ is incorporated as a spacer material in cuprate-titanate multilayers to reveal the role of dimensionality, interlayer coupling, and broken translational symmetry. At the unit cell limit, a decrease in carrier concentration is found that directly correlates with underdoping from lost charge reservoir layers at the interface, while increased STO layer thickness is found to augment the carrier concen-

tration with the charge reservoir layers but has no effect on the doping within the superconducting planes. Also spectroscopic evidence for charge transfer across the interface between Cu and Ti is shown to support a recent theoretical prediction of pre-doping at the cuprate-titanate interface in response to a polar discontinuity at the interface.

Acknowledgements

I would like to begin by acknowledging my collaborators in the Artificial Quantum Matter Laboratory at the University of Arkansas. The advice and training of my fellow graduate student, Jian Liu, was instrumental in the early years of my graduate research. I always enjoyed hearing his unique perspective on physics and the world around us. As Jian passed the torch to me, my honor was to pass it on to Derek Meyers. Derek could always be trusted to see a project through to finish. I will miss are crucial meetings at the Waffle House. Misha Kareev's tireless dedication to the lab and his colleagues was an inspiration. His knowledge of heterostructure synthesis and incredible work ethic can always be counted on. Eun Ju Moon and I wrote several papers together, and I always enjoyed our discussion on physics and life. I would also like to acknowledge collaborations with Srimanta Middey and Xiaoran Liu.

The bulk of my research would have been impossible without the availability of modern synchrotron facilities. I am deeply indebted to the team at the 4-ID-C beamline of the Advanced Photon Source. In particular, I would like to think Dr. John Freeland for his support and collaboration on all of my projects.

I would also like to note the financial support of the Doctoral Academy and Raymond Hughes Graduate Fellowships. I am honored by the awards and thankful for the support.

Last, I would like to express my sincerest thanks to my advisor, Dr. Jak Tchakhalian. His greatest lesson to me was his boundless curiosity which pervaded all of our projects together. It was my distinct honor to be guided into the world of professional research by him.

Dedication

I dedicate this dissertation to my family, especially...

    to Ashley for her love and encouragement;

    to Xavier, Vincent, Gabby, and Sophia for their joy;

    to my dad and mom for their never-ending faith and support.

Contents

Chapter 1

Introduction

This chapter serves as an introduction into the field of transition metal oxide heterostructures. It begins with a review of the models which underly the basic physics of oxide materials from the simplistic ionic conventions of interacting charged, hard spheres to the Hubbard model of strongly correlated electrons. A review of the materials studied in this dissertation ($SrTiO_3$, $La_{2/3}Ca_{1/3}MnO_3$, and $YBa_2Cu_3O_7$) and their properties is included, as well. At the end, the field of correlated interfaces are discussed with an emphasis on the tools available to manipulate existing phases and search for emergent ones.

1.1 Correlated Oxides

1.1.1 Structural Themes in Transition Metal Oxides

Coordination Geometry

In transition metal oxides (TMOs), variations in structure originate in the underlying bonding interactions between metal and oxygen that stipulate the coordination geometry between them in the solid. TMOs are routinely thought to follow ionic structural conventions stemming from the large electronegativity of oxygen. In this regard, the arrangement of oxygen ligands around metal ions, which serves as a basis for the resulting structures, depends largely on the geometry of efficiently packing hard spheres with nonequivalent radii in agreement with Pauling's Rules. However, this naive model often fails, and consideration must be given to other factors such as partial-covalency, dispersive interactions, crystal field effects, etc.

For a strictly ionic model, bonding is modeled as electrostatic attraction between oppositely charged, incompressible spheres. Interatomic distances are approximated by the sum of ionic radii. Typically, the radii are extracted from empirical data through assumptions on the size of the anion. Values of ionic radii can be found in tables based on calculations by Shannon and Prewitt [1]. In TMOs, these often serve as a rough predictive tools, although caution must be exercised in their application. Ionic radii are sensitive to a number of factors competing factors: (1) Ionic radii depend sensitively on the oxidation state, decreasing with the loss of electrons. (2) Cation size tends to increase, when a rise in anion coordination naturally creates extra distance reducing short range repulsion. Anion radii have been shown to vary with coordination as well. (3) Partial covalency effectively shortens metal-oxygen bonds. (4) Crystal field effects can distort ligand geometry (e.g. Jahn-Teller effect). Modern tabulations of ionic radii attempt to incorporate many of these factors and more, however a universally applicable protocol has not been developed.

Given suitable radii, predictions on the kinds of coordination polyhedra likely to develop in a solid can be made. The simple procedure, termed the radius-ratio rules, is summarized in Figure 1.1. The polyhedron with the maximal coordination will form subject to maintaining cation-anion contact. This condition places limits on the ratio of cation radius (R_c) to anion radius (R_a) supported for a given polyhedron. As cation size decreases relative to the anion, the coordination drops down at the limiting ratios defined in the table. The lower limit in a given coordination is based on the geometrical requirements for perfect packing, i.e., anions just "kiss" each other while continuing to make contact with the cation. Below this ratio, anions impinge on each other or lose contact with the cation leading to a change in coordination. For common oxidation states of $3d$ transition metals, ionic radii range from 50 to 90 pm. Assuming an oxygen radius of 126 pm, octahedral coordination is expected and often observed.

However, lower coordinations and distorted octahedra are common as well. There are several
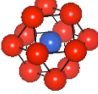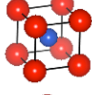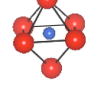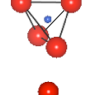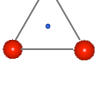
R_c/R_a	C. N.	Polyhedra	
1.0	12	Cuboctahedral	
0.732 - 1.0	8	Cubic	
0.414 - 0.732	6	Octahedral	
0.225 - 0.414	4	Tetrahedral	
0.155 - 0.225	3	Triangular	
< 0.155	1	Linear	

Figure 1.1: **Coordination polyhedra with corresponding radius-ratios.** The radius-ratio is defined as the ionic radius of the cation (R_c) divided by the ionic radius of anion (R_a). As cation size decreases, the coordination of anions around the cation must change to prevent anion-anion contact. This leads to ranges of radius-ratios over which different coordination polyhedra are stable. Coordination numbers and associated polyhedra are shown. Metal ions (blue) are displayed in different geometries with oxygen ions (red).

reason for this that show ions are in fact not hard spheres. Instead, observed distances stem from an equilibrium state of opposing forces. For instance, covalency leads to consolidation in the sharing of orbitals between different bonds that both strengthens and necessarily shortens them. Additionally, electron pair repulsion adds geometrical constraints to covalent bonds. In this way, partial covalency tends to lower coordination and distort octahedral symmetry. Another distortion significant to the subject matter of this dissertation is the Jahn-Teller effect, in which two opposing bonds are lengthened. This distortion stems from crystal field effects, and only occurs in select electron configurations (e.g., d^4 high-spin and d^9). These configurations are found in the materials used for this study, Mn^{3+} in $La_{2/3}Ca_{1/3}MnO_3$ and Cu^{2+} in $YBa_2Cu_3O_7$, respectively.

The Perovskite Family

TMOs display a diversity of complex crystal structures derived from the abundance of stable coordination geometries and the various means by which polyhedra can be linked to form metal-oxygen networks in the solid. One of the most common coordinations, octahedral, supports a number of technologically relevant oxide families, which are often characterized by the different possible connections between octahedra (see Figure 1.2). For the scope of this writing, we will only need to focus on one of the structurally simpler classes of corner-sharing ternary oxides, the perovskites.

The perovskite family inherited their name from the mineral calcium titanate $CaTiO_3$, which in turn is named after the Russian mineralogist L. A. Perovski. Any TMO adopting the same crystal structure as calcium titanate (see Figure 1.2(d) for ideal perovskite structure) belongs to this group. Perovskites are represented by the general chemical formula AMO_3, where A and M are cations. The A-site is 12-fold coordinated by oxygen neighbors, and the M-site sits inside the MO_6 octahedra, which form a corner-sharing network running throughout the crystal. Third row transition metals commonly inhabit the B-site, while the A-site, in keeping with the higher coordination, typically hosts larger cations (e.g., ionized alkaline earth and rare-earths elements).

The true beauty of the perovskites rest in the their ability to incorporate chemical and structural variations that necessitate distortions away from the ideal cubic lattice. In terms of ionic radii, the realization of a perfect cubic structure stipulates that $r_A + r_O = \sqrt{2}(r_M + r_O)$, where r_A, r_M, and r_O stand for the A, M, and O ions of the perovskite crystal. Clearly, perfect matching cannot be expected across the entirety of possible A and M cation pairs. The degree of distortion can be quantified in terms of the tolerance factor t.

$$t = \frac{r_A + r_O}{\sqrt{2}(r_M + r_O)} \tag{1.1}$$
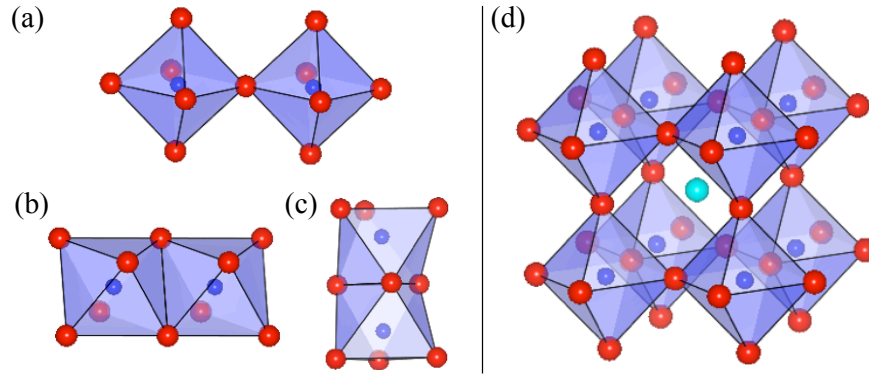
Figure 1.2: **Octahedral linkage and ideal perovskite structure.** **(a)** Binary oxides ReO_3 and a large number of ternaries such as the ABO_3 perovskites form corner-shared networks. This linking provides the greatest distance between cations increasing stability. **(b)** Monoxides typically configure into rock-salt structures, which demonstrate edge-sharing networks of octahedra. **(c)** M_2O_3 $3d$ oxides commonly take on the corundum structure, where octahedra form face-sharing networks. The close proximity of cations facilitates metal-metal bonding in some cases. **(d)** Ideal perovskite structure.

For $t = 1$, the ideal cubic structure is realized. Below 1, usually a series of cooperative tilts and rotations amongst the MO_6 octahedra distort the structure filling in the extra space between the A-site and oxygen ions. These octahedral rotations both lower the symmetry of the crystal structure and reduce the M-O-M bond angle from $180°$, which negatively impacts hybridization between O $2p$ and M $3d$ orbitals. The crystal symmetry is lowered in order from cubic ($Pm\bar{3}m$) to rhombohedral ($R\bar{3}$) to orthorhombic (Pbnm) to monoclinic ($P2_1/n$).

The adaptability of the perovskite structures to these deformations allow for: (1) the accommodation of a wide range of A and M cation pairs, (2) the possibility of mixtures of more than two types of cations, (3) ordered defects appearing within the perovskite structure, and (4) the manifestation of technologically important structural phase transitions (e.g. ferroelectricity). Several of these properties are essential to the electronic structure of the materials which are the subject of this dissertation and will be discussed more fully further on.

Cohesive Energy

While geometric considerations provide a useful guide to predicting the atomic arrangement of crystals, understanding the stability of these structures requires further examination. At first glance, it is not obvious that solid TMOs should form. The creation of both an ionized transition metal, M^{x+}, and O^{2-} are highly endothermic reactions. However, ionic solids contain positive and negative ions coupled by strong electrostatic interactions. This Coulomb energy provides the dominant contribution to the cohesive energy compensating for the energy required to form metal and oxygen ions.

To calculate the Coulomb contribution to the lattice energy (i.e., the potential energy of the crystal with all atoms at rest), we need to sum over the electrostatic interactions between all ions in the solid. The interaction between two ions i and j with charges Q_i and Q_j, respectively is given by equation 1.2.

$$U(r_{ij}) = \frac{Q_i Q_j}{4\pi\varepsilon_0 r_{ij}} \tag{1.2}$$

The sign of the interaction depends on the product of Q_i and Q_j, therefore non-convergence of the sum becomes problematic, unless the counting has been arranged carefully. This has led to the sum being defined in terms of Madelung potentials. For simple cubic structures, the Madelung Potential is given by equation 1.3,

$$U_{Madelung} = \frac{1}{2}\sum_{i,j} U(r_{ij}) = \alpha\frac{N_A Q_i Q_j}{4\pi\varepsilon_0 R} \tag{1.3}$$

where R is the nearest-neighbor cation-anion separation, N_A is Avogadro's number, and α is the Madelung constant. The Madelung constant is specific to a given crystal structure and does not depend on ion size or charge. Often the Madelung potential cannot be evaluated analytically except

for cases of high symmetry, instead numerical techniques typically based on Ewald summations are required. In general, Madelung energy increases in magnitude with packing efficiency in crystals, and this explains the preference to form structures with higher cation-anion coordination, which was an underlying assumption of the radius-ratio rules.

A cursory glance at equation 1.2 suggests that a full accounting of the lattice energy requires the introduction of additional terms. The Coulomb summation, taken by itself, compresses the crystal volume to the smallest possible value. This tendency is overcome by the repulsive interaction between electron orbitals of two impinging ions. The repulsive interaction is often parametrized with an exponential dependence, the Born-Mayer potential. At this point, the lattice energy can be accurately evaluated for most ionic crystals. As the Coulomb term becomes less dominant though, knowledge of dispersive interactions and partial covalency will be essential to properly model the lattice energy. It is possible to approximate them with Lennard-Jones and Morse potentials, respectively. However, a true understanding of covalent bonding necessitates a quantum mechanical interpretation. In this respect, physicist have developed a number of numerical tools based on tight-binding methods, and electron correlations can be included as well with modern density functional theory.

1.1.2 Electronic Structure

Ionic Potentials

TMOs lack conformity to any single picture of electronic behavior. An interpretation of their properties entails taking both a local view, focusing on the electronic states of individual ions, and a delocalized approach, considering the extended states formed by hybridization throughout their metal-oxygen networks. Conceptually, it is simplest to begin with the local view and then

progressively advance into the extended one. This will be the course of discussion for this section. At the end, both of these perspectives will be needed to explain one of the unconventional electronic states found in many oxides, the Mott insulator.

As stated earlier, oxides routinely follow ionic conventions. In this scenario, the $3d$ states do not hybridize and instead remain localized near the cation. Effectively, the cation only experiences an electrostatic field due to the other ionic charges in the solid. If only the monopole term is included, then the previously discussed Madelung potential defines the energy landscape between different electron excitations in oxides. These onsite potentials are exceeding large — on the order of tens of electron volts. Hence, the energy barrier to excite an electron between different atoms renders the highly ionic oxides insulating in nature, where the band gap is set by the charge transfer energy between electronic states on different ions.
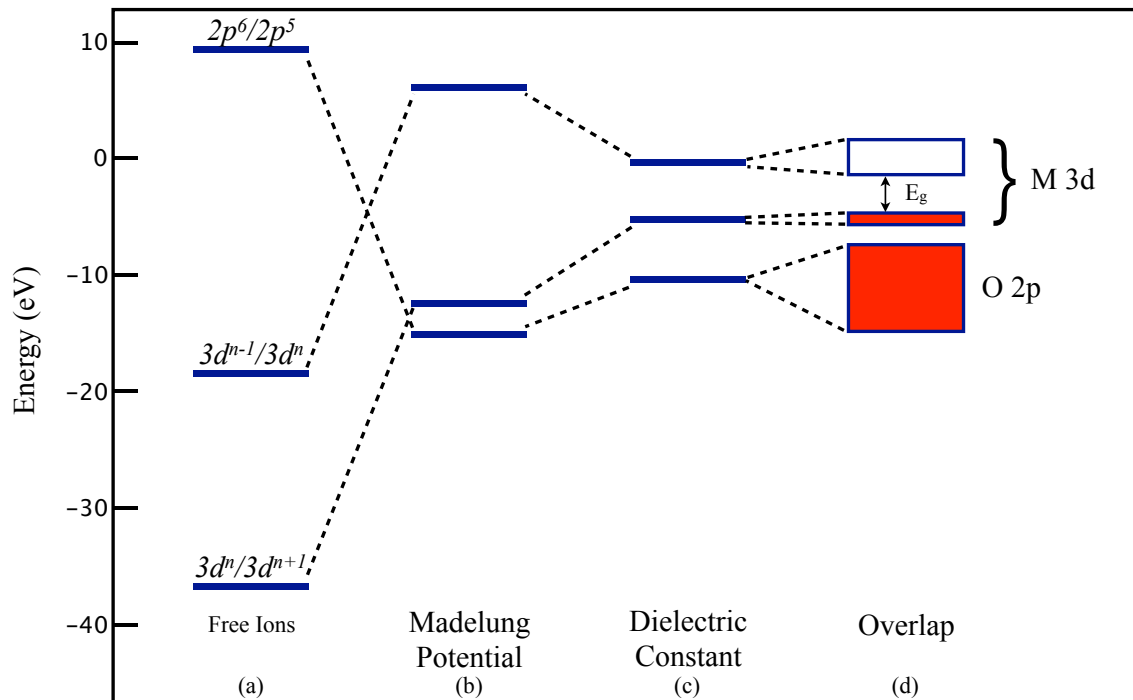
Figure 1.3: **Ionic model of hypothetical MO electronic structure.** **(a)** The energy levels of M and O free ions. **(b)** The shift in levels induced by the Madelung potential of the lattice. **(c)** Including the polarizability of the medium. **(d)** Broadening of levels due to hybridization. (Adapted from the NiO energy level diagram in reference [3].)

The energy level digram for a hypothetical transition metal monoxide MO (see Figure 1.3) helps illustrate these concepts [2]. Here, only the two most energetically favorable excitations are considered:

$$O^{2-}(2p^6) + M^{\nu+}(3d^n) \rightarrow O^-(2p^5) + M^{(\nu-1)+}(3d^{n+1}),$$ (1.4)

$$M^{\nu+}(3d^n) + M^{\nu+}(3d^n) \rightarrow M^{(\nu+1)+}(3d^{n-1}) + M^{(\nu-1)+}(3d^{n+1}).$$ (1.5)
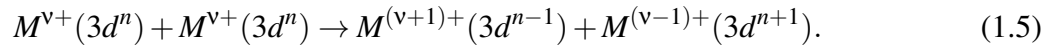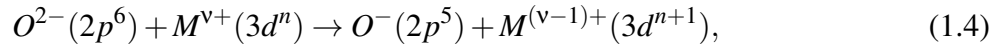
Equation 1.4 represents the removal of an electron from $2p^6$ and the placement of the same electron on a distant $3d^n$ site. Equation 1.5 shows the removal of an electron from $3d^n$ and the placement of the same electron on a $3d^n$ site far away in the crystal. (Transitions from possible defect levels have been ignored for simplicity.) To calculate the energetics of these transitions, first the free ion energies must be considered. The free ion energies can easily be obtained through tables of ionization energies and electron affinities. In Figure 1.3(a), the free ion energies have been plotted in a relative manner. The $2p^6$ state has been offset by placing the energy of $2p^5$ plus a free electron at zero. This is expressed as $2p^6/2p^5$. In the same manner, the $3d^{n-1}$ and $3d^n$ levels have been offset by $3d^n$ and $3d^{n+1}$, respectively. As mentioned, the ionization energies of a metal ion and the second electron affinity of oxygen are highly endothermic, and ionic crystals would simply fall apart, if not for the strong Coulomb attraction between the ions. Consequently, the energy levels of O^{2-} and the two different M ionizations are reduced and raised, respectively, by the Madelung potential. The resulting ionic version of the MO electronic structure is displayed in Figure 1.3(b). While insightful, this naive model requires requires modifications to better reflect the real physical situation. First, the transitions take place in the solid and are reduced by the dielectric constant of the medium (see Figure 1.3(c)). Also broadening of the electronic levels will occur with the formation of energy bands due to orbital overlap as shown in Figure 1.3(d). The completed energy level diagram reveals that the conduction and valence bands are of $3d$ orbital character, and the

band gap is derived from the second process (equation 1.5), in which an electron-hole pair is formed in the separated $3d$ band. Here, the O $2p$ band appears below the lower $3d$ band. The relative positions of these bands depends on the ionization energy of the metal ion. For higher ionization energies (found in the late transition metals), the O $2p$ band would be expected to appear between the separated $3d$ bands. This distinction underlies an important classification scheme in the physics of Mott insulators and will be discussed in more detail later on.

Crystal Field Theory

Up to now, the five $3d$ orbitals of the transition metals have been presented as degenerate, however this model is only valid in the case of a spherical symmetric potential. In other words, to lift the degeneracy higher-order terms of the electrostatic field must be included. This is the subject of crystal field theory in which the degeneracy of atomic orbitals is broken by a lowering in the symmetry of the local charge distribution. In this framework, the potential experienced by a transition metal ion stems from negative point charges, which represent the nearest neighbor oxygen anions. The exact nature of the orbital splitting depends crucially on the interaction between the spatially anisotropic $3d$ orbitals with the local charge symmetry.

The most commonly considered case is octahedral symmetry O_h (see Figure 1.4(a)). In this potential, the d orbitals are spit into two sets: the triply degenerate t_{2g} orbitals ($d_{x,y}$, $d_{x,z}$, and $d_{y,z}$) whose nodal planes face the O $2p$ orbitals and the doubly degenerate e_g ($d_{x^2-y^2}$ and $d_{z^2-r^2}$) with lobes pointing directly at the oxygen orbitals. The electrostatic repulsion from the O $2p$ electrons raises the energy of the e_g states with respect to t_{2g}. The energy separation between them is crystal field splitting, known as 10Dq.

Often transition metal ions have only partially filled $3d$ levels. In this case, the electrons present will fill the lowest lying energy levels first, and clearly occupation of the t_{2g} orbitals should be
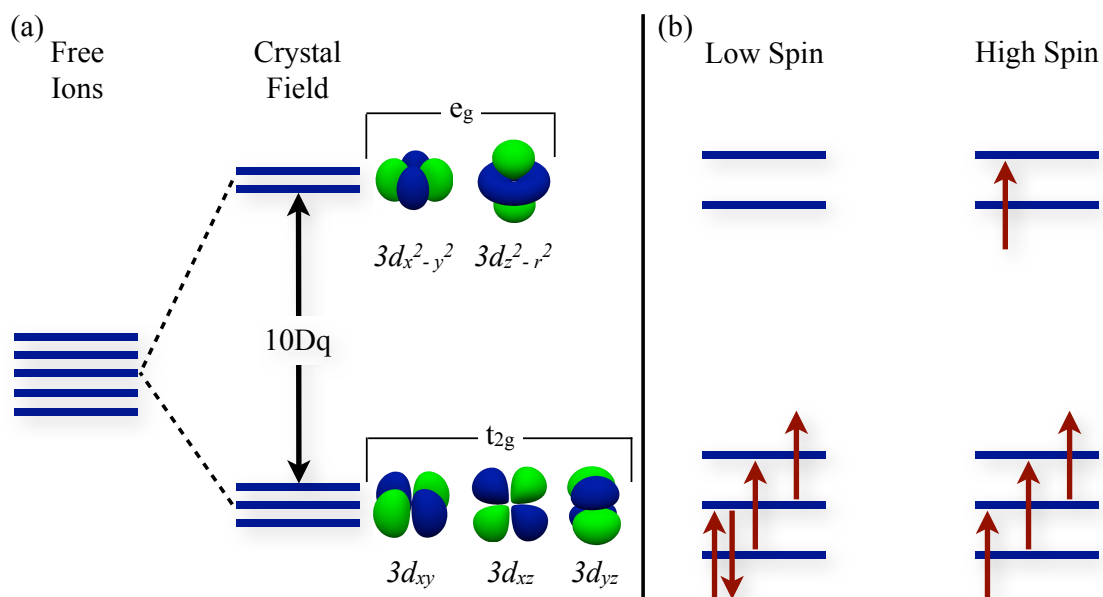
Figure 1.4: **Crystal field splitting in octahedral symmetry.** (a) The degeneracy of the five $3d$ orbitals is lifted in the oxo-ligand field. The orbitals split into an e_g doublet and a t_{2g} triplet below the e_g levels by the amount 10Dq. (b) Electronic configuration for the low and high spin cases of a $3d^4$ ion.

preferred. However, an interesting situation arises beyond the d^3 electron configuration. Here, the addition of an extra electron (i.e., a d^4 configuration) demands a choice between placing an electron in the same t_{2g} orbital as another electron or an unoccupied e_g orbital (see Figure 1.4(b)). The outcome depends on the relative sizes of the crystal field splitting and the Coulomb energy cost to place two electrons on the same orbital, the pairing energy. Two electrons occupying same orbital are required to have opposite spins according to Pauli's rule, and this necessitates a symmetric spatial wave function. Typically, the exchange constant, J_H (in reference to Hund's rules), is positive for two electrons on the same atom, and this situation would result in a Coulomb penalty. With these distinctions in mind, the system can take on two possible configurations, low or high spin. If the total pairing energy is less than the crystal field splitting (low spin state), then electrons will doubly occupy the lower energy t_{2g} orbitals first. In the reversed situation (high spin state), the electrons will first singly occupy all d orbitals starting with the lower energy orbitals

and then the higher energy e_g states. When more than one electron must choose between the high or low spin state, an intermediate case may result (e.g. trivalent cobalt).

Now that a procedure has been established to find the total spin quantum number S, an application of Hund's second and third rules should give the other angular momentum quantum numbers L and J. Here, L corresponds to the total orbital angular momentum, and $\mathbf{J} = \mathbf{L} + \mathbf{S}$. However, it is well known that the predicted values of the effective magnetic moment given by $2\mu_B\sqrt{J(J+1)}$ do not agree with experiment for $3d$ transition metal ions placed in crystal fields. The crystal field interaction quenches the angular orbital momentum $(L = 0)$, and hence $\mu_{eff} = 2\mu_B\sqrt{S(S+1)}$.

So far, consideration has been given only to the case of perfect octahedral coordination, which is a high symmetry crystal field with remaining degeneracies in the $3d$ orbitals. In lower symmetry anion distributions, the degeneracy of the orbitals can alomst be completely lifted. The removal of degeneracy through symmetry lowering is a common effect for a specific set of transition metal ions (e.g., Mn^{3+}), which are referred to as Jahn-Teller active. These ions possess electron configurations, where the spontaneous distortion of octahedron leads to a lower energy ground state. In Mn^{3+} ions ($3d^4$), the splitting of the two e_g orbitals allows for a reduction in the electronic energy
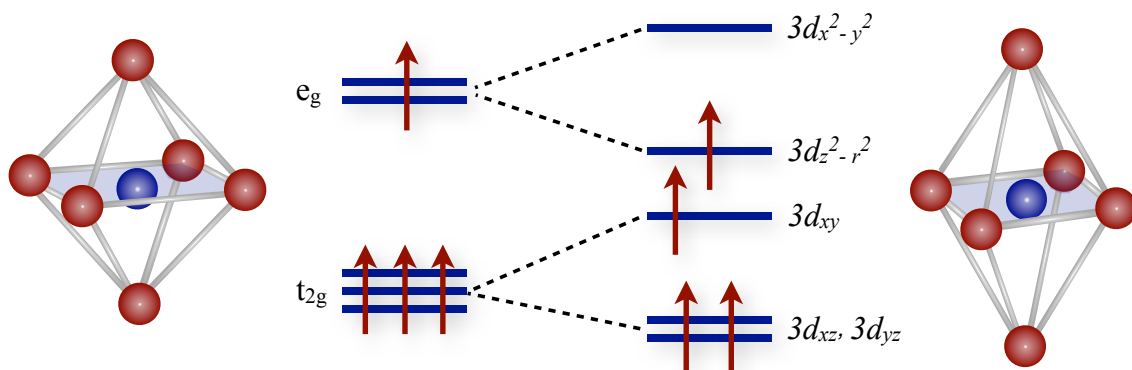
Figure 1.5: **Jahn-Teller Effect.** Elastic deformation of octahedra removes most of the remaining degeneracy in the e_g and t_{2g} states that leads to a lower energy electron configuration. The case of Mn^{3+} is shown. The singly occupied e_g level is now at lower energy, and the increase in $3d_{xy}$ state is exactly balanced by the decreases in $3d_{xz}$ and $3d_{yz}$.

(see Figure 1.5). Of course, this energy savings is balanced by the increase in elastic energy due to the deformation of the octahedra. If the lone e_g electron were not present such as in a Mn^{4+} ion ($3d^3$), then the energetics of the system would not favor a distortion.

Hybridization

The $3d$ orbitals of the first transition series, especially the later elements, have highly contracted and core-like spatial distributions. In this regard, hybridization between them and oxygen $2p$ orbitals is minimal which justifies the use of the ionic model outlined above. However, a finite degree of overlap prevails, and the resulting covalent bonding allows electrons to hop or resonate between different ions. In an MO_6 octahedra, symmetry determines the mixing between metal and oxygen orbitals, which requires the construction of symmetry adapted linear combinations of oxygen orbitals. (For a more detailed discussion see reference [3].) In short, the e_g orbitals hybridize with
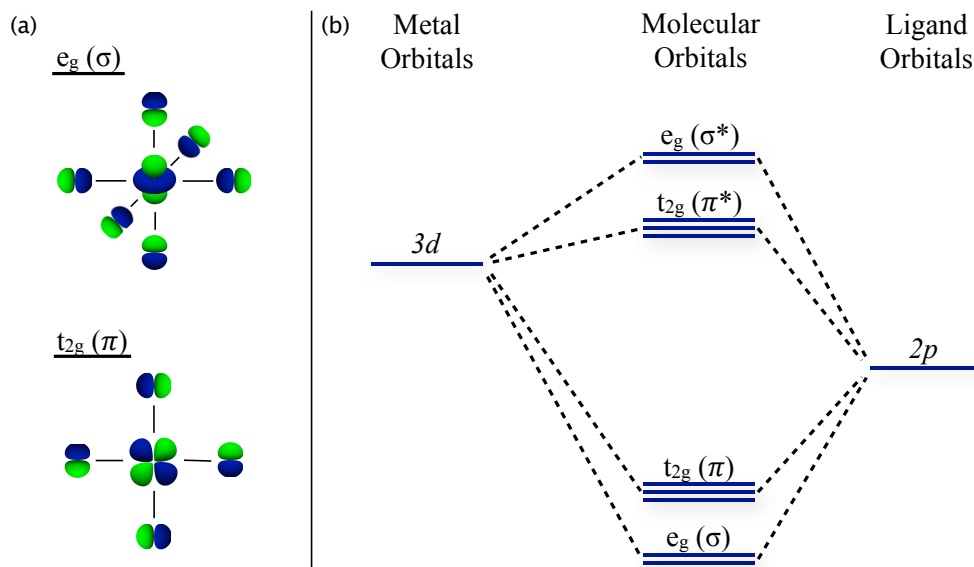
Figure 1.6: **Formation of molecular orbitals in MO_6 octahedra.** (a) Bonding combinations (in-phase) between the metal $3d_{z^2-r^2}$ and oxygen $2p$ orbitals. The e_g orbitals only form σ bonds ($3d_{x^2-y^2}$ not shown). Also bonding combinations (in-phase) between the metal $3d_{xz}$ and oxygen $2p$ orbitals. The t_{2g} orbitals only form π bonds (other t_{2g} orbitals not shown). **(b)** Molecular orbital diagram for an MO_6 complex with octahedral symmetry. The atomic orbitals of the transition metal and oxygen ions hybridize to form molecular orbitals.

O $2p$ orbitals forming σ bonds, where the lobes point along the metal-oxygen bond direction (see Figure 1.6(a)). The t_{2g} states form π type bonds with the lobes pointing in a perpendicular direction. The covalent bonding between orbitals can be in-phase or out of phase depending on the sign of the wavefunction. This results in bonding (denoted σ or π) and anitbonding (σ* or π*) states, respectively, with the latter occurring at a higher energy.

For a lone MO_6 octahedron, these hybridized states are considered molecular orbitals of the combined nuclei (see Figure 1.6(b)). In molecular orbital theory, the new states are expressed through a linear combination of the atomic orbitals (LCAO) and take the form

$$|\psi_n\rangle = c_i^n |\phi_i\rangle, \tag{1.6}$$

where $|\phi_i\rangle$ represent an appropriate basis of valence atomic orbitals, and the Einstein summation convention has been used. The eigenvalues ε_n and the coefficients c_i^n are obtained by solving the Schrödinger equation

$$(H_{ij} - \varepsilon_n S_{ij})c_i^n = 0. \tag{1.7}$$

H and **S** are the Hamiltonian and the overlap matrix, respectively, expressed in the atomic orbital basis. Since the atomic orbitals states of the metal and oxygen ions are not orthogonal, **S** will contain off-diagonal elements.

For partially ionic systems, the molecular orbitals can be treated as perturbations of the atomic orbitals due to the large energy separation between the M $3d$ and O $2p$ states, i.e. that is the amount of intermixing between atomic orbitals varies inversely with energy separation, but directly with the amount of overlap. Thus, the bonding states contain a greater degree of O $2p$ character, and the anitbonding states are assigned to the M $3d$ orbitals. Due to the preferential formation of stronger σ bonds in the e_g states versus weaker π bonding in the t_{2g} orbitals, the e_g orbitals feel a stronger

perturbation, and the crystal field splitting is enhanced.

In the solid, MO_6 octahedra link together forming a metal-oxygen network, in which the bonding and antibonding states delocalize throughout the periodic framework forming dispersive bands in place of σ, π, σ^*, and π^* molecular orbitals. The bandwidth W is directly proportional to the transfer integral $t_{pd} = \langle \phi_M | H | \phi_O \rangle$, which gives a measurement of the ease with which an electron can be transferred from a metal to an oxygen site. Small transfer integrals lead to narrow bands (large effective masses). In this way, the TMO bands reflect the atomic orbital character of the $3d$ transition metal states which make them up. These contracted (small radial extension compared to lattice spacing) and anisotropic orbitals typically yield narrow bands with complicated structures. Also, the interaction between metal sites occurs indirectly via hybridization with oxygen further narrowing the bands. Thus tight-binding models constructed from atomic Wannier orbitals are the best first approximations.

Mott Insulators

In band theory, insulators are differentiated from metals through the filling level of the highest occupied band. Each band in the Brillouin zone contains twice (spin degeneracy) as many electronic states, as there are primitive unit cells in the lattice. When the valence electron count is even, an integer number of bands are filled up to a band gap, and the fermi level sits in-between the conduction and the valence band. The vanishing density of states at the Fermi level results in an insulator. For an odd count the highest occupied band is only partially field, and density of states at the Fermi level is non-zero resulting in a metallic system. Under this paradigm, making an assignment of metal or insulator to any given material appears to be a trivial task of counting valence electrons. However, in 1937 it was realized that this model failed to correctly predict the ground state of many transition metal monoxides. The deviation from conventional band theory

15

stems from a violation of its underlying assumptions: electrons are independent interacting with only a static periodic potential. The narrow bands and low conduction electrons concentrations typical of TMOs diminish electron-electron screening strengthening electron correlations.

Incorporating electron correlations into the formalism remains a complex and continuously evolving field within condensed matter physics. Although a key simplification can be drawn from the ionic model. In the earlier MO energy level diagram, the band gap corresponded to the energy needed to excite a d-electron from one metal site to another ($d^n + d^n \rightarrow d^{n-1} + d^{n+1}$). Including only on-site electron repulsion U, the Hubbard Hamiltonian can be written as

$$H = -t \sum_{\langle ij \rangle} c_{i\sigma}^{\dagger} c_{j\sigma} + U \sum_i \left(n_{i\uparrow} - 1/2 \right) \left(n_{i\downarrow} - 1/2 \right) - \mu N, \qquad (1.8)$$
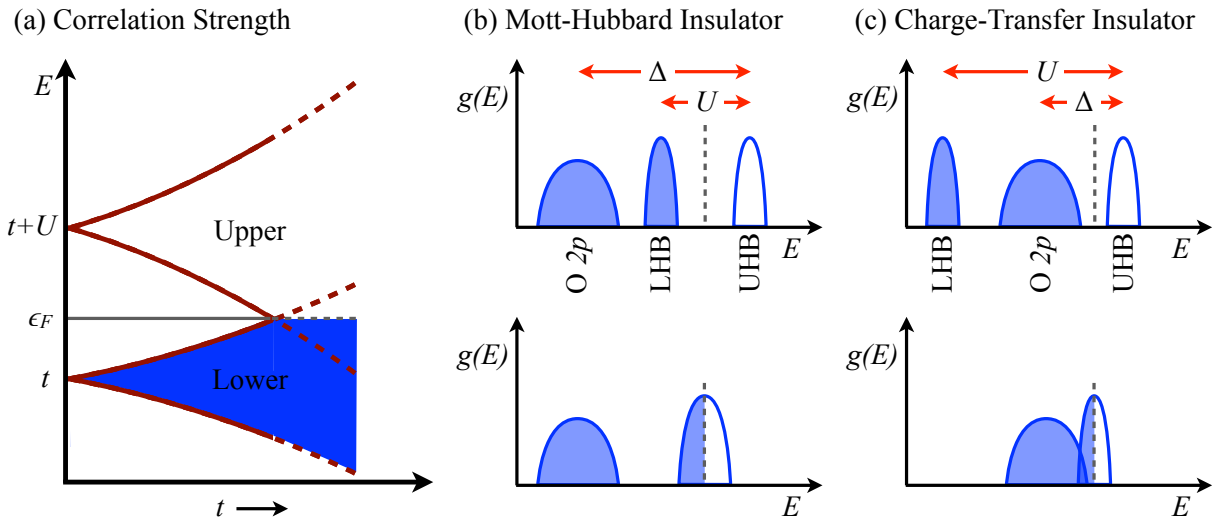
Figure 1.7: **Mott Insulator.** **(a)** Transition from localized to itinerant behavior in the Hubbard model. Lower and upper Hubbard bands (LHB and UHB) cross, when the band width W exceeds the electronic repulsion U resulting in a partially filled band. **(b)** Energy level diagrams (schematic) for a Mott-Hubbard insulator ($U < \Delta$). Top: LHB and UHB separated by U yielding an insulating state. Bottom: BC-MIT resulting in one partially filled band. **(c)** Energy level diagrams (schematic) for a Charge-Transfer Insulator ($\Delta < U$). Top: The O $2p$ band sits in-between the Hubbard bands. The system is insulating due to the charge gap Δ. Bottom: The oxygen band and UHB overlap yielding a metallic state. Adapted from references [4, 5]

where $c_{i\sigma}^{\dagger}$ ($c_{i\sigma}$) is the creation (annihilation) operator for a single-band electron at site i with spin

σ, and the number operator $n_{i\sigma} = c_{i\sigma}^{\dagger}c_{i\sigma}$. The first term captures the hopping between nearest

neighbor sites, while the second represents the Coulomb price U for double occupation of a single

site. The band filling is controlled by the electron density $n = N/L$, where N is the total number

of electrons and L is the number of lattice sites. In a non-degenerate band, the $n = 0$ and $n = 2$

fillings correspond to Bloch-Wilson insulators as expected from traditional band theory. At half-

filling ($n = 1$), the electron correlation strength U/t drives the system from localized to itinerant

(see Figure 1.7(a)). In the limiting cases, the Hubbard model is exactly solvable. For $U/t \ll 1$, the

problem reduces to a free Fermi-gas. For $U \gg t$, there is minimal coupling between lattice sites.

Double occupation of a lattice site will require energy $t + U$, while single occupation only requires

t. In this limit, the electrons will be localized with each site singly occupied.

At some intermediate state of U/t, the ground state of the Hubbard model should undergo

a metal-insulator transition (MIT). Consider a system with a controllable lattice constant, where

every site is singly occupied in an antiferromagnetic ground state. An additional electron can only

be accommodated at the $N/2$ lattice sites with opposite spin by the Puali exclusion principle. The

$N/2$ sites, which accept the extra electron, form the upper Hubbard band centered at $t + U$, while

the remaining $N/2$ sites form the lower Hubbard band centered at t. The bandwidth $W = 2zt$

(z is the number of nearest neighbors) is adjusted by the lattice spacing. At $U/W \sim 1$, the gap

will disappear, and the system crosses over from localized to itinerant behavior. This transition

is referred to as a bandwidth control (BC)-MIT. A second type of MIT is possible, when the

electron filling n takes a non-integer value. Consider an antiferromagnetic parent compound near

the $n = 1$ filling level as before. Removing an electron from a lattice site (carrier-doping), frees up

a low energy excitation that allows electrons to propagate through the lattice without paying the

interaction energy U. This is known as a filling controlled (FC)-MIT. For a thorough review see
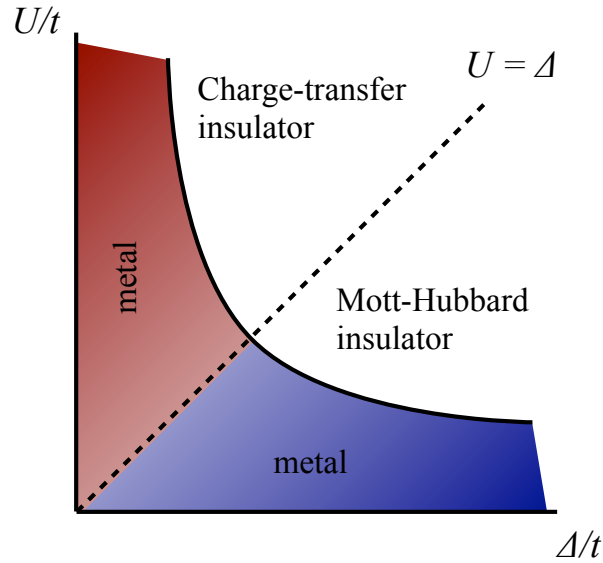
Figure 1.8: **ZSA diagram.** In the ZSA classification scheme, charge-transfer and Mott-Hubbard insulators are separated out by the relative strength of the interactions U/t and Δ/t. When the hopping integral, t, is relatively strong (e.g., $U < \Delta$ and $U/t \ll 1$), the bandwidth, W, bridges the gap, and metallization occurs.

references [4, 5].

Until now, only transitions between the lower and upper Hubbard band have been considered, however these are not always the lowest energy excitations in the system. This distinction depends on the relative sizes of U and the charge-transfer energy Δ which is the energy required to transfer an O $2p$ electron to a metal site ($3p^6 + 3d^n \rightarrow 2p^5 + 3d^{n+1} \equiv 3d^{n+1}\underline{L}$). Thus, Mott insulators are broken into two categories: Mott-Hubbard and charge-transfer. In Mott-Hubbard insulators ($\Delta > U$), the band gap forms between the lower and upper Hubbard bands (see Figure 1.7(b)), as discussed earlier. For charge-transfer insulators ($\Delta < U$), the fully occupied broad O $2p$ band sits in-between the lower and upper Hubbard bands (see Figure 1.7(c)). A convenient way to summarize the two different Mott insulators and their relationships' to the parameters of the Hubbard model is the Zaanen-Sawatzky-Allen (ZSA) diagram [6]. As mentioned before, the light and heavy transition metal compounds differ by the distance between the levels of their metal $3d$ and oxygen $2p$ orbitals. As the nuclear charge increases, the chemical potential of the d electrons moves lower

18

and closer to the p orbitals. Thus charge-transfer types are typical of the late transition metals (e.g., Ni and Cu). For small values of Δ the charge gap closes (see Figure 1.7(c)). In contrast to the Mott-Hubbard types, the oxygen p band strongly hybridizes with the $3d$ band at the Fermi level. The formal valence of oxygen deviates from O^{2-}, as $2p$ electrons move to d sites creating ligand holes, which is known as self doping. Since the ground state consists of itinerant $2p$ holes as well, the wavefunction is best described by a configuration interaction $\Psi = \alpha\Psi(d^n) + \beta\Psi(d^{n+1}\underline{L})$.

1.2 Closed Shell Oxide Insulators: SrTiO$_3$

1.2.1 Crystal Structure

Under standard ambient conditions, SrTiO$_3$ (STO) crystallizes in the ideal cubic perovskite structure, space group *Pm3m*. The lattice parameter, $a = 3.905$ Å, closely matches in-plane parameters for La$_{2/3}$Ca$_{1/3}$MnO$_3$ and YBa$_2$Cu$_3$O$_7$ producing low epitaxial strain $\varepsilon = \frac{a_{substrate} - a_{film}}{a_{film}}$ of ~ 1 % in heterostructures, where a_{film} means the original unstrained parameter of the film material. The coordination geometry consists of tetravalent Ti ions sixfold coordinated by O^{2-} ions forming a corner-shared network of TiO$_6$ octahedra. Sr^{2+} ions, each coordinated by 12 O^{2-} ions, fill the remaining empty space in the lattice efficiently resulting in an ideal cubic structure (tolerance factor $t = 1$) . Bonding, in STO, is mostly ionic in character with strong partially covalency between O $2p$ and Ti $3d$ states [7].

Upon cooling, STO undergoes a series of thermodynamic phase transitions [8, 9]. Between 110 - 65 K, the lattice symmetry lowers to tetragonal (space group *I/4mcm*), as neighboring octahedra rotate against each other continuously with temperature T. Near 55 K an order-disorder transition on the Sr site sets in lowering the symmetry further to orthorhombic. A possible low temperature and low symmetry phase may exists below 10K. Further deviations from the ideal cubic structure

can occur upon cation doping or large fluctuations in oxygen stoichiometry.

1.2.2 Electronic Structure

The electronic properties of STO are representative of d^0 TMOs. In the ionic limit, Ti atoms in STO lack $3d$ electrons meaning correlations are largely insignificant. The closed shell configuration naturally leads to a conventional band theory approach, and indeed STO is a strong band insulator with a gap of 3.2 eV [10, 11, 12]. The valence band is composed of mostly O $2p$ states, while the bottom of the conduction band is formed by empty Ti $3d$ orbitals. The octahedral environment divides the $3d$ states into t$_{2g}$ and e$_g$ as expected. In general, cations, occupying the A-site, only indirectly affect the electronic structure through ionic radius variations that modify the M-O-M bond angles influencing the bandwidth W.

Conductivity in STO can be manipulated through extrinsic doping of the A- and B-sites or intrinsic defect formation, typically oxygen vacancies. A-site substitution (e.g., Nb^{5+} and La^{3+}) and oxygen vacancies result in n-type conductivity, in which electronic states are filled at the bottom of the conduction band. For carrier densities between 10^{19} and 10^{21}, a superconductor transition occurs for Nb-doped STO and non-stoichimetric SrTiO$_{3-x}$ [13, 14]. B-site doping with Sc^{3+} introduces holes into the valence band, and p-type conductivity has been observed [15].

1.3 Colossal Magnetoresistive Manganites: La$_{2/3}$Ca$_{1/3}$MnO$_3$

1.3.1 Crystal Structure

The mixed valence manganites, for this work specifically the La$_{1-x}$Ca$_x$MnO$_3$ series, adopt the perovskite crystallographic structure. The parent compound LaMnO$_3$ crystallizes in the highly distorted O$'$-type orthorhombic structure (space group *Pbnm*) with $a = 5.54$ Å, $b = 5.75$ Å, and

$c = 7.70$ Å, where the Mn-O-Mn bond angle decreases to $155°$. While the misfitting La cations necessitate the buckling of the MnO_6 octahedra network corresponding to a cooperative rotation which lowers the symmetry to orthorhombic, the Jahn-Teller active Mn^{3+} ions facilitate further distortions in the octahedra that create a pattern of long and short Mn-O bonds in the ab-plane (orbital ordering) [16]. With A-site substitution of Ca for La, both the tolerance factor and Mn valence increase. $La_{2/3}Ca_{1/3}MnO_3$, the material used in this dissertation, sits on the orthorhombic side (space group *Pbnm*), near the edge of the O-type orthorhombic to rhombohedral (space group $R\bar{3}c$) transition ($t < 0.92$) [17, 18]. This distinction is critical, since cooperative-long-range Jahn-Teller distortions are not supported by rhombohedral symmetry (i.e., the rhombohedral crystal field does not split the e_g oribtals). Only localized Jahn-Teller distortions have been observed for samples within the rhombohedral phase (Sr-doped manganites). The lattice constants, for the orthorhombic phase, can be given in terms of the pseudo-cubic perovskite constant $a_p = 3.876$ Å with $a \approx b \approx \sqrt{2}a_p, c = 2a_p$. The end member of the series $CaMnO_3$ forms with orthorhombic symmetry as well, although the Mn^{4+} ion lacks the occupational degeneracy required for Jahn-Teller activity.

1.3.2 Electronic Structure

End Members (La,Ca)MnO$_3$

Much of the essential physics of the mixed valence manganites can be obtained from the local picture, where the interaction between formally $3d^4$ and $3d^3$ electronic configurations of the two distinct Mn ions host of a rich diversity of phenomena. Although, it is instructive to first consider both unique configurations separately, which can be facilitated through a discussion of the end members of the series, $LaMnO_3$ and $CaMnO_3$. As discussed earlier, manganese ions generally

favor the high spin state, when the *d* orbitals are split by a crystal field of oxygen ligands. For LaMnO$_3$, this gives t$_{2g}^{3\uparrow}$e$_g^{\uparrow}$, where the lone electron in the e$_g$ orbital is unstable against Jahn-Teller distortion (see Figure 1.5). A strong static, cooperative Jahn-Teller distortion distorts the lattice, which results in orbital ordering as mentioned previously. In CaMnO$_3$ with a t$_{2g}^{3\uparrow}$ configuration, such a distortion does not change the center of gravity of the t$_{2g}$ levels and consequently is not present. In terms of hybridization, the overlap between the t$_{2g}$ and O 2p orbitals is relatively small resulting in poor π-hybridization, while the e$_g$ orbitals overlap directly forming a σ^* anitbonding band. In this regard, the t$_{2g}^{3\uparrow}$ core can be viewed as a local spin ($S = 3/2$).

Both end members display vanishing density of states near the Fermi level, but the exact nature of the gap remains controversial [19, 20, 21]. The early and late transition metals are often categorically classified as Mott-Hubbard or charge transfer insulators, respectively, however the intermediate manganites are a borderline case with $U \simeq \Delta$. For LaMnO$_3$, conflicting reports have been given on the relative size these two interactions leading to further confusion. Also band structure calculations have suggested that neither model may apply. Instead, the Fermi level falls in the gap between the two Jahn-Teller split e$_g$ bands yielding a Bloch-Wilson insulator from conventional band theory. This controversy extends to CaMnO$_3$, as well. Core level spectroscopies have shown that the lowest-energy excitations in CaMnO$_3$ involve $d_i^n + d_j^n \rightarrow d_i^n \underline{L} + d_j^{n+1}$ transitions [23], while first principle calculations suggest that the Mn d-band is exchange split with occupied majority and unoccupied minority t$_{2g}$ states separated by a gap only traversable by spin-flip transitions [24].

Magnetic ordering in the end members is determined by the sign of the superexchange interaction. In TMOs, direct exchange is typically unimportant due to the small amount of orbital overlap between distant magnetic orbitals, instead the exchange interaction occurs indirectly through an intermediary oxygen ion. This long-range exchange interaction is termed superexchange. Similar

to direct exchange, superexchange is an electrostatic interaction that arises due to the kinetic energy advantage of delocalized electrons. Since the interaction occurs through an intermediary, the process is accurately described by second-order perturbation theory. A general result of second-order perturbation theory is that the perturbation energy is the square of the transition probability amplitude (matrix element) divided by the energy difference between the ground and excited state. For the case of two transition metal ions each with a single unpaired electron in the same non-degenerate orbital, this results in the exchange integral $J \sim -t^2/U$. Therefore, the excited states decreases the energy by realizing an antiferromagnetic coupling. Ferromagnetic coupling is possible, when electron transfer is from a half-filled to an empty orbital or from a filled to a half-filled orbital. Together the above guidelines constitute the Goodenough-Kanamori (GK) rules for superexchange [25, 26].

An application of the GK rules to the $t_{2g}^{3\uparrow}$ electron configuration of $CaMnO_3$ yields a G-type antiferromagnet, where both the inter- and intra-plane coupling are antiferromagnetic. $CaMnO_3$ does, in fact, take this magnetic ground state. $LaMnO_3$, on the other hand, assumes an A-type antiferromagnetic ground state, in which the ab-plane (out of plane) exchange J_{ab} (J_c) is ferromagnetic (antiferromagnetic) with the total moment vanishing [27]. The anisotropy in the magnetic ground state originates from the orbital ordering frozen into the system by the Jahn-Teller distortion of the octahedra. In the absence of Jahn-Teller splitting, the quarter-filled e_g orbitals would dominate exchange, and a ferromagnetic ground state is expected. The orbital polarization dramatically lessens the e_g states contribution to J_c, and the sign of exchange switches to antiferromagnetic [28].

Mixed Valency and Double Exchange

With A-site subsitution in the $La_{1-x}Ca_xMnO_3$ series, the Mn ion exhibits mixed valency (i.e, a portion x of the Mn ions are tetravalent and $1 - x$ are trivalent). The result is a heterogeneity
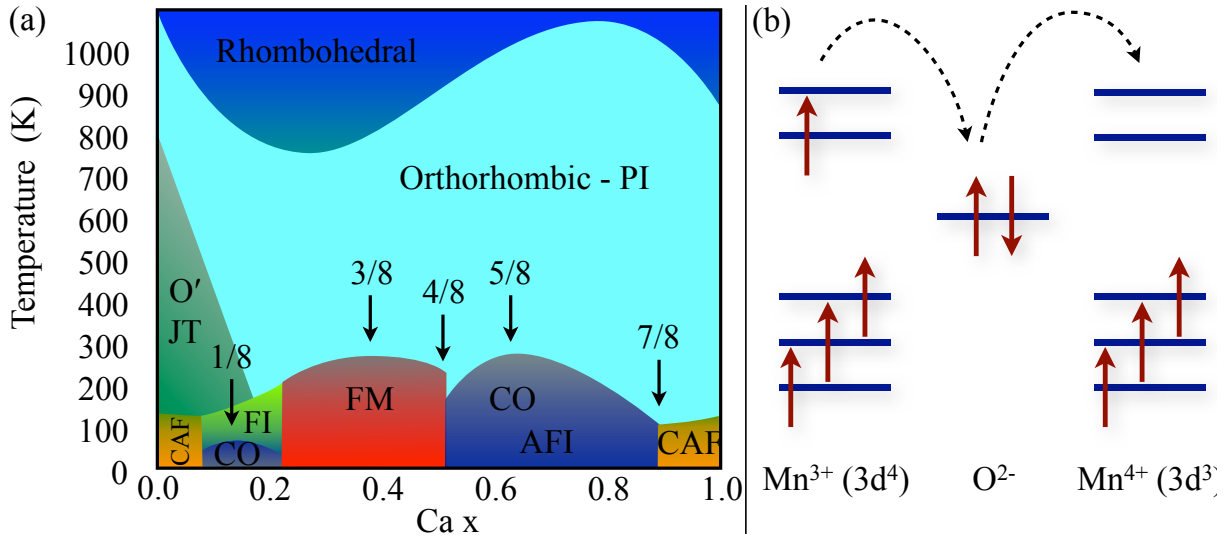
Figure 1.9: **$La_{1-x}Ca_xMnO_3$ phase diagram and mechanism of double exchange. (a)** The phase diagram of $La_{1-x}Ca_xMnO_3$ adapted from reference [29]. A rhombohedral to orthorhombic structural transition occurs at ~800 K regardless of the Ca doping content. A static Jahn-Teller distortion lowers the symmetry further for low levels of Ca doping. The magnetic and electronic grounds state are given for the entire range. **(b)** The double exchange mechanism between two Mn sites facilitated by an intermediary oxygen ion. The itinerant e_g electron only hops to an empty site, where the $t_{2g}^{3\uparrow}$ core is in parallel alignment (i.e. spin-flip transitions are energetically unfavourable).

of ground states over the full doping range (see Figure 1.8(a)) [30, 31, 32, 33]. At temperature above ~800 K, the lattice is rhombohedral over the entire doping series. Below, an orthorhombic distortion develops with additional Jahn-Teller activity at higher concentrations of Mn^{3+}. Near the parent compound $LaMnO_3$ canted antiferromagnetism develops as a result of nanoscale phase separation[33]. Charge ordering ground states can be found on both sides of the ferromagnetic metal phase. Here, interatomic Coulomb interactions localize the potentially mobile e_g electrons on Mn sites forming a regular lattice. Charge ordering occurs at rational fractions of x, when the Coulomb interactions become comparable to the bandwidth. Towards the high end of Ca doping ($x > 0.5$), various forms of antiferromagnetism develop.

Of primary interest is the ferromagnetic metal phase occurring over the narrow window from $0.17 \leq x \leq 0.5$ with the highest Curie temperature (~260 K) at a rational doping of $x = 3/8$.

To explain the ferromagnetic metal ground state, Zener considered exchange between Mn^{3+} and Mn^{4+}, where the simultaneous transfer of an electron from Mn^{3+} to oxygen and from oxygen to the nearest neighbor Mn^{4+} takes place (see Figure 1.8(b)) [34]. This transfer is known as double exchange, and unlike superexchange is always ferromagnetic and requires the transfer of real, not virtual, electrons. The hopping to an empty neighboring site proceeds without spin-flipping. There will be a strong on-site exchange between the itinerant e_g electron and the $t_{2g}^{3\uparrow}$ core which will result in the parallel alignment of spins. Ferromagnetic alignment maintains the high spin state on each site. Clearly, there is a direct correlation between conductivity and ferromagnetism. Extended parallel spin alignment allows the e_g electron to hop throughout the lattice. This kinetic energy savings achieves a corresponding increase in electron bandwidth.

Colossal Magnetoresistance

Near the Curie temperature, an exceedingly large magnetoresistive effect occurs, i.e., the resistance changes by orders of magnitude in response to an external magnetic field. This can be explained, in part, as a consequence of double exchange, which must be further generalized from the description above to include general spin directions [35]. Here the transfer integral becomes $t = t_0 \cos(\theta/2)$, where θ is the angle between the two spin directions, and the term $\cos(\theta/2)$ comes from the spin wavefunction. Since, the hopping probability is proportional to $|\cos(\theta/2)|$, an external magnetic field will align spins between neighboring ions increasing the electron bandwidth and subsequently the conductivity. This effect will be strongest near T_c, where the spins are not completely aligned. However, recent theoretical works have shown that double exchange alone is not enough to explain the magnitude of the magnetoresistive effect [36], instead an electron-phonon coupling term must be included. The coupling occurs as a result of the Jahn-Teller distorted Mn^{3+} octahedra, where polarons (electrons which move through the lattice essentially dragging large lattice distortions)

are formed in the paramagnetic insulating phase above the Curie Temperature. These polarons are magnetic and frozen into the lattice, until the transition to the ferromagnetic state unbinds them. Despite these efforts, the magnetic transport behavior of the manganites still remains an open question. Other competing models incorporate percolative transport through ferromagnetic domains in an electronically phase separated medium to explain the dramatic change in resistance [37].

1.4 High-T$_C$ Cuprates: YBa$_2$Cu$_3$O$_{7-\delta}$

1.4.1 Crystal Structure

Quickened by the promise of room temperature superconductivity there has been a rapid proliferation in the number of structures belonging to the class of High-T$_C$ cuprates, which began in 1986 with the discovery of transition temperatures around 30 K in the La-Ba-Cu-O system [38]. These structures can be divided roughly into three main families: La$_{2-x}$A$_x$CuO$_4$ (A = Ca, Sr, Ba), LnBa$_2$Cu$_3$O$_{7-\delta}$ (Ln = rare-earth element), and Bi$_2$(Ca, Sr)$_{n+1}$Cu$_n$O$_{2n+4}$ [39]. Compounds containing Tl and Hg might warrant a separate classification but share many similarities with the Bi cuprates. All cuprates retain the categorical feature of quasi-2D CuO$_2$ superconducting planes, while the cation structure, in which the superconducting planes are embedded, varies significantly amongst the families. The CuO$_2$ planes form a corner connected square lattice composed from distorted CuO$_6$ octahedra, CuO$_5$ pyramids, or simply CuO$_2$ square planes depending on the specific material. When apical oxygen ions are present (i.e., a higher coordination than square planar), the out of plane Cu-O bonds stretch deforming the coordination complex in response to the Jahn-Teller activity of the degenerate e$_g^3$ electron configuration of divalent Cu, which provides quasi-two-dimensionality. The square lattice naturally imposes tetragonal symmetry on most of

the cuprates, however some cuprates crystallize with a slight orthorhombic distortion, which is often the result of varying the dopant concentration. For a thorough review of the structural aspects of the cuprates see reference [40], as the remainder will focus on $YBa_2Cu_3O_{7-\delta}$

$YBa_2Cu_3O_7$ (YBCO) crystallizes in an oxygen deficient perovskite structure, where tripling along the c-axis occurs due to the Ba-Y-Ba ordering of the A-site (see Figure 1.9(a)). The lattice is orthorhombic (space group *Pmmm*) with lattice parameters $a = 3.828$ Å, $b = 3.888$ Å, and $c = 11.65$ Å. Two main structural units are readily apparent: the layered CuO_2 planes and the CuO_3 chains comprising the infinite layer (IL) and charger reservoir (CR) blocks, respectively. The electronically and structurally distinct Cu sites of these two blocks are a unique feature of the $LnBa_2Cu_3O_{7-\delta}$ family.

The CR blocks function as the source of holes for the superconducting planes, and the adjustable coordination of the Cu(1) site in the chains facilitates this role. For superconducting $YBa_2Cu_3O_7$, the Cu(1) site's geometry is square planar forming chains along the b-axis, whereas in non-superconducting $YBa_2Cu_3O_6$ the coordination is linear. The oxygen doping x is continuos through the series $YBa_2Cu_3O_{6+x}$. At $x = 0.4$, a tetragonal to orthorhombic transition accompanies the formation of square planar complexes through the addition of oxygen at the O(1) site in the chains. For intermediate doping levels, the O(1) vacancies can form superstructures with every second (third) site empty Ortho II (Ortho III) phase.

The IL blocks are formed from CuO_5 pyramids. Throughout the continuous doping range, the Cu(2) site of the superconducting planes remains in this square-pyramidal coordination. The apical oxygen bond length is distorted by the removal of orbital degeneracy, as described previously. This leads to a quasi-2D planar structure, the CuO_2 planes. YBCO is a bilayer material with two planes per unit cell separated only by a Y cation layer. It is worth noting that within a family the number of CuO_2 planes per unit cell directly correlates with T_C [41, 42]. Upon doping, the orthorhombic

transition deforms the square symmetry of the CuO_2 planes, whereby the planar oxygen network buckles, shifting the oxygen ions towards the center of the bilayer. The apical oxygen distance has been found to be a function of doping as well, decreasing at higher oxygen concentrations.
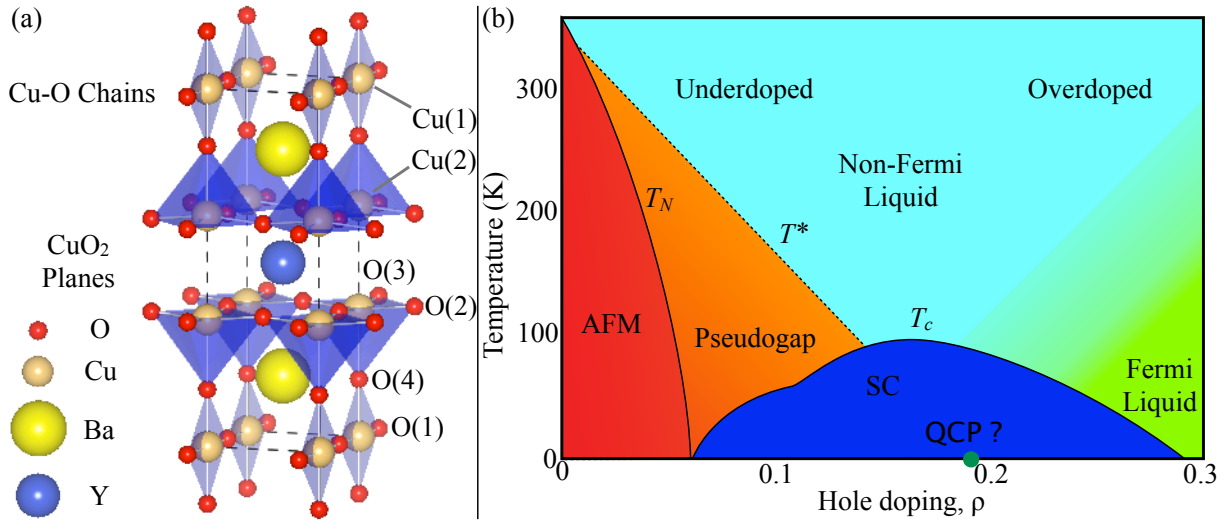
Figure 1.10: **$YBa_2Cu_3O_7$ crystal structure and cuprate phase diagram.** (a) Conventional $YBa_2Cu_3O_7$ unit cell. **(b)** The parent compounds of the High-T_c cuprates are Mott insulators, which display antiferromagnetic correlations above the T_N and an antiferromagnetic ground state below. Upon hole doping the antiferromagnetic order is weakened, and subsequently replaced by superconductivity. The superconducting dome extends over the approximate range $0.05 \le \rho \le 0.3$. On the overdoped side, the system is metallic and can be described by Fermi-liquid theory. The normal state remains enigmatic: characterized by a large region of non-Fermi-liquid behavior with anomalous transport properties and a pseudogap phase at low doping with signs of suppressed charge and spin excitations. The similarities between the cuprate normal state and heavy-fermion metals has evoked the idea of a hidden quantum critical point (QCP) beneath the superconducting dome. Adapted from reference [69].

1.4.2   Carrier Doping in $YBa_2Cu_3O_{7-\delta}$ and the Generic Cuprate Phase Diagram

The formal oxidation states, disregarding covalency, in the insulating parent compound $YBa_2Cu_3O_6$ are Y^{3+}, Ba^{2+} O^{2-}, Cu^{2+} for the square planar Cu(2) site, and Cu^{1+} for the linearly coordinated Cu(1) site. Upon the introduction of holes into the system, a superconducting ground sate can be obtained. This can be accomplished through doping the A-site with divalent Ca, which is analogous to the common practice of cation doping in other cuprate compounds, e.g., Sr^{2+} in La_2CuO_4.

However, for the case of YBCO varying the oxygen concentration in the CR blocks, as described above, has proven to be the most attractive method. At low dopant concentrations, the excess holes mainly form on the Cu(1) site transforming Cu^{1+} into Cu^{2+}. At higher levels, the oxidation states of both Cu sites remains divalent, as the formation of Cu^{3+} requires a ~ 10 eV Coulomb penalty. Instead, the remaining holes are associated with the oxygen sites (i.e., a charge transfer scenario) in the CR and IL blocks with 0.6 holes per chain unit and 0.2 holes per CuO_2 plane in the $YBa_2Cu_3O_7$ conventional unit cell [43, 44, 45, 46]. At full oxygenation, YBCO is only slightly overdoped with a transition temperature of 89 K versus 93 K for optimal doping. To advance further into the overdoped region, simultaneous Ca and O doping must be used [47].

All cuprates share a universal phase diagram as a function of hole doping within the superconducting planes (see Figure 1.9(b)). Here, the hole doping ρ is given in terms of the number of holes near a neighboring Cu site in the CuO_2 plane. Despite the odd number of electrons per unit cell, the parent compounds (e.g., $YBa_2Cu_3O_6$) are insulators. The deviation from conventional band theory is due to the strong electron correlations that drive this class of materials into the Mott insulator phase with long-range antiferromagnetic ordering. The Nèel temperature $T_N \simeq 300 - 500$ K is governed by weak interlayer coupling between planes, while the in-plane superexchange $J \simeq 1500$ K is incredibly strong.

In $YBa_2Cu_3O_6$, the situation is further complicated by the multiples planes and Cu sites per unit cell. This requires the introduction of two extra exchange parameters: intrabilayer coupling $J_\perp$ between Cu(2) ions in adjacent planes and a much weaker coupling $J_{\perp 1}$ between bilayers through a O-Cu(1)-O bridge. Neutron scattering experiments have obtained the following values: $J \simeq 150$ meV, $J_\perp \simeq 10$ meV, and $J_{\perp 1} \simeq 0.04$ meV [49, 50]. Together the exchange parameters define the 2D spin 1/2 square lattice Heisenberg Hamiltonian that models the spin excitation spectrum in YBCO [48]. There is small amount of anisotropic exchange, as well, which must be included to

full understand experimental results [51, 50]. Below T_N, the moments arrange themselves in anti-ferromagnetic order both in-plane and between the Cu-Y-Cu bilayer. Due to anisotropic exchange the moments are not fixed within the plane. There are no moments on the Cu(1) sites in the chains. At 15 K, a second transition takes place. A magnetic moment develops on the Cu(1) site that mediates ferromagnetic coupling between adjacent bilayers, while antiferromagnetic coupling remains within the plane and in individual bilayers [50].

Upon hole doping long-range antiferromagnetic order is lost, though short-range antiferromagnetic fluctuations remain. Just beyond the antiferromagnetic region, the superconducting dome begins. The dome-shape (i.e., transition temperatures initially increase with doping inside the underdoped region, reaching a material specific maximum value at optimal doping, and then decrease to zero upon overdoping) is generic to all cuprates. For YBCO, two superconducting plateaus at 60 and 90 K are often observed. The first plateau, at 60 K, is associated with the formation of chain superstructures and local oxygen vacancies, while the latter plateau reflects the limited doping ability of oxygen incorporation within the chains. A maximum does occur near the $x = 0.93$, after which T_c begins decreasing within the limited overdoped region. As mentioned earlier, with Ca doping the overdoped region can be accessed fully.

Above the underdoped side of the dome sits the enigmatic pseudogap phase. Unlike conventional superconductors, in which the energy gap in the density of states at the Fermi level vanishes near T_c, for cuprates the pseudogap persists until the temperature T^* [52, 53]. Both T^* and the pseudogap increase with underdoping. The origin of the pseudogap remains unresolved [54]. One view suggests that the energy gap above T_c stems from preformed Cooper pairs which lack the phase coherence to form a macroscopic quantum state [55, 56]. For this case, the pseudo gap is merely the remnant of the superconducting gap. Alternatively, in the competition scenario the pseudogap is unrelated to superconductivity, instead a competing order or fluctuation, the details

of which vary with the specific model (e.g., spin density waves or antiferromagnetic correlation), is introduced [57, 58, 59, 60, 61]. Direct evidence for two unique energy gaps has come from angle-resolved photoemission spectroscopy (ARPES) that has found disparate behavior in the nodal and anti-nodal gaps along Fermi arcs in momentum space [62, 63, 64, 65].

The normal state above optimal T_c is known as the "strange-metal" or non-Fermi-liquid region. The transport properties display anomalous behavior: a linear T-dependence of the in-plane resistivity and a quadratic dependence of the Hall angle [66]. This V-shaped region is bound on the underdoped side by the pseudogap phase and on the overdoped side by a metallic phase which displays increasingly Fermi-Liquid behavior (e.g., $\rho \sim T^2$) with continual advancement in doping [67, 68]. The distinction between these three regions is somewhat loose, instead the boundaries are defined by crossover temperatures such as T^*, as a clear phase transition remains to be identified. In addition, the non-Fermi-liquid behavior near optimal doping in the cuprate phase diagram has led to the popular notion of a quantum critical point corresponding to a zero-temperature quantum phase transition, which is masked by the superconducting dome [69].

1.4.3   Electronic Structure

Central to the discussion of the cuprates is the electronic structure of the ubiquitous CuO_2 planes from which the physics of high-T_c superconductivity is widely accepted to originate. Reflecting the mixture of localized and itinerant behavior in the cuprates, it is simplest to start with the local picture of the copper $3d$ and oxygen $2p$ levels and their hybridization in the superconducting planes and then build towards a band model. In the parent compounds, Cu is divalent with a $3d^9$ electron configuration, and subsequently presents with strong Jahn-Teller activity in response to a degenerate crystal field splitting. The distortion from an ideal octahedral environment lifts this degeneracy in the e_g orbitals yielding a single hole in the $d_{x^2-y^2}$ orbital (see Figure 1.10(a)). The
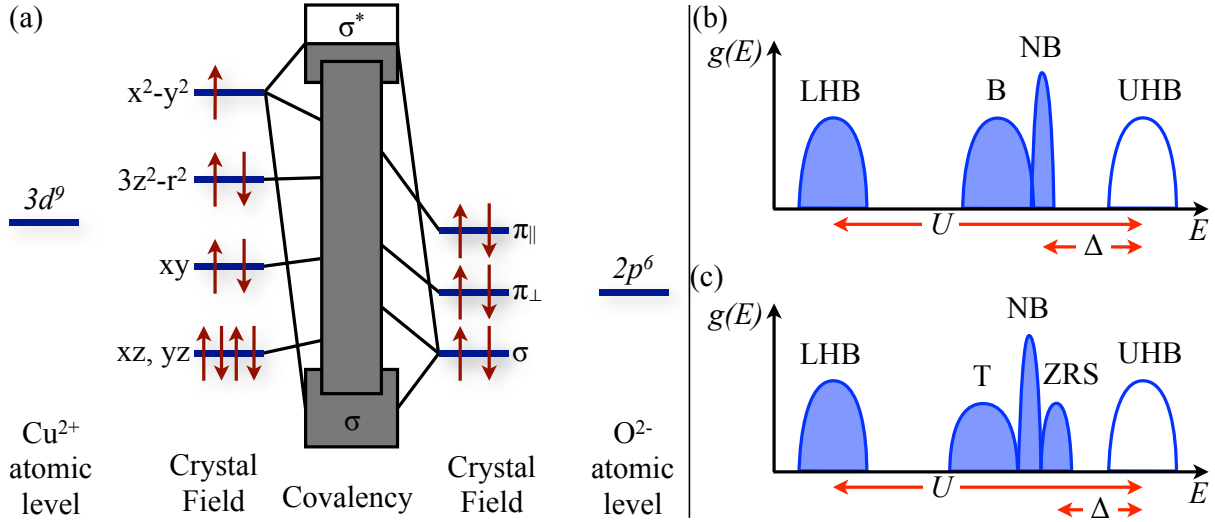
Figure 1.11: **Electronic structure of the CuO$_2$ planes.** (a) Splitting of the Cu $3d$ and O $2p$ levels in a square pyramidal crystal field. Covalent bonding leads to broad σ bonding and anti-bonding bands. Adapted from reference [70]. (b) Three-band p-d model showing the bonding (B), nonbonding (NB), and anti-bonding bands. The anti-bonding band is divided into the lower-Hubbard and upper-Hubbard subbands due to the large onsite repulsion U. The B and NB bands appear in-between the subbands, as $\Delta < U$. (c) The bonding band is exchange split into triplet (T) and singlet (ZRS) states by the interaction of the doped oxygen $2p$ hole and the hole in the Cu $d_{x^2-y^2}$ orbital. Adapted from reference [71].

atomic $2p$ oxygen levels are split by the crystal field, as well, into three levels: $\pi_{||}$, $\pi_\perp$, and σ. The limited orbital overlap with Cu orbitals results in weak hybridization with π-type states and subsequently narrow π-bands. Alternatively, direct hybridization occurs between the oxygen σ states, formed from the p_x and p_y orbitals of the in-plane oxygen network, and the $d_{x^2-y^2}$ copper orbitals. This strong covalent bonding gives rise to broad σ and σ^* bands.

Based on the electronic structure sketched in Figure 1.10(a), the cuprates are expected to be metallic with a half-filled antibonding pdσ band. In agreement, band theory calculations predict a metallic state without magnetic correlations [72]. However, an insulating gap of $\sim$1.5 eV has been observed in optical spectra [73]. Instead, the cuprates fit into the class of Mott insulators with each Cu site hosting a localized hole. Virtual hopping between nearest neighbors leads to a kinetic energy savings and by the rules of superexchange (half-filled to half-filled) an antiferromagnetic

ground state.

The strongly correlated behavior exhibited by the parent compounds naturally led to an early interpretation in terms of the Hubbard model (see equation 1.8), where in the hole notation completely filled shells (e.g., $Cu3d^{10}$ and $O2p^6$) are treated as the vacuum states in Hilbert space [74]. In the strong coupling limit $U \gg t$, the lower subband can be accounted for by perturbation theory allowing for a reduction of the two-subband model to the one-subband t-J Hamiltonian

$$H = -t \sum_{\langle ij \rangle} c_{i\sigma}^{\dagger} c_{j\sigma} + J \sum_{\langle ij \rangle} \left(\mathbf{S}_i \mathbf{S}_j - \frac{1}{4} n_i n_j \right), \tag{1.9}$$

where $\mathbf{S}_i = c_{i\alpha}^{\dagger} \sigma_{\alpha\beta} c_{i\beta}$ are the spin operators at site i for $S = 1/2$, and $\sigma_{\alpha\beta}$ are the Pauli spin matrices. The exchange constant is given by the usual form $J \sim t^2/U$. As will be shown, the one-band $t - J$ model is an accurate description of the low energy physics of the cuprates.

To incorporate hybridization with the planar oxygen network, the more complicated three-band p-d Hamiltonian is frequently used [75], however this model can be simplified to yield an effective one-band model. The oxygen bonding and non-bonding bands appear between the split Hubbard subbands (see Figure 1.10(b)), as the charge transfer energy Δ is smaller than the onsite repulsion U, and the cuprates are in fact charge-transfer insulators after the Zaanen-Sawatzky-Allen scheme [6]. In this case, doped holes will reside on the oxygen $2p$ orbitals. There is a strong exchange interaction between the spin of this doped hole on oxygen and the spin of the hole on Cu,

$$J_{Cu-O} = t_{pd}^2 \left(\frac{1}{\Delta} + \frac{1}{U - \Delta} \right). \tag{1.10}$$

The strength of this interaction is due to the large degree of hybridization which is maximized when the hole sits in a state made up of a symmetry adopted linear combination of the four O $p\sigma_{x,y}$

orbitals. The oxygen bonding band splits due to the large exchange J_{Cu-O} into triplet and singlet bands separated by 3.5 eV (see Figure 1.10(c)) [76, 77]. The singlet formed by the two hole state on Cu and O is popularly known as the Zhang-Rice singlet after its discoverers. It should be noted that the hopping of a singlet hole on oxygen from site j to i necessarily implies the hopping of a Cu hole from site i to j. In light of this, the problem can be reduced to the single-band $t - J$ model with Δ playing the role of U and a hopping integral $t = t_{pd}^2/\Delta$.

1.5 Correlated Interfaces

1.5.1 Interfacial Engineering

As detailed in this chapter, transition metal oxides exhibit a broad spectrum of practical phenomena such as ferroelectricity, colossal magnetoresistance, high temperature superconductivity, and metal to insulator transitions, whose functionalization continues to experience a concerted effort across the broad scientific community. In the bulk, strongly competing orders leave their grounds states susceptible to the influences of lattice distortions and variations in stoichiometry making them excellent candidates for breakthroughs from the field of heterostructure engineering. When matching two oxides at the interface, disparate character in the physical, chemical, electronic, or magnetic structure between them offers another route to exploit susceptibilities and tune the strongly coupled charge, spin, orbital, and lattice degrees of freedom. That is correlated interfaces can naturally leverage underlying instabilities to the ends of manipulating existing electronic phases and searching for emergent ones.

Roughly the interfacial toolbox can be divided into five classifications [78]. (1) The simplest and most commonly used tool is epitaxial *strain*. Strain results from a mismatch between the

atomic arrangement at the two meeting faces of oxide heterostructures and is given by

$$\varepsilon = \frac{a_{substrate} - a_{film}}{a_{film}},$$ (1.11)

where a_{film} is the undistorted length of the bulk material. Here, it is assumed that the film distorts to match the lattice constant $a_{substrate}$ of the much larger (in the direction perpendicular to the plane) and stable substrate. The distortions introduced into the lattice have a direct effect on the electronic structure by modulating the hybridization between atomic orbitals. (2) *Charge transfer* has become a preferred route to unconventional doping at oxide interfaces. A prime examples is a prominent superlattice composed of a Mott and band insulator $LaTiO_3$ and $SrTiO_3$, respectively [79]. In the bulk, the two materials exhibit distinct Ti valencies, however in the superlattice charges redistribute across the layers inducing a metallic state. (3) *Symmetry breaking* is an obvious effect of the abrupt interruption of periodicity at the interface and comes in many flavors from translation symmetry invalidating Bloch's theorem to inversion symmetry to time reversal symmetry. The simultaneous breaking of inversion and time reversal symmetry has recently fueled theoretical investigation into magnetoelectric coupling in oxide heterostructures [80]. (4) If polar materials are included in the heterostructure, conflicting boundary conditions at the interface often leads to *electrostatic coupling* between the constituent layers. (5) *Frustration* between competing interactions are routinely found in magnetic interfaces, where the spin degrees of freedom are mismatched across the interface. These situations are often engineered to produce large exchange biases between ferromagnets and antiferromagnets.

1.5.2 The Ultrathin Limit

While in typical heterostructures individual layers retain their bulk-like properties away from the interface, the constituent layers of an ultrathin superlattice extend up to only a few unit cells. In this case, the lines are blurred between distinct materials coupled at the interface and a new artificial phase of matter. For instance, stacking single unit cells of alternating perovskites along the crystallographic [111] direction yields the equivalent of a single-phase double perovskite $A_2BB'O_6$ with rock salt ordering of the B-site. In this context, artificial layered materials should be viewed as new compounds with their own set of properties bearing a strong resemblance to naturally occurring layered oxides. A key difference remains though. Artificial structures allow access to a region of compounds which are thermodynamically unstable in the bulk. While their growth remains a challenge at the forefront of materials research, the prospects of realizing new functionalities will continue to push the science of material synthesis forward.

Chapter 2

Experimental Techniques

This chapter introduces the experimental techniques used throughout the dissertation to study correlated interfaces in oxide heterostructures. The characterization of buried multilayer interfaces represent a demanding task requiring advanced techniques to uncover the physical mechanisms at work. To overcome this obstacle, x-ray absorption spectroscopy is utilized to probe the electronic structure of oxide multilayers. The chapter starts with a review of theory behind and implementation of x-ray absorption spectroscopy. In the last half of the chapter the ultrathin film deposition technique, laser molecular beam epitaxy (MBE), is discussed. Laser MBE is a leading method in the production of atomically sharp oxide interfaces, and a description of the process and underlying mechanisms involved is included.

2.1 X-ray Absorption Spectroscopy

X-ray absorption spectroscopy (XAS) involves excitations from the inner atomic electron states unassociated with chemical bonding to a valence or continuum states and is therefore a core level spectroscopy. These transitions are allowed under the electric dipole interaction and have strong absorption cross sections. Several excitations are possible (e.g., $s \rightarrow p$, $p \rightarrow d$, and $d \rightarrow f$). In this dissertation, our focus will be on $2p \rightarrow 3d$ transitions, as the materials under investigation contain partially filled $3d$ levels. This is historically referred to as the L absorption edge (see Figure 2.1), and depending on the specific element involved transitions fall into an energy range from 350 eV to 950 eV. Element specificity is an innate feature of XAS and in general all core-level spectroscopies.
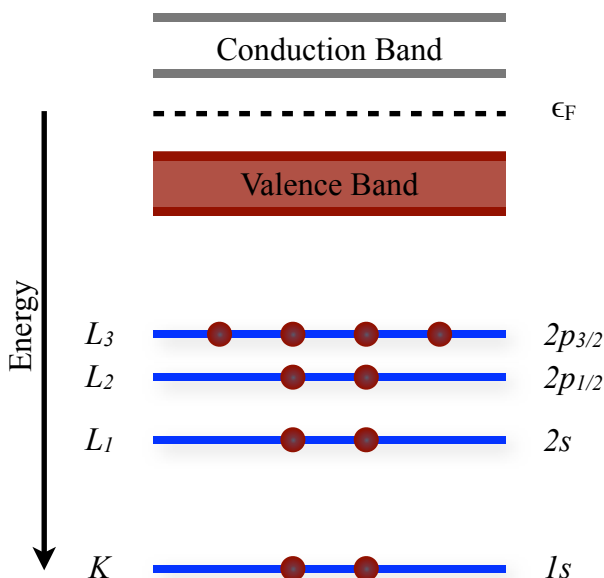
Figure 2.1: **Core states and corresponding edge names.** Historical edge names (right) for various core level excitations (left). The K edge for $3d$ transition metals occurs between $5-11$ KeV. The L edge is split into three different transitions. The L_3 and L_2 edges occur between $400-1000$ eV with only a few eV between them.

For instance, each $3d$ transition metal's L absorption edge will occur at a unique binding energy E_0, which increases moving across the series. This can be understood in terms of the increasing electrostatic potential, generated by the positively charge atomic nucleus, that scales directly with the atomic number Z.

X-ray absorption spectra can be roughly divided into three regions based on the relative energies of the incident photon E and the binding energy of the core electron excited. (1) The pre-edge ($E < E_0$) is typically flat and therefore useful to correct backgrounds. For $1s$ XAS, the pre-edge may contain relatively weak peaks corresponding to quadruple-allowed ($\Delta = \pm 2$) dipole forbidden transitions, e.g., $1s \rightarrow 3d$. (2) The x-ray absorption near-edge structure (XANES) extends typically up to 50 eV above the absorption edge. In the XANES region, the photoelectrons have only a small amount of kinetic energy ($E - E_0$) and experience strong multiple scattering from inner and outer coordination shells. The XANES spectra is sensitive to the coordination number and oxidation state of the absorbing atom and is useful in "finger printing" analysis of materials.

(3) The extended x-ray absorption fine structure begins at approximately 50 eV and finishes up to 1000 eV above the edge. These photoelectrons possess a high-level of kinetic energy, and only single scattering events by nearest neighbors need to be accounted for. EXAFS is a powerful technique for resolving quantitative aspects of the nearest neighbor structure. For soft x-ray absorption spectroscopy ($E < 1000$ eV), which is the focus of this dissertation, the EXAFS regions are either inaccessible or interrupted by other closely spaced edges found within this narrow energy window.

2.1.1 One-Electron Picture

Neglecting electron-electron correlations, XAS spectra can be simply explained in terms of the materials band structure. Consider the density of states (DOS) for an insulating material with a valence shell consisting of $3d$ electron states (see Figure 2.2(a)). The Fermi-level demarcates the unoccupied and occupied DOS separated by a band gap, while the tightly bound $2p$-core level is buried deep below the Fermi-level. The core levels do not participate in bonding, and their contributions to the DOS are represented by delta functions. The spin orbit interaction splits the $2p$ level into a multiplet of $(2s+1)(2l+1) = (2(1/2)+1)(2(1)+1) = 6$ states with a level degeneracy of $(2j+1)$. This gives two fine structure levels labeled by the total angular momentum $j = 3/2, 1/2$. The $2p_{3/2}$ level has twice as many states, and the delta function is twice as high in response. The separation between adjacent levels in a multiplet is given by $E(j) - E(j-1) = j\zeta$, where ζ is the spin orbit coupling constant. The spin-orbit splitting is proportional to Z^4 and can be rather large for the 2p level in the $3d$ transition metal series.

In XAS, excitations from the occupied core DOS into the unoccupied DOS are made. The spectrum obtained from this process will be a convolution of the core DOS and the unoccupied valence DOS. Since the core DOS consists of two delta functions, 2p XAS essentially maps the unoccupied DOS twice across the L edge, which splits into two separate regions knowns as the L_3
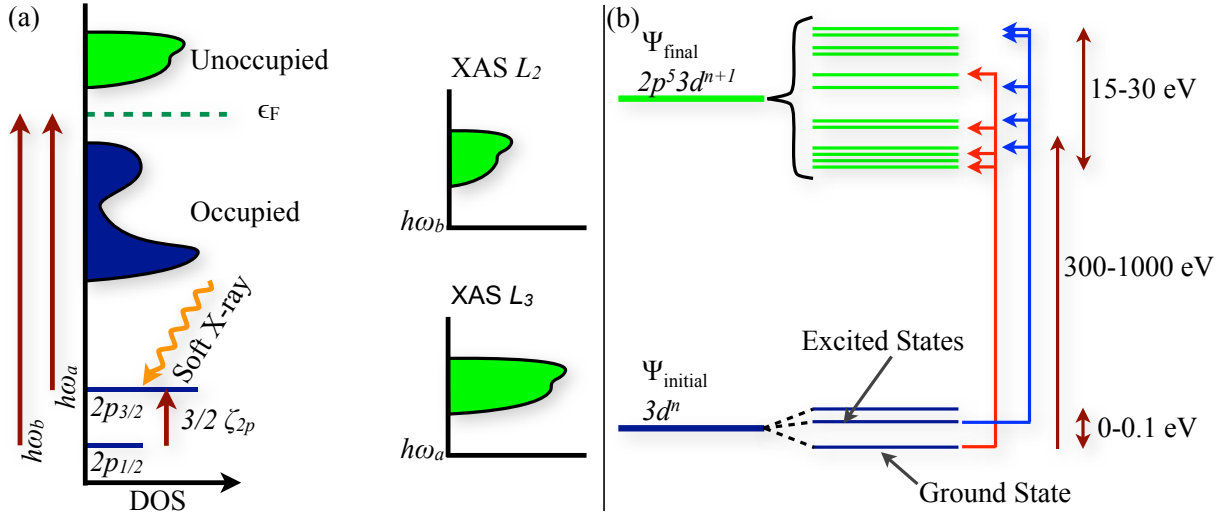
Figure 2.2: **One-electron and configuration pictures of x-ray absorption spectroscopy. (a)** In the one-electron picture, core level excitations map out the unoccupied DOS, as the core levels are represented by delta functions separated by a multiple of the spin orbit coupling constant. **(b)** Configuration Picture. The ground state belongs to the $3d^n$ configuration. There are several states belonging to the final $2p^5 3d^{n+1}$ configuration. The selection rules only allow for transitions to a minority of possible final states. A small number of excited states lie close to the ground state but each transition to their own unique spectrum of final states. In this way, XAS becomes a sensitive probe of the initial state of the system. Adapted from reference [81].

and L_2 edges. The L_3 edge will have twice the intensity, and a shift of $3/2$ times the spin orbit coupling constant is introduced.

2.1.2 Configuration Picture

Unfortunately, the simplistic picture of one-electron theory fails to reproduce XAS spectra, as there is strong overlap between the core hole and valence electron wavefunctions. The most prominent features in XAS spectra originate from the formation of excitons, a bound state between the $2p$ core hole and the extra electron excited into the valence level. That is, the exciton represents the end result of the XAS process. In this point of view, the absorption of light transforms the many-electron ground state of the system into a final state configuration representing the exciton, e.g., $(\Psi_i = 3d^n \rightarrow \Psi_f = 2p^5 3d^{n+1})$

For a given electron configuration, the number of corresponding possible final states can become quite large. In $2p$ XAS, the final electron configuration will be $2p^5 3d^{n+1}$. For $n = 9$, the number of final states remains small coming from only the $2p$ core hole multiplet: 2 levels with a total degeneracy of 6 states. In general, the total degeneracy is given by $6 \times \frac{10!}{(10-n+1)!(n+1)!}$. The $2p$-core hole contributes a factor of 6, and the multiplets of the $3d^{n+1}$ configuration are accounted for by the combination $\binom{10}{n+1}$. Similar to before, a level of a multiplet can be labelled by the total angular momentum J. Electron-electron interactions introduce another complication, as well. The degree of electron repulsion varies with the exact combination of occupied orbitals, which further spreads these final states out across the energy range. For a thorough review of multiplet theory as it relates to XAS, see reference [82]. Given a complex multiplet structure extended over an absorption edge, the prominent and well-defined peaks, often found in XAS spectra, appear to be at odds with expectations. This is resolved through the incorporation of dipole selection rules.

Using symmetry arguments, a set of selection rules can be derived that constrain the transitions between initial and final states. In time-dependent perturbation theory, the transition probability W from the initial state Ψ_i to the final state Ψ_f is given by Fermi's golden rule

$$W_{i \to f} = \frac{2\pi}{\hbar} |\langle \Psi_f | T | \Psi_i \rangle|^2 \delta(E_f - E_i - \hbar\omega), \qquad (2.1)$$

where the delta function ensures energy conservation. A transition occurs, only if the final state energy E_f equals the sum of the initial state and x-ray energies E_i and $\hbar\omega$, respectively. The transition operator T represents a one-photon transition. Taking only the dipole term from the Taylor expansion, the transition operator reduces to $T = \hat{e}_q \cdot \vec{r}$, where $\hat{e}_q$ is the unit vector of the photon electric field, and $\vec{r}$ is the position vector. The dipole operator is odd under parity. This constrains transitions to be between states of different parity, otherwise the integral $\langle \Psi_f | T | \Psi_i \rangle$

will be odd and therefore vanishing. From this simple argument, the following selection rules can be found:

$$\Delta l = \pm 1 \tag{2.2}$$

$$\Delta m_l = 0, \pm 1$$

$$\Delta j = 0, \pm 1$$

$$\Delta m_s = 0$$

$$\Delta L = 0, \pm 1$$

$$\Delta S = 0$$

$$\Delta J = 0, \pm 1$$

It should be noted that the dipole operator does not work on the spin component of the wavefunction. While there are many final state belonging to the $2p^5 3d^{n+1}$ configuration, the selection rules limit and define the ones which are accessible based on the initial state (see Figure 2.2(b)). In this way, XAS becomes a sensitive probe of the system's electronic ground state.

2.1.3 Polarization Dependence

In polarization dependent XAS, the orientation of the electric field vector can be used to tailor restrictions on the allowed final states. Consider, the simple case of an excitation from a s to a p orbital in the one-electron picture. The p level is split into three different orbitals: p_x, p_y, and p_z. From symmetry arguments, z-polarized light can only excite an electron from a s to a p_z orbital. The same is true for x- and y-polarized light. Now, imagine that the p_z orbital is preferentially unoccupied in the ground state. In the one-electron picture, XAS probes the unoccupied DOS in

accordance with the exclusion principle, and the intensity of absorption will become dependent on the orientation of the electric field vector, i.e., a dichroism will be present. In general, the use of linearly polarized light to probe the orbital occupation of the initial state is called x-ray linear dichroism (XLD). For $2p$ XAS, the situation becomes slightly more complicated, as the symmetries of the five d orbitals do not lend themselves to a simple interpretation in terms of cartesian coordinates. However, the guiding principle is the same. The choice of electric field vectors restricts the final states available, and a difference in intensity between polarizations reflects imbalance in orbital occupation for the ground state.

Often anisotropy exists in the spin component of the ground state, as well. At first, it may not seem obvious how XAS detects imbalances in spin-up and spin-down electrons, since the dipole transition operator does not act on spin space. The answer is spin-orbit coupling which provides the link between spin moments and the dipole matrix elements. This can be understood within the "two step model" of Stör and Wu [83]. In the first step, consider only the excitation probability of the initial state. In the basis of the total angular momentum operator, each spin becomes affiliated with particular orbital states, which will then be acted upon by the dipole operator. The excitation probabilities for orbital states vary strongly with photon polarization and can be determined through the electric dipole matrix elements. This leads to an imbalance in the number of spin-up and spin-down electrons excited for a specified photon polarization. For instance, if right-circularly polarized light is used to transition electrons from the $p_{3/2}$ level, statistically more spin-up electrons will be excited than spin-down. The effect is exactly opposite for left-circularly polarized light. For the $p_{1/2}$ level, the orbital and spin affiliations will not be the same as in the $p_{3/2}$ case, and the imbalance in spin-up and spin-down electrons flips for the right- and left-circularly polarized light with different weightings as well. In the second step, the preferred spin orientation of the excited electrons becomes a probe of spin imbalance in the final states. By the exclusion

principle, an imbalance in spin within the unoccupied DOS will lead to a difference in absorption intensity between right- and left-circularly polarized light. This is referred to x-ray magnetic circular dichroism (XMCD).

2.1.4 Experimental Setup

XLD and XMCD measurements, described in the following chapters, were performed at the 4-ID-C beam line of the Advanced Photon Source, Argonne National Laboratory. The x-ray source is a unique fully electromagnetic undulator capable of delivering vertical, horizontal, and right- and left-circular polarizations of light from $500 - 2800$ eV. The availability of multiple polarizations allows the sample surface to be kept at a fixed incidence with respect to the x-ray beam path avoiding geometrical artifacts in dichroism experiments. The monochromator is a spherical grating which offers a resolution of ~ 0.1 eV at a photon energy of 1000 eV. In the soft x-ray regime, the shallow penetration depth makes the transmission method of obtaining spectra inapplicable for most samples. Instead, the spectra were measured in fluorescence (TFY) and electron (TEY) yield modes. The photons emitted in florescence have a mean free path similar to the incident photons and are considered to be bulk-sensitive. While the ejected electrons in electron yield interact strongly with the sample before reaching the surface and have a shallow probing depth which is exponentially cut off from the surface. The combination of the two methods has been used for depth profiling and to access the electronic structure of buried multi-layer interfaces. Energy alignments were carried out by measuring a standard simultaneously in the diagnostic section of the beamline. Each spectrum was normalized to the beam intensity monitored by a gold mesh set in front of the samples. The endstation consists of a liquid He flow cryostat capable of reaching temperatures down to 10 K and a 7 Tesla superconducting magnet. In order to avoid spurious signals, XMCD spectra were recorded in both positive and negative magnetic fields. Additional

details on the 4-ID-C can be found in reference [84]

2.2   Laser Molecular Beam Epitaxy

Laser MBE refers to a thin film and multilayer synthesis combination technique involving a physical vapor deposition process, known as pulsed laser deposition (PLD), and *in situ* surface monitoring via high-pressure reflection high-energy electron diffraction (HP RHEED). Laser MBE can be a misnomer, as the plasma plume may contain a variety of species including ions, electrons, neutral atoms, and in the case of strong interaction with ambient oxygen molecular binary oxides. In the first subsection, the focus will be the deposition process, followed by a subsection on RHEED. At the end, a brief review of the deposition conditions for $YBa_2Cu_3O_7$, $La_{2/3}Ca_{1/3}MnO_3$, and $SrTiO_3$ will be given.

2.2.1   Pulsed Laser Deposition

Laser-assisted film growth began in 1965 shortly after the development of the laser. The first films were semiconductors and dielectrics with ablation carried out by a ruby laser, however the technique yielded films inferior in quality to those produced by competing methods. This changed in 1987, when Dijkkamp and Venkatesan demonstrated superior growth of a high temperate superconductor $YBa_2Cu_3O_7$ compared to other thin film processing methods at the time. Afterwards PLD became one of the dominant techniques in the deposition of thin films and multilayers of complex oxides ceramics. In the early nineties, PLD benefitted from achievements in pulsed lasers with higher repetition rates and shorter pulse intervals. The most recent advancement, *in situ* surface monitoring with HP RHEED, has engendered PLD with unit cell precision bringing it to the forefront of modern materials research. For a thorough review on the development and theory of PLD, see reference [85].

Ablation and Plume Propagation

The PLD process begins with the ablation of target material by a high-fluence laser beam in the range of $1-4$ J/cm^2. The target typically consists of a stoichiometric form of the material intended to be synthesized. At the earliest stage of laser-solid interaction, faster electronic excitations (~ 10 fs) absorb the incoming photon stream. Within ~ 100 ps, this energy is converted to thermal and chemical energy resulting in practically instantaneous removal of target material from the surface [86]. Rapid heating rates (10^{11} K/s) and increasing gas pressures of 10-500 atm are observed at the target surface [85]. The evaporated particles quickly equilibrate within a few collisions and ionize forming a dense plasma plume above the target surface. For long pulse durations ~ 10 ns, found in the KrF (248 nm) excimer laser of this dissertation, the remainder of the laser pulse is absorbed
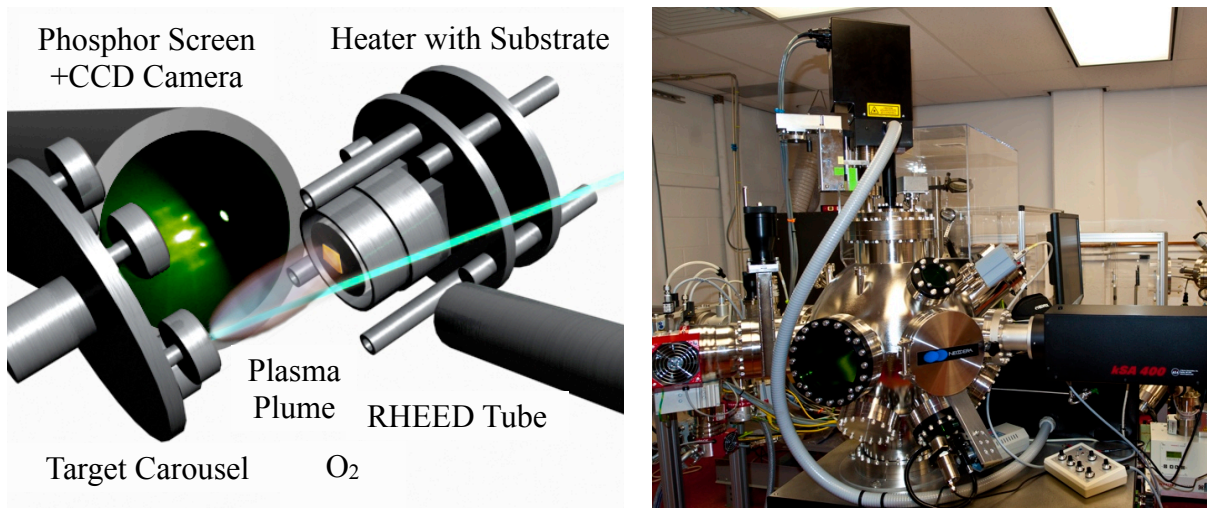
Figure 2.3: **Laser MBE experimental setup. (Left)** Schematic of PLD system [87]. Laser light enters the chamber and strikes the queued target in the carousal. PLD systems are typically capable of holding multiple targets in a computer controlled carousal facilitating the synthesis of complex multilayers. The plasma plume is ejected from the surface of the target and interacts with the ambient gas, before being deposited on the substrate. The substate temperature is continuously controlled and monitored. Also a HP-RHEED system is illustrated, where electrons exit a small orifice into the chamber and scatter off of the growing multilayer. The scattered electrons collect on a phosphorous screen, which allows for analysis of the electron diffraction pattern. **(Right)** Photograph of the Neocera Laser MBE system used for sample fabrication in this dissertation [88].

by the plasma shielding the target and increasing the temperature and pressure within the plume. The resulting high pressure ejects the plasma from the target surface.

The plume propagates from target to substrate within 10-100 μs depending on the target to substrate distance and pressure within the chamber. In this time span, the plasma interacts strongly with the background gas (mainly oxygen). It is understood that a certain degree of thermalization of the species in the plume is required to obtain films of desired stoichiometry and morphology. Reducing the kinetic energy of ablated particles is necessary to avoid sputtering of the growing film and defect creation. Often this goal is achieved by simply varying the background gas pressure. However, O_2 pressure is an important thermodynamic variable that must be adjusted to maintain the stability of the chemical phase of the growing film, as well. In this case, sometimes the optimal solution is to adjust the target substrate distance or the fluence of the incident laser beam. However, there is a material dependent minimal threshold, below which ablation cannot occur [85].

Atomistic Processes

At this stage, species within the plume begin absorbing onto random sites at the substrate surface, and the growing film evolves. Thin film growth is a complex subject involving multiple competing mechanisms that are material and technique dependent. Therefore, the goal will be to give a generalized overview with some PLD specifics. Most notably, PLD naturally imposes a pulsed flux. In the short run during plasma substrate interaction, film formation is driven by a series of kinetic processes and in the long run between the succession of impinging plumes by thermal ones. (Note, only a brief review of film growth will be give here. For a more thorough discussion, see reference [89].)

After absorption, deposited species (adatoms) on the substrate surface are mobile with a diffusivity D determined by the substrate temperature T_s. They remain mobile until finding an ener-

getically favorable site. In the absence of defects, this means diffusing to a site of higher atomic coordination such as incorporation into step edges or island formation, where initially two adatoms met. Of course this is a dynamical process, and there is finite probability that adatoms will escape from a step edge, island, or even the surface of the film (desorption). As the new layer forms, the probability of nucleation on top of an existing island increases as a function of the layer's expanding coverage. These adatoms will also diffuse to higher coordination sites which requires transferring down to the lower level by a mechanism referred to as interlayer mass transport [90]. Transfer over the step edge is regulated by the Ehrlich-Schwoebel (ES) barrier [91, 92]. For large ES values, voids within the growing layer will remained unfilled, and 3D island growth will occur.

PLD differs from other physical vapor deposition processes in two main ways. First, the flux is inherently pulsed, as opposed to a constant flux which allows for a steady state of adatoms to be reached on the substrate surface. Instead, the average flux $F = N_p/\tau$ must be considered, where N_p is the amount of adatoms deposited per pulse and τ is the time between pulses. Second, the energy of the species within the plume can vary broadly and are on the order of a few eV in high vacuum, while other methods typically involve particles with energies in the fractions of eV. In the case of the latter, a similar spread in energy can be obtained in PLD given strong interaction between the plume and the background gas.

Step-Flow and LBL Growth

Vicinal surfaces must incorporate natural terraces from the miscut in the substrate which serve as important nucleation sites in crystal growth. The average spacing between terraces is given by $L \simeq a/\alpha$, where α is the miscut angle and a is the lattice spacing. In the regime of low deposition flux F and high diffusivity, the probability of migrating into terraces overtakes island formation. This results in terraces continually expanding across the surface referred to as step-flow. If the

ES barrier is negligible, then larger terraces will tend to out grow smaller ones resulting in step-bunching. For moderate values of ES step-flow growth stabilizes. When the time between pulses exceeds the lifetime of a diffusing adatom on a terrace, the condition for step-flow growth becomes $F < 2N_p D/L^2$ [93].

While step-flow results in smooth, uniform layers, there are no periodic changes in the the surface that can be tracked *in situ* to determine layer thickness and completeness. Instead, an ideal layer-by-layer (LBL) growth is required. This necessitates island formation to be initially favored over incorporation into the step edge. In this case, the number of islands rises rapidly and falls offs sharply after coverage reaches only a few percent, when adatoms are more likely to find an island than another adatom [94]. As a result, the number of nucleation sites saturates in PLD after the first pulse. The islands are separated by a characteristic spacing λ which is determined by the diffusivity and flux. To avoid step flow, the condition $\lambda < L$ must be satisfied. The additional pulses deposit material that initially leads to island expansion called ripening. Later, nucleation on top of an existing islands becomes unavoidable. The result is a two layer growth front which is unfavorable to LBL growth. Increasing diffusion to promote interlayer mass transfer has the undesirable effect of leading to a step-flow growth.

One possible solution is interval deposition, in which enough material for exactly one layer is deposited as quickly as possible followed by an extended annealing time. The reasoning for this lies in the surface changes that occur between pulses. In the early stage of layer growth, adatoms migrate to islands from the initial surface versus interlayer mass transfer. This will lead to a fractal pattern of islands on the surface [94]. Between pulses, thermal processes will smoothen island contours reducing the step edge density. Reduced step edge density at a fixed coverage clearly hinders interlayer mass transport. To avoid this, the time between pulses should be reduced to interrupt thermal smoothening processes. Also the high supersaturation associated with PLD, will

lead to an increase in nucleation resulting in a large number of smaller islands.

2.2.2   Reflection High-Energy Electron Diffraction

RHEED is an *in situ* electron diffraction technique used to characterized the surface of crystalline materials especially throughout thin film growth. Due to the grazing incidence geometry, only scattering from the surface will contribute to the diffraction pattern, which distinguishes RHEED from bulk-sensitive electron diffraction techniques. Until recently, the ultrahigh vacuum require-ment of the electron guns utilized in RHEED kept them from application in PLD. Development of differential pumping systems have removed this hurdle, and HP RHEED represent a growing trend for *in situ* characterization of oxide thin films and multilayers.

All diffraction techniques begin with a "suitable" beam of radiation, whose characteristic wave-length λ fixes the amount of reciprocal space that can be sampled. This can be expressed mathe-matically as a limit on the scattering vector $Q_{max} = 4\pi/\lambda$. In order to properly resolve distances on the order of neighboring atoms, approximately 1 Å, then the diffraction experiment must be capable of reaching far enough out into reciprocal space. To facilitate this, the incident electrons are accelerated to energies $E \sim 25$ keV, which gives a de Broglie wavelength $\lambda = \frac{h}{\sqrt{2m_0 E}} = .078$ Å, where m_0 is the electron's rest mass [96].

The electron beam in RHEED strikes the sample at grazing incidence, which coupled with the shallow penetration depth of electrons in matter implies that only the surface atoms participate in forward scattering. Considering an ideally flat surface, the diffraction problem reduces to that of a two dimensional (2D) lattice. In this case, reciprocal space will consist of an array of parallel and infinite rods that yields a 2D reciprocal lattice of points retaining the translational and rotational symmetries of the real space lattice, when cut by a plane perpendicular to the rods' axes. The infinite structure in the third dimension results from the Fourier transform relationship between
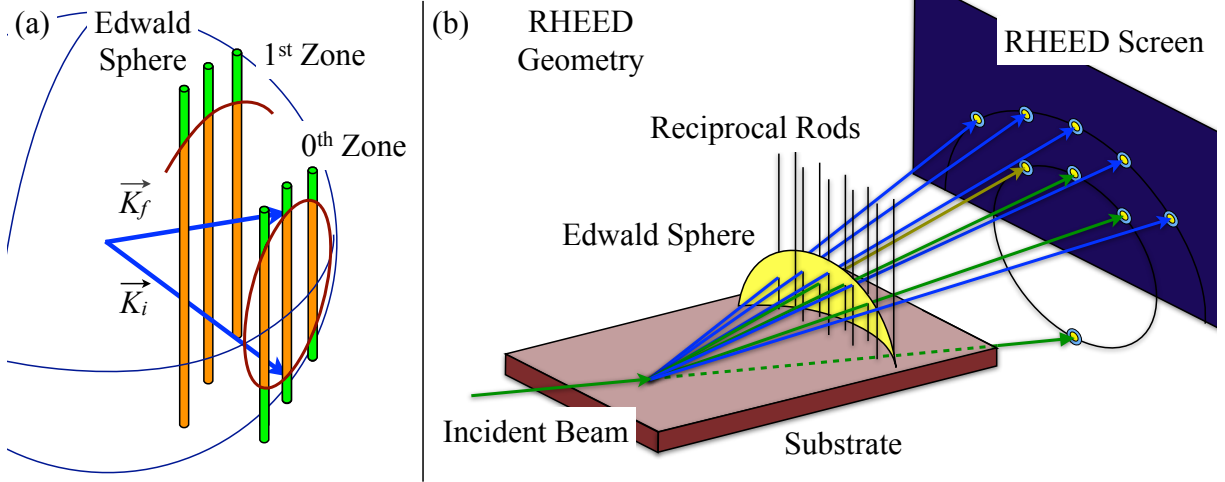
50

Figure 2.4: **Edwald sphere construction and electron scattering geometry in RHEED. (a)**
Schematic of Edwald sphere with a reciprocal lattice of an infinite rods. In elastic scattering, the
condition for diffraction reduces to the intersection of the reciprocal lattice with a sphere of radius
$|\vec{k}_i|$. For a 2D lattice with infinite extension in the third dimension, the diffraction conditions will
be met along a series of circles called Laue Zones. **(b)** Schematic of RHEED geometry. The
forward scattered electron beam off a crystalline substrate will produce a diffraction image on a
distant phosphorous screen, whose form can be determined from the Edwald sphere construction
shown in part (a). Adapted from reference [95].

real and reciprocal space and the loss in translational symmetry in the third dimension of real

space. For a square lattice in real space with lattice constant a, the reciprocal lattice is also a

square lattice with constant $2\pi/a$, where an infinite rod extends normal to the plane from each

reciprocal lattice point.

Ignoring multiple-scattering events the so-called kinematic approximation, the condition for

diffraction can be simply stated in terms of momentum transferred to the scattered electron as

$$\vec{Q} = \vec{k}_i - \vec{k}_s = \vec{G}, \tag{2.3}$$

where $\vec{k}_i$ and $\vec{k}_s$ are the incident and scattered electron wave vectors, and $\vec{G}$ is a reciprocal lattice

vector. Limiting the discussion to elastic scattering (i.e., $|\vec{k}_i| = |\vec{k}_s|$), the locus of all possible

orientations of the incident and scattered wave vectors construct an Edwald sphere in reciprocal

space with a radius of $|\vec{k}_i|$ (see Figure 2.4(a)). When the surface of the Edwald sphere intersects a reciprocal rod, the diffraction condition is met for the corresponding reciprocal lattice vector. The Edwald sphere is centered by convention, such that the specular reflection meets the diffraction condition for the (00) rod. In practice, the incident beam falls along a high-symmetry direction of the lattice. In this case, the plane containing the set of (0n) rods (n is an integer) cuts a circle into the Edwald's sphere, known as the zeroth Laue zone. The (0n) rods, which intersect this circle, fulfill the diffraction condition. In a similar way, higher order Laue zones can be constructed.

The forward scattered beam impinges on a circular 2D phosphorous screen, which typically subtends a large enough solid angle to include multiple Laue zones from the zeroth order up (see Figure 2.4(b)). The total number of Laue zones depends upon the specific limits placed on the scattering geometry by chamber design. The detector is further limited by the lack of energy resolution, subsequently elastic and inelastic scattering contribute to RHEED images. Also, electrons strongly interact with matter leading to strong multiple scattering requiring the use of dynamical scattering theory. Consequently, the RHEED images necessarily includes deviations from the simple kinematic theory outlined such as Kikuchi lines and modulations in reflections' intensities. These added complications require modeling to extract quantitative information.

RHEED is most often applied towards real time monitoring of thin film growth. For instance, increase surface disorder is detectable as streaking of the reflection spots in RHEED images. Here, disorder reduces the crystalline correlation length leading to a finite thickness of the reciprocal space rods. Three dimensional island formation can be detected from transmission patterns appearing in the RHEED image. Both developments are unfavorable to LBL growth and require close monitoring. Also, RHEED can measure the timed dependent intensity of the specular spot. Oscillations in the specular intensity correspond to the completion of new layers on the surface of the substrate. In LBL growth, the forming new layer interferes destructively with the under layer.

At exactly half coverage an oscillation will reach a minimum, and then rise to the original intensity, as the new layer is completed. Often the original intensity is not met with accumulating layers, as surface disorder increases dampening oscillations. Sometimes, this can be corrected with a dwell time between layers, which allows for thermal smoothening processes.

2.2.3 Deposition Conditions: $YBa_2Cu_3O_7$, $La_{2/3}Ca_{1/3}MnO_3$, and $SrTiO_3$

The synthesis of $YBa_2Cu_3O_7$/$La_{2/3}Ca_{1/3}MnO_3$ and $YBa_2Cu_3O_7$/$SrTiO_3$ multilayers was largely dictated by the $P(O_2)$-T phase diagram of $YBa_2Cu_3O_y$ (see Figure 2.5). On the phase diagram narrow regions, which are conductive to epitaxial growth, have been identified for various deposition techniques. Typically high quality film formation takes place near thermodynamic stability lines, and the films as-grown are oxygen deficient ($YBa_2Cu_3O_6$). This requires a post-growth annealing in $300 - 760$ Torr of O_2 to fully oxidize $YBa_2Cu_3O_7$ films.

Multilayers were deposited on $SrTiO_3$ substrates (5 mm x 5 mm x 0.5 mm) by interval PLD in a LBL fashion. Fabrication was carried out in a recently developed PLD system featuring infrared laser substrate heating and *in situ* monitoring via HP RHEED. Stoichiometric targets of the constituent materials were sequentially ablated by a KrF excimer laser. In the case of $YBa_2Cu_3O_7$, the optimal conditions for 2D growth were found to be a low laser frequency of $6 - 8$ Hz with a dwell time between the epitaxial deposition of each individual unit cell, which allowed for thermal smoothening processes. For LCMO, interval deposition with a laser frequency of $15 - 25$ Hz proved to be the most favorable conditions for a LBL growth. Furthermore, interval deposition allowed for a mutually compatible growth regime for YBCO and LCMO to be achieved, which is discussed thoroughly in the adjacent chapter. $SrTiO_3$ deposition required a low frequency growth 3 HZ with a dwell time between consecutive layers. RHEED specular intensity oscillations were observed for all layers, allowing for unit cell control during the construction of these multilay-
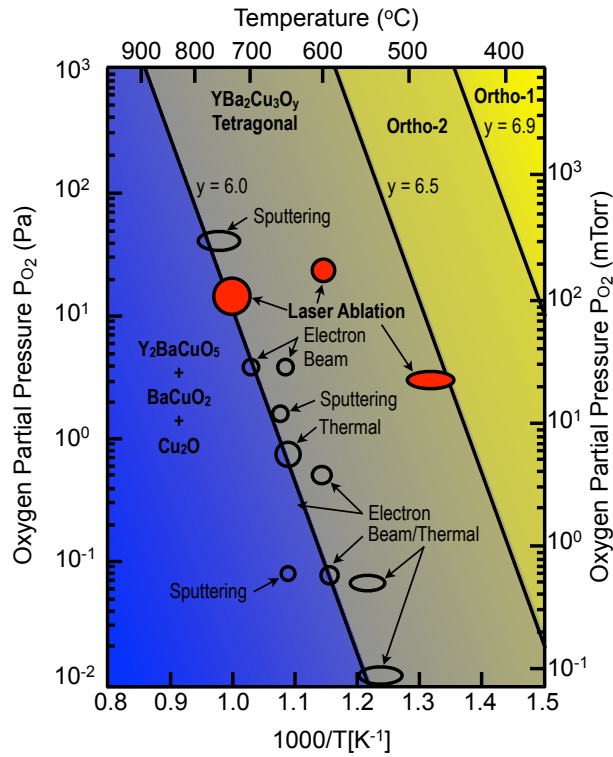
Figure 2.5: **YBa$_2$Cu$_3$O$_7$ $P(O_2)$-T phase diagram.** Regions favorable to high-quality epitaxial growth are marked for various deposition techniques. Adapted from reference [97].

ers. The substrate temperature was continuously monitored and held at 750° C, and an oxygen partial pressure $P(O_2) = 250$ mTorr O$_2$ was maintained inside the chamber throughout the deposition. Immediately after deposition, the samples were annealed at 550° C, and the chamber was back-filled with oxygen to 500 Torr. These annealing conditions were maintained for 1 h. The structurally and electronic qualities of the multilayers, produced under these conditions, are shown in the subsequent chapters through a combination of characterization techniques, e.g., x-ray diffraction, transmission electron microscopy, and transport measurements.

Chapter 3

Enhanced Spin and Electronic Reconstructions at the Cuprate-Manganite Interface

In this chapter, we examine the results from our search for a mutually compatible growth regime in cuprate-manganite heterostructures. Enhancements in the spin and electronic reconstructions at the cuprate-manganite interface are observed. Polarized x-ray spectroscopy measurements taken at the Cu L edge reveal up to a five-fold increase in the magnetic dichroism as compared to past experimental results. The strong dichroic signal allows us to successfully apply the magneto-optical sum rules that reveal an uncompensated Cu moment, $m_{spin} = 0.3079 \, \mu_B/$Cu, induced in the CuO_2 plane. Furthermore an increase in the degree of interlayer charge transfer up to $0.25e$ (where e is charge of an electron) per copper ion is observed leading to a profound reconstruction in the orbital scheme for these interfacial copper ions. It is inferred that these enhancements are related to an increase in T_{MI} observed for manganite layers grown with rapidly modulated flux.

3.1 Introduction

The confluence of multiple competing order parameters stemming from the rich spectrum of ground states accessible in artificial transition metal oxide multilayers facilitates the exploration of unique quantum states and phenomena at the interface. A quintessential example is the junction between the high-T_c cuprate $YBa_2Cu_3O_7$ (YBCO) and the colossal magnetoresistance manganite $La_{2/3}Ca_{1/3}MnO_3$ (LCMO), for which the exact nature of the electronic and magnetic structure at and near the interface remains actively debated. On one hand, proximity effects (PE) are excepted to play a dominate role in determining properties [98], and indeed prior extensive measurements

of YBCO/LCMO heterostructures have revealed suppressions in the critical temperature and free carrier response operating over a length scale far exceeding the anticipated superconductive (SC) condensate penetration depth ξ_F [99, 100]. One possible explanation for the observed long range PE is a triplet pairing component of the SC condensate due to the presence of magnetic inhomogeneity near the interface [101].

Through the combined utilization of polarized neutron reflectivity and X-ray magnetic circular dichroism (XMCD), a definitive picture of the microscopic magnetic profile in YBCO/LCMO multilayers was obtained which coincided with the aforementioned theoretical predictions including an induced net moment in the SC layer at the interface with an antiferromagnetic coupling to the ferromagnetic (FM) layer [102, 103, 104]. However, subsequent X-ray linear dichroism (XLD) measurements established the role of orbital reconstruction in which a strong covalent Cu-O-Mn bond at the interface promotes charge transfer between layers and a rearrangement of the Cu $d_{z^2 - r^2}$ occupation[105]. The sign of the magnetic interaction between Cu and Mn is simply determined by the Goodenough-Kanamori rules, while charge transfer across the interface offers an alternative explanation to the previously seen long range PE [100, 106]. Despite these advancements, recent theoretical and experimental results have reproduced the magnetic dichroic signal on Cu but failed to account for the orbital reconstruction [107, 108]. Furthermore, recently evidence for a triplet SC component in YBCO/LCMO heterostructures has been emerging [109].

In this chapter, we report on a resonant x-ray absorption spectroscopy (XAS) study of the electronic and magnetic profile of the cuprate-manganite interface in a representative [YBCO (9 u.c.)/LCMO (26 u.c.)]×3 superlattice (SL). Circularly polarized X-rays are used to acquire element sensitive information about the magnetic structure of the interface, while linear polarizations probe the electronic structure. Temperature dependent dc transport measurements explore the electronic and magnetic qualities of the films. We conclude that both spin and electronic reconstructions are

present and markedly enhanced. Furthermore, these enhancements are linked to the structural and chemical properties of the manganite-cuprate layers obtained by rapidly modulated flux. Also, the sum rules are applied for the first time (to the best of the author's knowledge) to this interface, and an uncompensated moment which closely matches recent local spin density approximation (LSDA+U) calculations is found [107].

3.2 Results and Discussion

3.2.1 Mutually Compatible Growth Regime

A mutually compatible growth regime (i.e., temperature and pressure) for YBCO and LCMO was achieved through interval deposition, in which material is deposited by high frequency pulses followed by an extended dwell time between the deposition of each unit cell (u.c.) [110]. Undamped RHEED specular intensity oscillations (not shown) were observed for both YBCO and LCMO layers over a large number of cycles allowing for a layer-by-layer growth with u.c. control. Figure 3.1(b) shows the post growth RHEED image for the SL along the (001) direction. The presence of unbroken crystal truncation rods up to the second order combined with well defined specular (00) and off specular Bragg reflections testifies to the quality of the 2-D growth.

To determine the structural properties of the SL, we performed X-ray scattering at beamline 5-BM-D of the Advanced Photon Source (APS) at Argonne National Laboratory. Figure 3.1 shows the specular X-ray diffraction along the (00L) crystal truncation rod as a function of the magnitude of the out-of-plane momentum transfer vector, Q_z. As seen in Figure 3.1(a), the SL shows all expected Bragg reflections for c-axis oriented layers and Kiessig fringes testifying to the quality of the film and sharpness of the interfaces. Based on the position of the YBCO (005) reflection, the average c-axis lattice constant for the YBCO layers in the SL is 11.70 Å, which agrees with
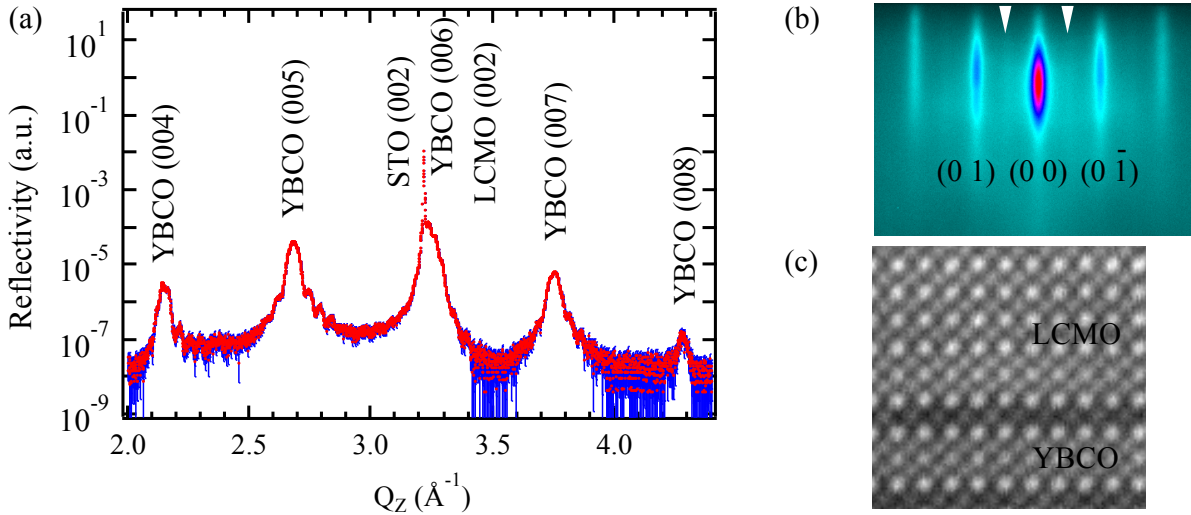
57

Figure 3.1: **Structural Characterization.** **(a)** X-ray reflectivity data (dots) and error bar (solid line) for a [YBCO (9 u.c.)/LCMO (26 u.c.)]×10 SL SrTiO$_3$. **(b)** The after growth RHEED image for the same SL on a SrTiO$_3$ substrate. White triangular markers indicate the weak half-order signal which is attributed to the *Pbnm* crystal symmetry of the capping LCMO layer. **(c)** A high angle annular dark field scanning transmission electron microscopy image of the YBCO/LCMO interfacial region. Labels indicate different layers.

the reported bulk value for optimal stoichiometry [111]. Furthermore, in an effort to investigate the structural quality of the interfacial region, high angle annular dark field (HAADF) scanning transmission electron microscopy (STEM) measurements were made. In Figure 3.1(c), an HAADF STEM image for the YBCO/LCMO film is shown which exhibits a defect free and atomically sharp interfacial region.

In order to establish the electronic qualities of the samples, we investigated the dc transport properties of single layer YBCO and LCMO films and the SL. Figure 3.2 shows resistivity versus temperature for single layers of YBCO (left axis) and LCMO (right axis). As seen for the YBCO film, the superconducting transition T_c takes place at 93 K attesting to the proper optimally doped stoichiometry. In the case of the LCMO sample, the metal-to-insulator transition takes place at $T_{MI} = 212$ K (inflection point). Note, the previously reported values of T_{MI} for LCMO films grown under similar conditions (e.g., substrate, thickness etc.) but without the use of interval deposition

are typically <170 K [108]. In a conventional growth to achieve an elevated T_{MI} as in our films, significantly increased fabrication temperatures would be required which is a detrimental constraint on cuprate growth [112]. The stabilization of material phases outside of regions of thermodynamic stability is a hallmark of interval deposition, and the electronic and magnetic properties of LCMO are known to depend sensitively on stoichiometry and the presence of defects [31, 113]. Together, these help explain the origin of the enhancements seen in the spectroscopy data below. In addition, the temperature dependent resistance for the SL is plotted on the bottom left axis of Figure 3.2. A suppression in the critical temperature $T_c = 56.7$ K is observed and is most likely the result of hole depletion through interlayer charge transfer as corroborated by the XAS data below.
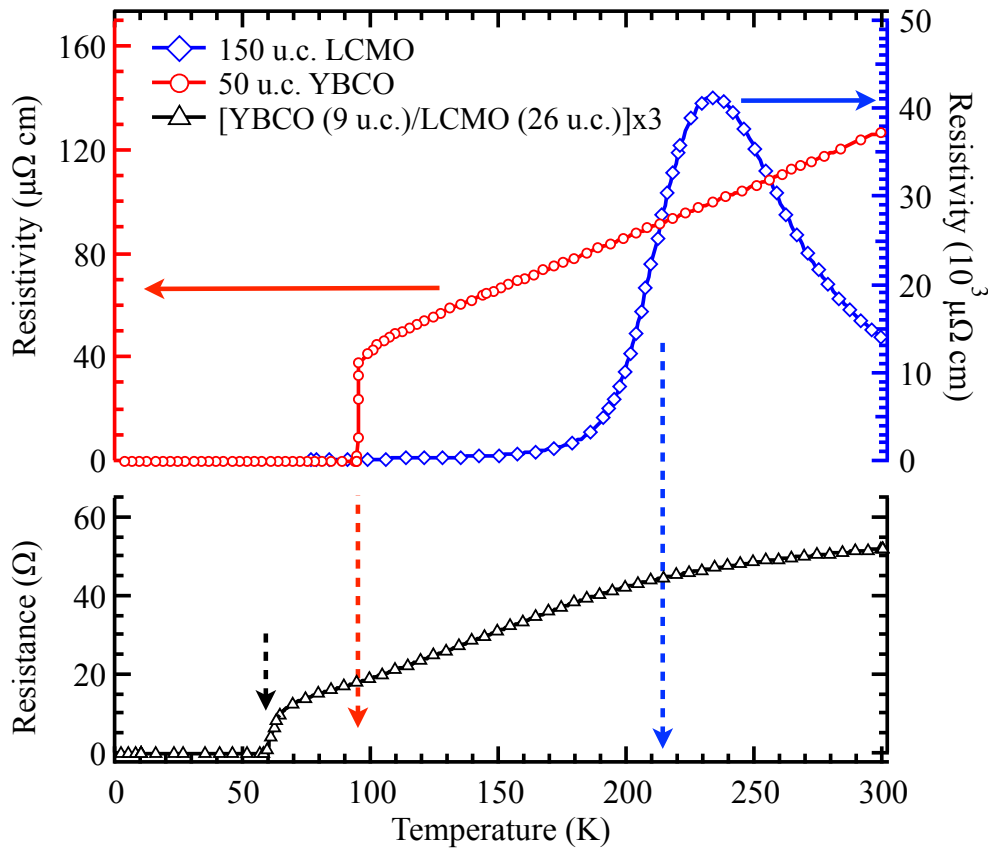

Figure 3.2: **Transport measurements.** Temperature-dependent dc transport for 50 u.c. YBCO and 150 u.c. LCMO single layers and the [YBCO (9 u.c.)/LCMO (26 u.c.)]×3 SL on SrTiO$_3$ substrates. Measurements were performed in the conventional *van der Paw* configuration.

3.2.2 Enhanced Electronic and Spin Reconstructions

Next we explored the electronic and magnetic structure with XLD and XMCD resonant soft X-ray spectroscopies. The experiments were carried out at the 4-ID-C beamline of the Advanced Photon Source in Argonne National Laboratory. In the XLD studies at the Cu L edge, we investigated the orbital occupation by measuring the difference in absorption for polarizations in the ab-plane and along the c-axis, while the XMCD experiments at the Cu and Mn L edges obtained information regarding element specific magnetic moments by measuring the differences in the absorption of right and left circular polarizations. Spectra were recorded at an incident angle of 15 degrees out of plane simultaneously in both fluorescence yield (FY) and total electron yield (TEY) acquisition modes.

The linear polarization-dependent Cu L_3 absorption spectra of the SL is presented in Figure 3.3(a). First we consider the bulk sensitive FY data set which shows the strong XLD expected for the Cu^{2+} ($3d^9$) state of cuprates [44, 114]. Note, the in-plane signal stems from formally divalent Cu within the CuO_2 sheets. Several important features can be identified in the spectrum of which the excitonic line near 931 eV is the most prominent and corresponds to transitions from the Cu $2p$ core levels into the unoccupied bands of mainly Cu $d_{x^2-y^2}$ orbital character ($2p^63d^9 \rightarrow 2p^53d^{10}$). A clear shoulder is observed on the high energy side of the white line. The shoulder is ascribed to transitions coupled with Cu ligand hole states ($2p^63d^9\underline{L} \rightarrow 2p^53d^{10}\underline{L}$) and is the well-known signature of the Zhang-Rice state [76]. Another important feature of the FY spectrum is connected to the c-axis polarization, where the maximum of the absorption peak is shifted by 0.3 eV to higher energy; the larger number of ligand hole states in the chains transfer spectral weight from the excitonic line to the high energy shoulder. Since the $d_{z^2-r^2}$ orbital of the CuO_2 planes is occupied, the out of plane polarization mainly probes unoccupied states from monovalent Cu in
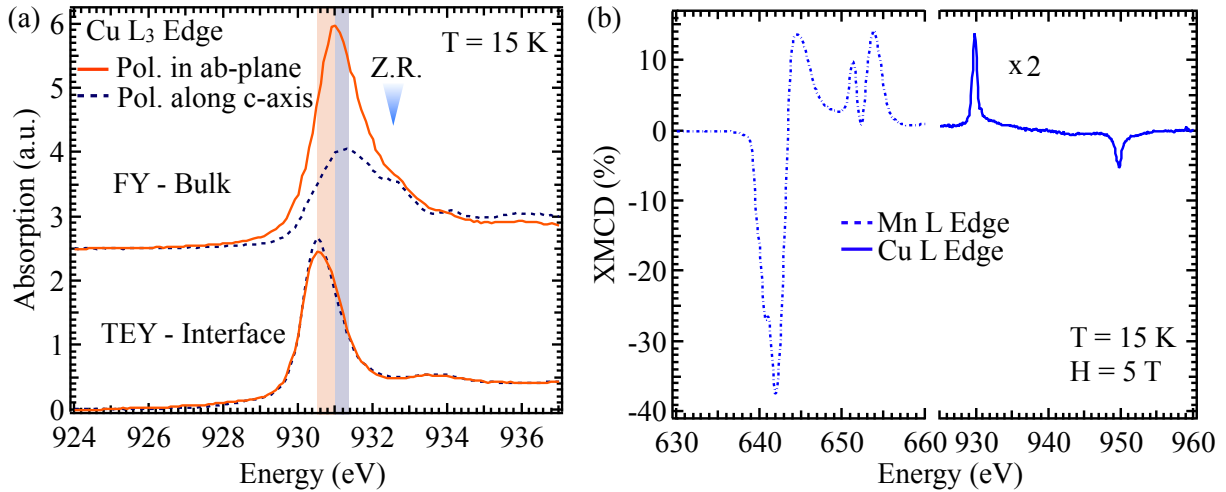
Figure 3.3: **Soft X-ray spectroscopies of the [9 u.c. YBCO/ 26 u.c. LCMO]×3 SL on SrTiO$_3$.** **(a)** XLD measurements at the Cu L$_3$-edge. The top and bottom sets of spectra correspond to FY and TEY detection modes, respectively. Due to TEY's shallow probing depth, only Cu at the first interface predominantly contributes to the Cu L intensity in this mode. **(b)** XMCD measurements at the Mn (left) and Cu (right) L-edges in TEY. Note, to rule out artifacts the XMCD data sets were checked at both magnetic field orientations.

the chains of $d_{z^2-y^2}$ orbital character.

In the TEY data, distinct transformations in polarization dependence and lineshape manifest in the spectra indicating charge transfer across the interface leading to a reconstruction in the orbital scheme for interfacial Cu ions. As indicated in Fig. 3(a), the position of the Cu white line is shifted by 0.5 eV to lower energy in the TEY spectrum, which exceeds the value (0.4 eV) reported in the prior study. This substantial chemical shift is the mark of interfacial charge transfer. Through a comparison to Cu^{1+} and Cu^{2+} reference materials, an approximate calculation yields a charge transfer amplitude of 0.25e per copper ion [115]. Furthermore, the shoulder at high energy is not observed in the TEY data confirming the depletion of holes from the YBCO region of the interface. While the evolution in the amplitude of the high energy shoulder is a common feature of YBCO XAS doping profiles, the shift in the white line is unexpected [44]. Previously, this has been attributed to the reconstruction of the $d_{z^2-r^2}$ orbital through the formation of a covalent bond with Mn through apical oxygen across the interface [105, 116]. Confirming this picture, the large linear

dichroism of the bulk is no longer present, and the absorption along the c-axis now even surpasses that of the the in-plane for the TEY spectrum.

Finally, we turn our attention to magnetism on Cu and Mn. Figure 3(b) shows the XMCD spectra at both the Mn and Cu L edges acquired in TEY mode. As anticipated for a FM system, the strong magnetic dichroism reaches a maximum value of 37.4 % at the Mn L_3 edge. On the Cu L edge, however, only a moderate magnetic signal is present, which indicates an uncompensated magnetic moment on Cu near the interface. From the sign of the XMCD on both Mn and Cu edges, an antiparallel alignment of Cu and Mn moments coupled across the interface can be deduced. The magnitude of the dichroism (6.9 %) a the Cu L_3 edge is up to a *factor five larger* than the previously reported values providing additional evidence for the high quality of the interface [104]. The measurements at the Cu L-edge were repeated at 100 mT without loss in the magnitude of the magnetic dichroism.

So far, only qualitative assessments of the induced moment on Cu at the interface have been reported [103, 104]. Few experimental techniques combine a sensitivity to buried multilayers interfaces and element specific measurements of magnetic moments. While the magnitude of the moments cannot be read directly from XMCD spectra, through an application of the sum rules both the orbital and spin components can be obtained for a specific element [117, 118]. According to the XMCD sum rules, the orbital and spin parts can be calculated as follows:

$$m_{orbital} = -\frac{4q}{3r}(10 - n_{3d}) \tag{3.1}$$

$$m_{spin} = \frac{-6p - 4q}{r}(10 - n_{3d}), \tag{3.2}$$

where $m_{orbital}$ and m_{spin} are the orbital and spin magnetic moments given in μ_B/atom, respectively. The integrals p, q, and r are indicated in Figure 3.4, and n_{3d} is the $3d$ electron occupation number.
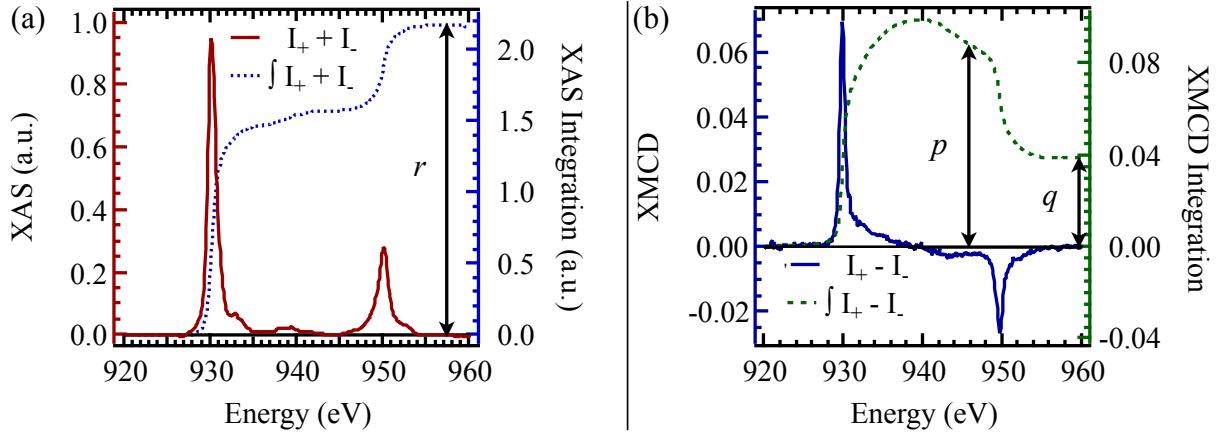
Figure 3.4: **Sum rules applied to the interfacial Cu XMCD signal. (a)** The unpolarized Cu $2p$ XAS spectrum (solid line) from TEY with edge jump removed. The integral over the L edge (dashed line) is plotted as a function of energy. The quantity r is the integral over the entire edge. **(b)** The Cu $2p$ XMCD spectrum (solid line) from TEY. The integrals (dashed line) over the L_3 and L edge are given by p and q, respectively.

Equation 3.2 has been simplified by ignoring the quantity $\langle T_z \rangle / \langle S_z \rangle$, where T and S are the dipole and spin operators, respectively. The omission of these terms has been shown to introduce small (a few %) and offsetting errors [119]. The lack of orbital polarization found in XLD for interfacial Cu lends further support to the use of this approximation. The orbital component, as expected, is quenched by the crystal field with $m_{orbital} = -0.02451 \ \mu_B/Cu$, while $m_{spin} = -0.30791 \ \mu_b/Cu$, which agrees with current theoretical calculations [107].

3.3   Conclusion

In summary, our resonant soft X-ray spectroscopy study of the cuprate-manganite interface has confirmed the presence of both spin and orbital reconstructions. We observed increases in the dichroic signal and the chemical shift at the Cu L edge signaling an enhancement in the induced moment on Cu and the degree of interlayer charge transfer, respectively. Sum rules calculations find a spin moment of 0.3079 μ_B/Cu. Furthermore, an increase in T_{MI} has been observed for manganite layers grown with interval deposition, which is fundamentally related to its magnetic

and electronic properties.

Chapter 4

Interfacial Controlled Carrier Doping of a High-Temperature Superconductor

In this chapter, we examine an experimental exercise to direct the phase diagram of a high-T_c cuprate using interfacial electron-doping by means of a heterojunction with a colossal magnetoresistive manganite. Initially, the heterojunction between $YBa_2Cu_3O_7$ and $La_{2/3}Ca_{1/3}MnO_3$ behaves in a parallel manner to that of chemical control, i.e., the carrier density is regulated by the interface. The introduction of manganite layers into the heterostructure triggers a thickness dependent suppression in the superconducting transition temperature. Analysis of the polarized x-ray absorption spectrums on Mn and Cu reveals a flow of electronic charge across the interface, where the depleted electrons directly enter the CuO_2 planes unbalancing the standard carrier distribution between infinite layers and charge reservoir blocks, despite this the heterojunction conforms with the conventional $YBa_2Cu_3O_{7-\delta}$ phase diagram. Until a breakdown in the charge transfer process, defined by the spatial limit of charge reconstruction, blocks access to the electron-doped superconducting phase. As electron flow abates, the average Mn valence declines to the as-grown value ($Mn^{3.33+}$) facilitating the development of spin and orbital reconstructions at the interface.

4.1 Introduction

The discovery of an interface based method for manipulating a material's phase diagram would be elementary to not only tailoring the material's electronic attributes but to also creating systems that have no bulk counterparts. One possible inroad into this problem has emerged in the field of ultra-thin superlattices (consisting of individual layers approaching 1 unit cell (u.c.) of thickness),

where near interface reconstructions are capable of stabilizing electronic phases previously only accessible through chemical doping of parent compounds. Oxide heterostructures have displayed a particularly strong susceptibility to interlayer charge redistribution derived from incompatibilities in electronic boundary conditions making them ideal candidates to explore this hypothesis [79, 120, 121, 122, 123]. Moreover, the inherent electron correlations give rise to rich phase diagrams with pronounced coupling amongst lattice, spin, charge, and orbital degrees of freedom leading to emergent phases and functionalities at heterojunctions [124, 125].

The promise of fostering these type of unrealized electronic states has sparked interest into a system composed of a high-T_c superconductor $YBa_2Cu_3O_7$ (YBCO) and a colossal magnetoresistive manganite $La_{2/3}Ca_{1/3}MnO_3$ (LCMO). Early research hinged on antagonism amidst superconductivity and ferromagnetism, where the singlet structure of Cooper pairs must be reconciled with the parallel alignment imposed by the ferromagnet's exchange interaction [98, 126, 101]. Indeed several studies have associated depressed critical temperatures and magnetization in YBCO/LCMO superlattices with long range proximity effects [99, 127, 128, 109, 129, 100, 130], yet the macroscopic validity of this interpretation remains unclear. Of greater interest to this study are the overshadowing impacts of charge, spin, and orbital reconstruction present at the interface [104, 105, 103, 131, 132]. In particular, x-ray spectroscopies have established that electron transfer from Mn to Cu ions takes place through a covalent bond at the interface. Additionally, tunneling and electron energy loss spectroscopies have set an upper limit on the region of electronic alteration at approximately 1 nm (slightly less than 1 YBCO unit cell u.c.). Despite this progress, conflicting views remain about the direction of charge flow and the electronic profile of the reconstructed region. To this end, ultrathin SLs which are true interface materials unclouded by the admixture of bulk-like properties would allow for a clearer analysis of these reconstructed states and possibly the revelation of emergent phases, e.g., electron-doped superconductivity in a formally hole-doped

66

cuprate.

We begin by investigating the consequences of charge reconstruction for interfacial states, specifically the implications of electron doing on CuO_2 planes in a formally hole doped superconductor. As shown schematically in Figure 1(b), we fabricated superlattices (SL) consisting of [YBCO (2 u.c.)/LCMO (N u.c.)]$_m$ with $N = 1, 2, 3$ and $m = 20, 15, 9$, respectively on $SrTiO_3$ substrates. Through x-ray spectroscopy and diffraction, depleted electrons are established to directly enter the CuO_2 upsetting the conventional balance of charge throughout the u.c. Electron transfer into the conducting planes behaves as a dial to tune through the copper oxide phase diagram without the need for chemical substitution or oxygen reduction. Commensurate with the observation of charge transfer, the LCMO layers advance into a canted AFM state. However, electron transfer ceases before electron-doped superconductivity is reached. Upon further increasing the manganite layer thickness the transferral of electrons to YBCO rapidly diminishes, as the average Mn valence decreases to $Mn^{3.33+}$ (the expected value for the chosen A-site ratio). This breakdown in electron transfer was explored in a series of YBCO/LCMO SLs with $N = 5, 10, 15, 20, 30$ and $m = 7, 6, 5, 4, 3$, respectively. The cessation in charge transfer coincides with previous limits placed on the area of electronic alteration. The shift in Mn valence draws the system into the ferromagnetic region of the LCMO phase diagram, and magnetic dichroism at the Mn L edge scales with the reduction in valence. The Mn magnetic signal is found to be strongly field dependent suggesting electronic phase-separated phenomena. Orbital and spin reconstructions on interfacial Cu develop alongside the rise in Mn $3d$ count, as evidenced by linear and magnetic dichroic signals at the Cu L edge.

4.2 Results and Discussion

4.2.1 Evolution of T_c with N

Figure1(a) shows the temperature dependent resistivity for the $N = 1, 2, 3$ SLs in which varying the LCMO thickness obtains a clear superconductor-insulator (S-I) transition. The samples were measured in van der Pauw geometry, and the in-plane resistivity ρ_{ab} was calculated with a parallel resistor model.

$$\rho_{ab} = R_S \times t_{YBCO} \tag{4.1}$$

Measurements of the Mn valence (see below) indicate that the LCMO layers are inside the AFM-insulator section of the phase diagram [30]. In this case, the current will be shunted to the YBCO layers, and the resistivity is only a function of the total YBCO thickness t_{YBCO} [133]. As shown in Figure1(a), T_c plummets considerably from 50 to 12.5 K, when N increases by the smallest possible margin from 1 to 2. Here T_c is taken to be the temperature at which the sheet resistance falls to zero. Both samples exhibit the well-known non-Fermi liquid linear T-dependence [134], and the temperature T_0, at which ρ_{ab} deviates from linearity, shifts higher for $N = 2$ (see Figure B.1 for linear plot). At $N = 3$ the superconducting phase remains unrealized down 2 K, and the sample displays insulating behavior in its place. The degradation in normal state transport properties and following S-I transition is consistent with reduced carrier doping in $YBa_2Cu_3O_{7-\delta}$ [135].

However, an accounting of the carrier concentration within the SLs is required to properly establish the origins of suppressed superconductivity with N. In the undoped compound $YBa_2Cu_3O_6$ the two inequivalent Cu sites, $Cu(1)O_3$ chains and $Cu(2)O_2$ planes, would be in a $3d^{10}$ and $3d^9$ configuration, respectively, and the O sites would be in a $2p^6$ configuration for a strictly ionic model. Upon oxygen doping to $YBa_2Cu_3O_7$, previous experiments and theoretical calculations
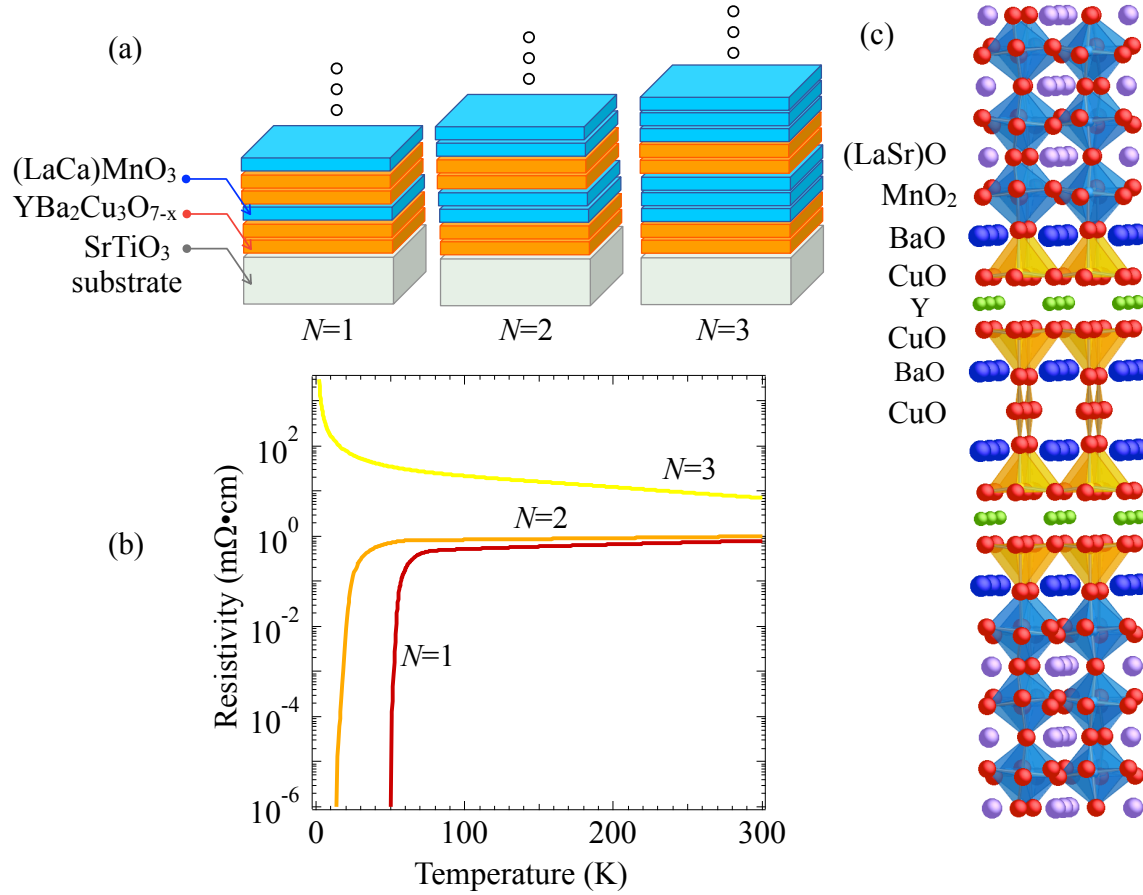
Figure 4.1: **Electronic transport measurements and superlattice schematics**. **(a)** Four point probe electrical transport measurements of superlattices with $N = 1, 2, 3$. A transition from super-conductor to insulator takes place at $N = 3$. **(b)** Block schematics of superlattices studied. Films are composed of alternating layers: $YBa_2Cu_3O_7$ layers (blue blocks) and $La_{2/3}Ca_{1/3}MnO_3$ layers (orange blocks). All films were grown on $SrTiO_3$ substrates (gray blocks). We label the films on the basis of $La_{2/3}Ca_{1/3}MnO_3$ thickness as $N = 1, 2, 3$ u.c. with a constant $YBa_2Cu_3O_7$ layer thickness of 2 u.c. This give superlattices with the structure [YBCO (2 u.c.)/LCMO (N u.c.)]$_m$ ($N = 1, 2, 3$ u.c. and $m = 20, 15, 9$). **(c)** Crystal structure of the $N = 3$ superlattice. Note the two inequivalent copper sites: Cu(1) in the CuO_3 chains and Cu(2) in the CuO_2 planes. CuO layers are absent from both top and bottom interfaces.

on the electronic structure determined that the $3d$ count of the Cu(1) atoms decreases by one, and

the remaining holes will form on the O sites (i.e. a charge-transfer model) with approximately

0.6 holes per chain unit and 0.2 holes per plane unit [43, 44, 45, 46]. The holes are introduced

into the electronic structure by oxygen doping within the CuO layers of the chains. In ultrathin

heterostructures, missing CuO layers at the interface will have a dramatic impact on T_c and must be considered first in an analysis of T_c reduction.

4.2.2 Structure

The structure of the interface plays an integral role in determining the properties of ultrathin superlattices. In YBCO/LCMO heterostructures, the formation of a covalent bond between Cu and Mn at the interface has been proposed as the origin of reconstructions in orbital, charge, and spin degrees of freedom [104]. In fact, the goal of the current study is to leverage this unique bonding to facilitate interfacial charge transfer and manipulate the YBCO phase diagram. Furthermore, the covalent bond with Cu in the CuO_2 planes requires the removal of the CuO layers at the interface that leads to serious consequences in terms of carrier doping in the YBCO layers. When the YBCO layer thickness is limited to 2 u.c., the loss of chains at both top and bottom interfaces hypothetically cuts hole doping within the layer in half and should reduce T_c down to 56 K. Therefore an understanding of the interfacial structure is a prerequisite for interpreting results.

The termination of the interfaces remains a contentious theme of current research. Some transmission electron microscopy (TEM) studies have concluded that the bottom interface terminates without the loss of CuO layers [138], while others others reported missing chain layers at both bottom and top interfaces [139]. Originally, this disagreement was thought to stem from the growth technique (pulsed laser deposition versus sputtering) employed, however recent experiments have removed this possibility [140]. For the top interface, there is agreement that the CuO layers are missing which gives a La/CaO—CuO_2 interface.

To resolve these issues within this study, high-angle x-ray diffraction and reciprocal space mapping was carried out at beamline 33-BM-C of Argonne National Labs (see Figure 1.7). Specular x-ray reflectivity along the (00L) crystal truncation rod combined with a series of simulations
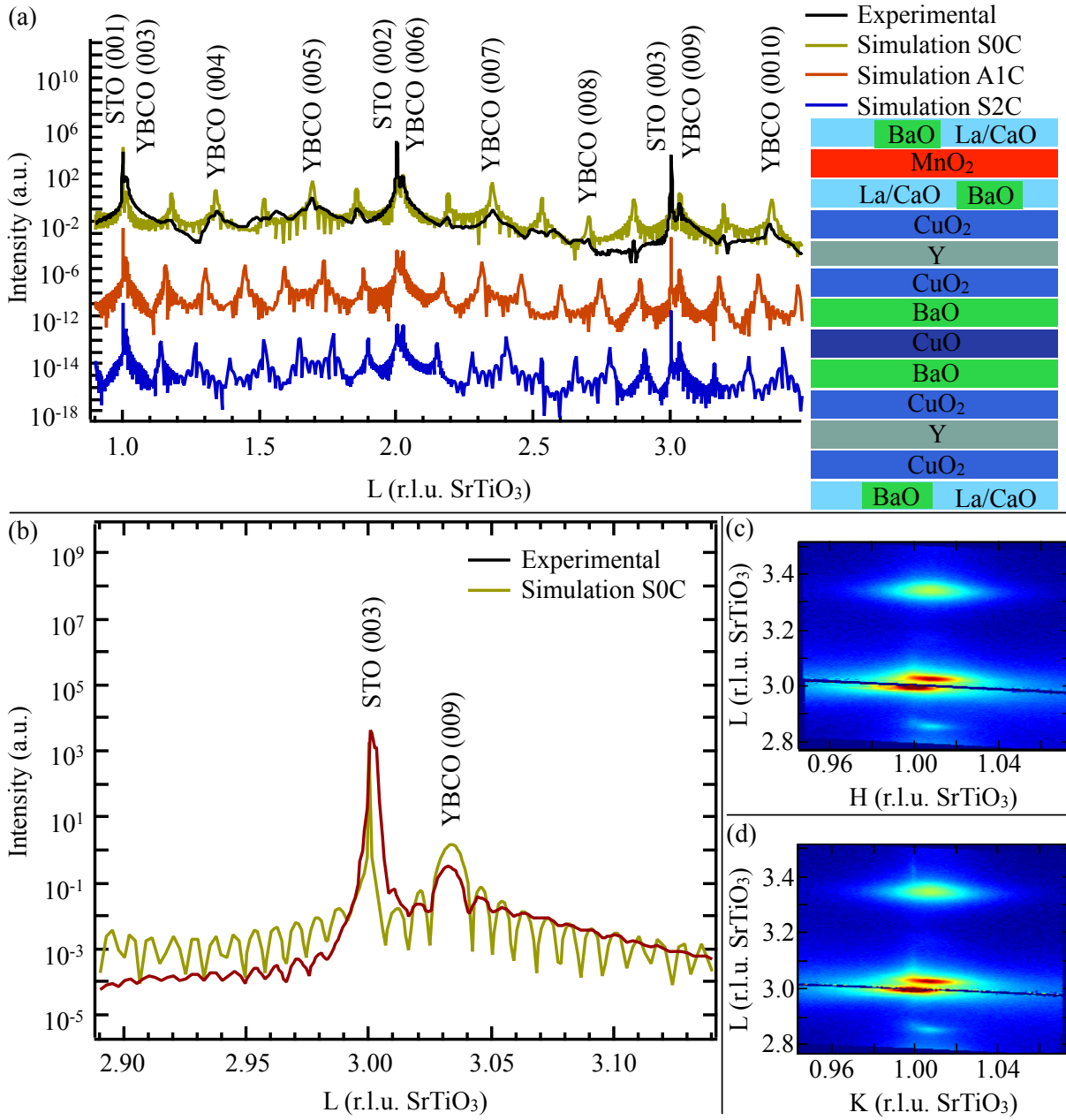
Figure 4.2: **Structural analysis of the [YBCO (2 u.c.)/LCMO(1 u.c.)]x20 SL. (a)** Specular x-ray reflectivity along the (00L) crystal truncation rod (black curve). Simulations of the reflectivity data for symmetric interfaces with CuO layers missing at top and bottom interfaces (S0C), asymmetric interfaces with CuO missing at one interface (A1C), and symmetric with CuO present at top and bottom interfaces (S2C). Simulations displaced vertically for clarity. Inset: Block schematic of S0C model. **(b)** Specular x-ray reflectivity around the STO (003) and simulation S0C. **(c)** Reciprocal space map around STO (103) **(d)** Reciprocal space map around STO (013).

picked out a unique interfacial stacking and allows for the determination of c-axis structural parameters. The experimental diffraction pattern for the N = 1 samples is displayed in Figure 1.7(a)

alongside three simulations, which are displaced vertically for clarity. The experimental pattern includes the expected Bragg peaks from a c-axis oriented thin film and additional reflections between the Bragg peaks corresponding to the super-period of the heterostructure. The simulated patterns were constructed with the reflectivity fitting program GenX [141]. Custom atomic models can be directly inputted to simulate the diffraction spectra. The atomic arrangement of the models are based on the principles of chemical matching for layer stacking in ABO_3 perovskites (for more details see the accompanying chapter on $YBa_2Cu_3O_7/SrTiO_3$). Although this gives six possible stacking configurations, we only considered the possibilities supported by the previous TEM experiments. Three models were tested: symmetric interfaces with chains missing at top and bottom interfaces (S0C), asymmetric interfaces with chains missing at one interface (A1C), and symmetric with chains present at top and bottom interfaces (S2C). Only the S0C model was able to match the experimental pattern. Differences between the simulation and experimental pattern are due to interfacial roughness and modulations in the super-period, which were not accounted for within the S0C model (shown schematically as an inset to Figure 1.7(a)). While mixing of La/CaO and BaO at the interfaces was taken into consideration, the possibility of patches, where interfacial chains are present, was not accounted for in the S0C model. Given the conflicting TEM data, these patches might exist. A magnified view around the STO (003) rod is shown in Figure 1.7(b). The YBCO (009) peak is visible, and Keissig fringes are present within the pattern. Based on the fringes and location of superlattice reflections, there are exactly 20 repeats in the SL with a period $\Lambda = 22.9841$ Angstroms. The location of the YBCO (009) rod gives a c-axis parameter $c = 11.5571$ Angstroms. In the bulk, the c-axis parameter of YBCO evolves as a function of doping and correlates closely with T_c [142]. The value of the c obtained for the SL is shorter than expected — even compared to over-doped samples.

The accommodation of misfit strain can be rule out as a possible source of the unusually short

lattice constant. In heteroexpitaxy, the growing film locks into atomic registry with the substrate, which generates epitaxial strain. The degree of strain depends upon the mismatch between in-plane lattice parameters. STO has a cubic lattice with $c = 3.9045$ Angstroms, while YBCO has an orthorhombic lattice with in-plane parameters $a = 3.8227$ and $b = 3.8872$ Angstroms. Epitaxy will result in the YBCO lattice undergoing tensile strain. In Figures 1.7(c, d), reciprocal space maps around the STO (103) and (013) rods, respectively, show that the $n = 1$ SL is relaxed. In both figures, the YBCO (108)/(018), (109)/(019), and (1010)/(0110) rods do not line up with their respective substrate peaks, hence the heterostructures have relaxed to their bulk in-plane parameters.

4.2.3   Charge Transfer from LCMO

X-ray diffraction experiments along with modeling have established that the chain layers are not present at both top and bottom interfaces in the SLs. Hence the two YBCO u.c. share only one set of chains (see Figure 1.1(c)), which cuts their doping level in half (one hole per u.c.). This hypothetically limits $T_{c,max}$ to approximately 55 K and is the starting point for further calculations [142]. In our model, the holes within the YBCO u.c. are filled in through interfacial electron transfer. Assuming a maximum valence shift to Mn^{4+} (shown experimentally below) and given the constraint of epitaxy (u.c. matching at the interface), the manganite layers provide $-0.67e \times N$ per two YBCO u.c. For $N = 3$, the translocated electrons exactly cancel the remaining holes, and the system should be rendered insulating. In the $N = 1, 2$ SLs transition temperatures fall within the outlined range (55 - 0 K), however predicting the exact behavior of these intermediate cases presents formidable challenges: (1) The incomplete YBCO layers contain an unknown rearrangement of carriers. (2) While diffraction experiments favor a MnO_2—BaO-CuO_2 termination, the probable existence of SrO—CuO patches provide an unaccounted for reservoir of holes. (3) The carrier concentration within the CuO_2 planes depends sensitively on the distribution of transferred
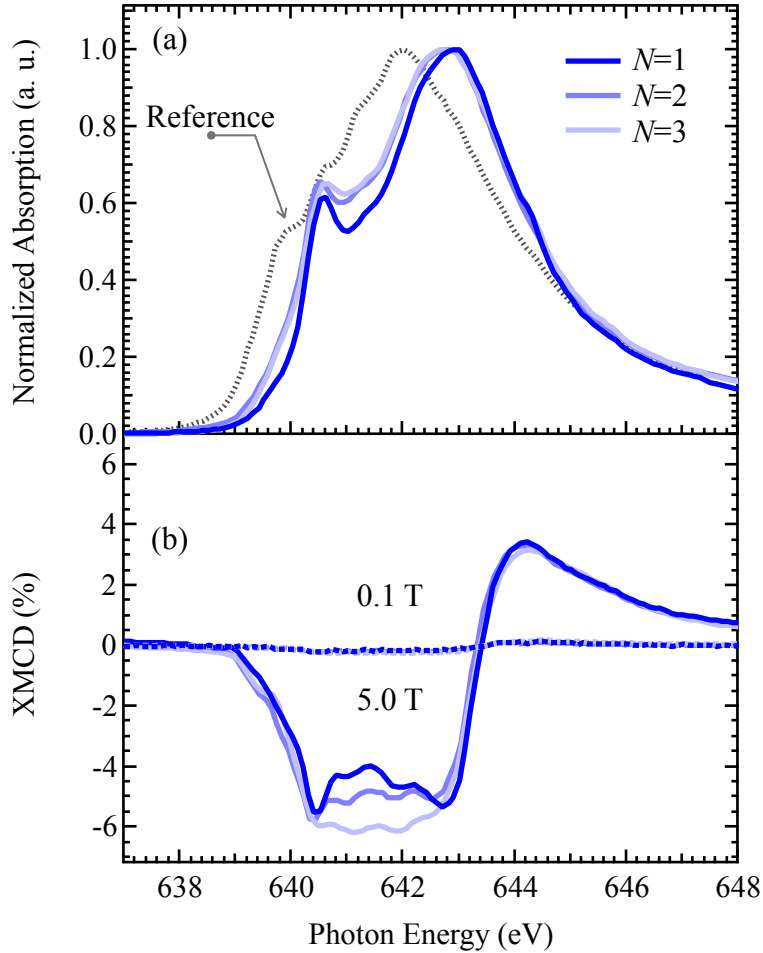
Figure 4.3: **Mn valence and magnetism. (a)** Circularly polarized average for superlattices with dependence on N at the Mn L_3 edge. The valence state of Mn is fixed close to 4^+ rather than the expected 3.33^+. For comparison, a 150 uc LCMO reference film with a nominal valence of 3.33^+ is shown. **(b)** X-ray magnetic circular dichroism measurements of superlattices with dependence on magnetic field. Strong field dependence points to a canted AFM state.

electrons. For these reasons, x-ray absorption spectroscopy (XAS) was utilized to measure and track the charge flow out of the manganite layers and into the cuprate layers.

To uncover the origin of the transferred charge, Mn L edge XAS spectra were recorded with left circularly (I^-) and right circularly polarized (I^+) light at 15 K. The polarization averaged absorption spectra for the SL are compared with that recorded on a 150 uc thick $La_{2/3}Ca_{1/3}MnO_3$ film ($Mn^{3.33+}$) in Figure 3(a). The chemical shift to higher photon energy and the pronounced doublet feature, found in the SLs, are typical of a $CaMnO_3$ spectra, which indicates that the Mn ions have

increased valency to +4 from +3.33 by transferring electrons to the YBCO layers [19]. The similar Mn oxidation state for each heterostructure also implies that the net amount of electron transfer through the interface is $-0.67e$ per Mn ion. Furthermore, all SLs show a weak x-ray magnetic circular dichroism (XMCD) signal (Fig. 3b) in a 5 Tesla magnetic field, which is reprsentative of an AFM state. The disappearance of the XMCD signal with the reduction of magnetic field to 0.1 Tesla affirms that the manganite layers are not ferromagnetic, which agrees with the phase diagram of bulk $La_{1-x}Ca_xMnO_3$. Near $x = 1$ (i.e. Mn valency close +4) the system is antiferromagnetic [31]. The small XMCD signal in high field stems from spin canting.

4.2.4 Modification of the Electronic Structure within the YBCO Layers

Modifications to the cuprate electronic structure, in this case due to incorporation of depleted electrons, can be monitored by probing changes in the unoccupied density of states. Here we have utilized XAS, which is also sensitive to the orbital occupation and symmetry at the different Cu sites. The polarized Cu L_3 edge x-ray absorption spectra are reported in Figure 1.2(a, b) for both ab-plane and c-axis. Spectra were acquired in both bulk sensitive total fluorescence yield (TFY) and surface sensitive total electron yield (TEY) mode. Due to the ultrathin nature of the YBCO layers, there is no significant difference between the two sets of data, and only the TFY data will be shown here. The asymmetric ligand environment around Cu(2) leads to a preferentially empty $3d_{x^2-y^2}$ orbital and hence a strong x-ray linear dichroism (see Figure B.2). Here, the signal has been normalized to edge max for ease of comparison. The absorption signal with electric field vector (**E**) parallel to the ab-plane (I_{ab}) mainly probes state associated with the Cu(2) $3d_{x^2-y^2}$ orbital, while **E** parallel to c-axis (I_c) detects states with Cu(1) $3d_{z^2-y^2}$ orbital character. [143]. I_{ab} consists of a sharp peak (the so called white line) stemming from Cu(2) $3d^9 \rightarrow$ Cu(2) $2\underline{p}3d^{10}$ transitions at about 931.2 eV and a shoulder on the high-energy side at 932.53 eV, designated Zhang-Rice (ZR),
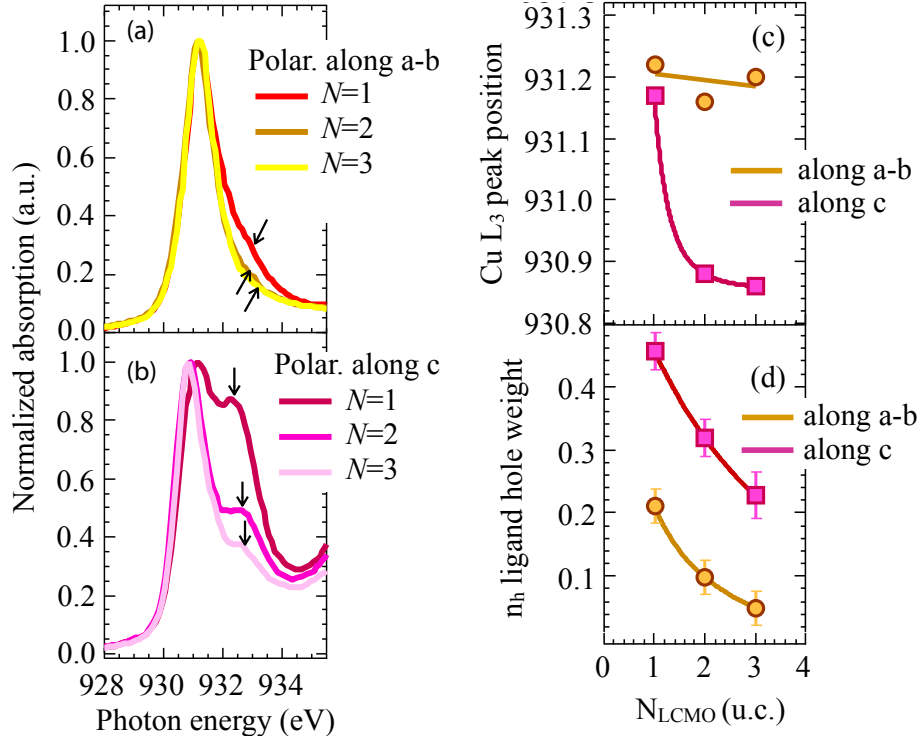
Figure 4.4: **Cu electronic structure and ligand weight analysis.** (a) and (b) X-ray Linear Dichroism (XLD) measurements at the Cu L_3 edge at 15 K with the electric-field vector $\mathbf{E}\|$ab and $\mathbf{E}\|$c, respectively. Arrows indicate the progression of the ZR and satellite peak as a function of LCMO thickness. The relative strength of the ZR and satellite peak measure the concentration of holes on neighboring oxygen sites. (c), Main peak energy shift with dependence on N taken from graphs (a) and (b). (d) Ligand hole weight plotted as a function of LCMO layer thickness for both polarizations. The ligand hole weight was calculated from XLD spectra as described in supplement.

from Cu(2) $3d^9\underline{L} \rightarrow$ Cu(2) $2\underline{p}3d^{10}\underline{L}$ transitions, where $\underline{L}$ denotes a $2p$ hole on neighboring oxygen sites. For I_c, the lower-energy contribution at about 931 eV is associated with mainly Cu(1) $3d^9$ $\rightarrow$ Cu(1) $2\underline{p}3d^{10}$ transitions, and the high energy satellite peak arises due to Cu(1) $3d^9\underline{L} \rightarrow$ Cu(1) $2\underline{p}3d^{10}\underline{L}$ transitions [44].

The intensity of Cu spectral lines are directly related to the number of unoccupied states involved providing a measure of hole occupancy in Cu $3d$ orbitals. Throughout the SL series, the dominant contribution to the unoccupied density of states remains transitions from Cu(2) of $3d_{x^2-y^2}$ orbital character (WL). However, a portion of this spectral weight is redistributed to the ZR shoul-

der. As discussed above, the dopant holes in the CuO$_2$ planes form on oxygen sites, and the $3d$ count on planar Cu(2) sites stays fixed. XAS studies clearly show that the peak position of the Cu(2) main absorption line does not shift with doping (see Figure 1.2(c)) [44, 144]. Due to covalancy between Cu d and O p orbitals, the hole on a neighboring oxygen site will interact strongly with the localized hole in the Cu(2) $3d_{x^2-y^2}$ orbital leading to the ZR line (see the introduction for a further description of the ZR state). The total spectral weight of the WL and ZR peaks is approximately constant throughout the SL series, and these two peaks only trade intensity as a function of N (see Figure B.2 for plots with post edge normalization). A similar scenario occurs in XAS studies on the effects of oxygen doping in YBCO [44]. This offers an explanation for the diminishing relative intensity of the ZR peak with increasing LCMO layer thickness seen in Figure 1.2(a). For increasing N, fewer holes are present on oxygen sites to interact with the holes on Cu sites, and subsequently these transitions contribute to the WL instead. The situation at the Cu(1) sites in the chains (see Figure 1.2(b)) is analogous, except the $3d$ count increases with a reduction in hole content. Unlike planar Cu(2), dopant holes form on Cu(1) sites as well as neighboring oxygen sites in the chains. Therefore, the total spectral weight (main peak and shoulder) is reduced as a function of N.

To quantify the degree of charge transfer and modification in electronic structure, the ligand hole weight n_h (i.e., the proportion of Cu L$_3$ edge spectral weight corresponding to ligand hole final states) has been calculated from the XAS spectra [145, 146]. (Fitting details can be found in Appendix A.) The ligand hole weight is plotted as a function of N in Figure 2(d) for both orientations of **E**. Since the polarization dependence naturally distinguishes between the two Cu sites, n_h esitmates the hole density within the CuO$_2$ planes (CuO$_3$ chains) for polarization parallel to the ab-plane (c-axis). For the ab-plane, n_h begins well below the value expected for optimally doped YBCO and quickly approaches zero with N, while in the chains n_h begins near the value

found in optimally doped YBCO and is still not fully depressed at $N = 3$ [44]. (See Appendix A for ligand weight analysis of $YBa_2Cu_3O_{7-\delta}$.) From the n_h data sets, we infer that electron transfer takes place first in the CuO_2 planes — then in the chains — and develops as a function of LCMO layer thickness. This behavior reflects the incomplete structure of the YBCO u.c. at the interface, where CuO layers are only present in the middle of each YBCO block (see Figure 1.1(c)). Thereby, a component of depth sensitivity is coincidentally acquired. These findings suggest that the distribution of depleted electrons peaks near the interface and penetrates deeper with increasing N.

4.2.5 Phase Diagram

The charge profile, which emerges from the n_h data set, directly contrasts with expectations based on chemical doping and interface based field effect methods. In XAS studies of gated YBCO thin films, the injected holes entered the CuO_2 planes, as in oxygen doping, indirectly through the chain units, and the majority of these holes remained within the chains themselves offering a profile consistent with chemical control [149]. Only ionic liquid based field effect devices, where carrier concentrations changes up to 8×10^{14} cm^2 can be induced, have successfully altered the carrier density within the planes to the point of reaching the insulating phase [150]. In our samples, the distribution of depleted electrons peaks within the CuO_2 planes and unbalances the conventional doping ratio between the CuO_3 chains and the conducting planes. This distinct arrangement is attributed to the atomic configuration of the interface that allows direct coupling through a Cu-O-Mn bond [105].

In this regard, cuprate-manganite heterojunctions offer the opportunity to explore the superconductor phase in the 123 family outside of the ordinary carrier alignment. While all cuprates contain the fundamental CuO_2 planes, the origins of significant variation amongst optimal transi-
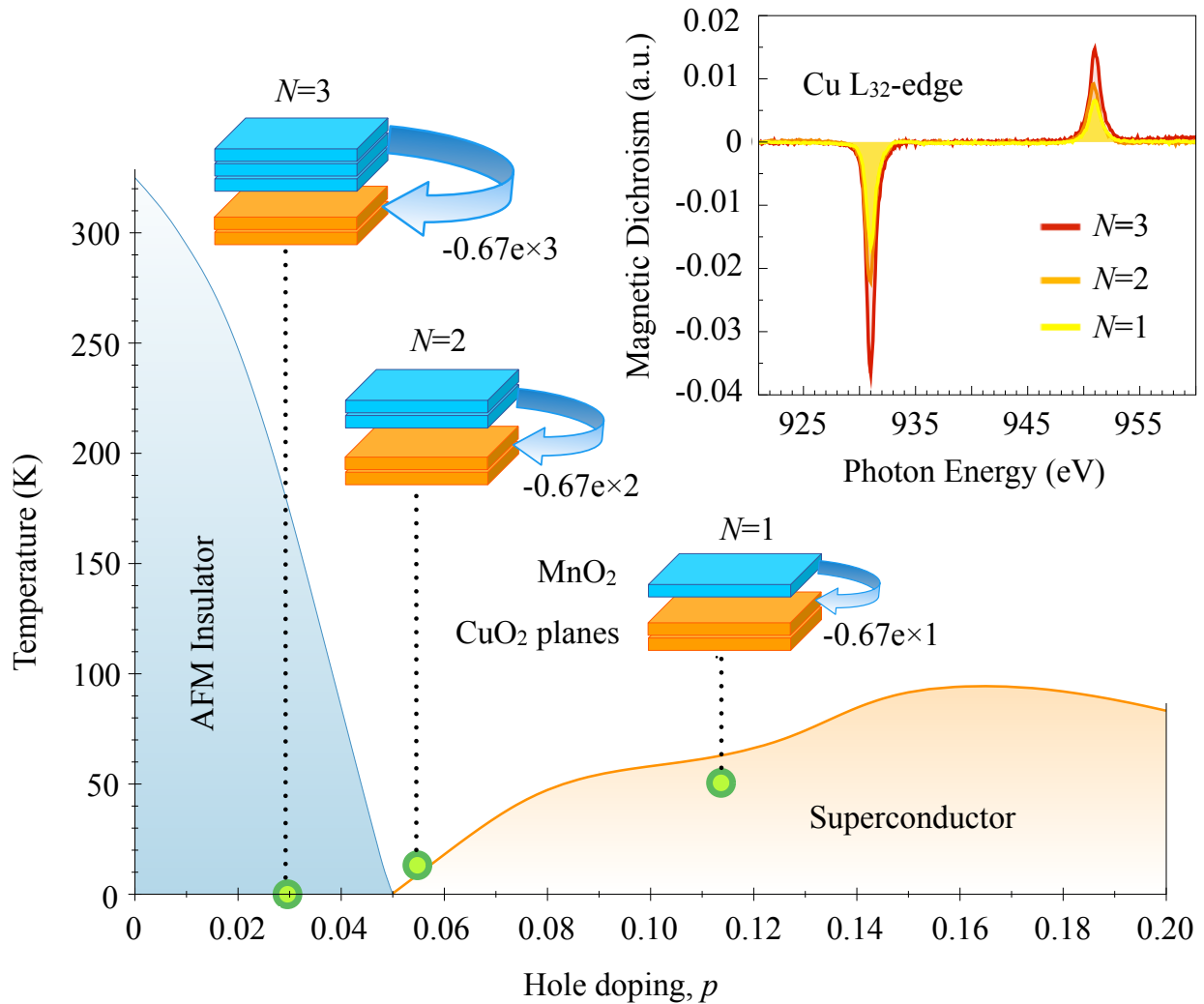
Figure 4.5: **Progression of superlattices on the bulk YBCO phase diagram.** Block schematics show the amount of charge transferred as a function of LCMO layer thickness: $-0.67e \times N$ per two YBCO u.c. Points on the phase diagram calculated from a combination of transport data and ligand weight analysis as described in the supplemental. **(Inset)** XMCD measurements of the Cu L_3 edge recorded at 15 K in a 5 Tesla magnetic field.

tion temperatures across the diverse cuprate families remains a poorly understood topic. Material

dependent alterations within the electronic structure of the layers perpendicular to the planes have

been proposed to play an important role [147]. To test this proposition, the position of the SLs on

the YBCO phase diagram have been plotted in Figure 1.4 [148]. The T_c information was taken from

the transport data, while the level of hole doping within the CuO$_2$ planes resulted from calculations

based on the in-plane n$_h$ (see Appendix A). The SLs fit well into the bulk YBCO phase diagram

and demonstrate the modification in carrier density with LCMO layer thickness. As supporting evidence, the XMCD data at the Cu L edge in a 5 Tesla field has been insetted into Figure 1.4. The size of the XMCD signal scales as a function of N. Weak ferromagnetism in the cuprates stems from the Dzyaloshinskii-Moriya (DM) interaction [151]. For the highly underdoped cuprates (the case for N = 3), long range AFM order is expected, and the DM interaction simply cants the moments along the c-axis. However for the doped cuprates (N = 1 and 2), only short range AFM order survives. A picture of emerging AFM order is inferred commensurate with further advancement into the underdoped region of the phase diagram. In light of the agreement between the experimental data sets and the conventional bulk phase diagram, we find that the electronic structure of the conducting planes remains the single most important factor in determining the superconducting properties of the cuprates.

4.2.6   Electron-Doped YBCO

The phase diagram in Figure 1.4 fails to take into account the full cuprate symmetry (electron-doped superconductors). Upon increasing N, the trend suggests that the electron-doped region will be accessible. However further samples, which were manufactured up to $N = 30$, remained outside of the superconducting state as measured by DC transport (not shown). Given the previous results, the electron transfer should be sufficient to push the system through the electron-doped superconducting phase. Hence, a breakdown in the above paradigm should occur shortly after $N = 3$.

The breakdown in charger transfer was investigated with XAS at the Mn L edge for the $N = 5, 10, 15, 20, 30$ samples. The polarization averaged spectra were taken in TEY mode at 15 K. A shift in the Mn L_3 maximum to lower energy occurs with increasing N, and the doublet feature disappears (see Figure 1.5(a)). In Figure 1.5(b), the L_3 edge maximum is tracked as a function

of N. The location of the edge correlates strongly with the Mn valence state [19]. The respective energies of Mn^{4+} and $Mn^{3.3+}$ are labeled by arrows on the graph. The dashed line is simply a guide to the eye. This series of chemical shifts towards lower energy denotes a decline in the average Mn valence. While a charge profile perpendicular to the interface cannot be obtained directly from the spatially averaged XAS data set, the accumulation of layers farther from the interface which fail to donate charge to the CuO_2 planes of YBCO is expected given the limited range of charge transfer. In spite of conflicting reports, recent experimental and theoretical studies have set an upper limit on the region of electronic alteration to within the first 2 or 3 u.c. [121, 66, 152]. Accordingly,
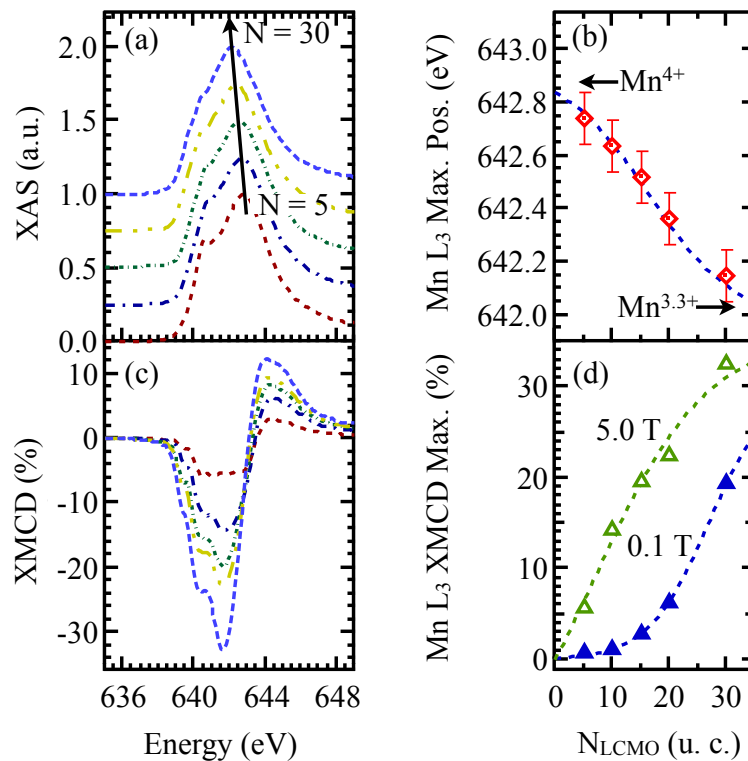
Figure 4.6: **Mn valence and magnetism in thicker heterostructures.** (a) Mn L_3 edge XAS for the $N = 5, 10, 15, 20, 30$ superlattices with offsets for clarity. Measurements were taken at 15 K, and the edge max was normalized to unity. An arrow indicates the series of chemical shifts for the L_3 maximum. (b) Position of L edge maximum graphed against N. Location of Mn^{4+} and $Mn^{3.3+}$ noted by arrows. (c) Mn L_3 edge XMCD for $N = 5 - 30$. Data taken at 15 K and 5.0 Tesla. (d) Maximum of dichroic signal graphed against N. Data sets for 5.0 and 0.1 Tesla indicated. Dashed lines are guides to the eye.

electron transfer into adjacent YBCO layers ceases.

4.2.7 Developing Spin and Orbital Reconstructions

As will be shown, the reduction in Mn valence impacts the magnetic structure of the SLs, as well. In Figure 1.5(c), a strong magnetic dichroism develops at the Mn L edge with increasing N. The modulus of the difference spectra's minima are plotted as a function of N for external fields, 5.0 and 0.1 Tesla (see Figure 1.5(d)). The dashed guides are tapered based on data from a 150 u.c. thick LMCO single layer. A strong field dependence persists across all the SLs, but peaks at $N = 15$. The correlation between increases in both the Mn $3d$ count and magnetic signal stems from the mixture of Mn^{3+} and Mn^{4+} ions that actuates the mechanism of double exchange leading to a ferromagnetic ground state within the manganite layers. The field dependence suggest that LCMO layers are phase-separated, where regions of ferromagnetic metal are inter-dispersed with charge-ordered domains. Below the Curie temperature, the phase separation diminishes with increases in magnetization, i.e., the ferromagnetic metallic phase percolates in reaction to an applied magnetic field [37, 136, 137].

At the interface, spin reconstructions on neighboring Cu sites evolve beside ferromagnetism on Mn. The spin reconstructions can be seen in Figures 1.6(a, b), where the Cu L_3 XMCD signal has been plotted for applied fields of 5.0 and 0.1 Tesla, respectively. For $N = 30$, the magnitude of the dichroic signal is larger at low field, while for the other SLs the signals either switch sign or disappear below the noise floor with a reduction in field. The sign of the dichroism carriers information about the relative alignment of spins (up or down). For example, the $N = 30$ sample displays a positive (negative) Cu (Mn) dichroism, and an antiferromagnetic alignment between Cu and Mn spins at the interface can be inferred. In this case, the small magnitude of the Cu signal suggest that the Cu spins cant in the opposite direction. In a previous article, an antiferromagnetic
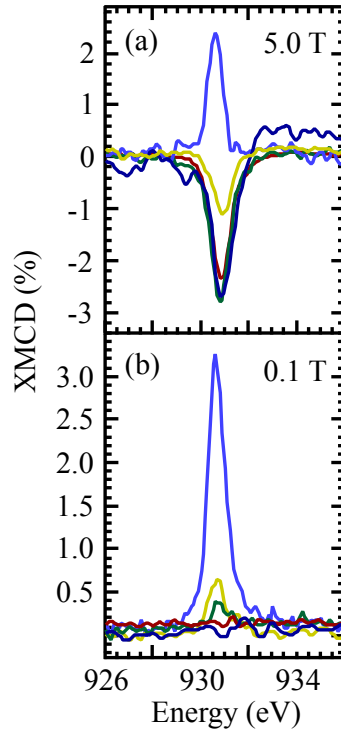
Figure 4.7: **Spin reconstructions on interfacial Cu.** Data sets were taken in TEY mode. The shallow probing depth of TEY enhances interfacial sensitivity, when signals are acquired through a thick capping layer. **(a)** Cu L_3 edge XMCD measurements taken at 15 K and 5.0 Tesla. **(b)** Cu L_3 edge XMCD measurements taken at 15 K and 0.1 Tesla.

coupling, in accordance with superexchange, between adjacent Mn and Cu ions was shown as well, and the magnitude of Cu spin reconstructions scaled with the Mn XMCD signal [104]. The low field data reflects the coupling between Cu and Mn spins, where the Cu signal is proportional to magnitude of the Mn dichroism. The high field data contains a second contribution from inner Cu layers, whose spins cant in the direction of the field due to the aforementioned DM interaction. Except for the $N = 30$ sample, the asymmetric exchange interaction eclipses the signal from the interfacial Cu reconstructions in the 5.0 Tesla field. Furthermore, the increasing thickness of the capping layer has a dynamical effect on the constitution of the TEY signal. TEY has a shallow probing depth and thereby becomes interface sensitive with large N.

The orbital reconstruction cannot be observed from the data presented. XLD measurements

were made and demonstrated the expected orbital reconstruction (not shown). However, the evolution in the XLD signal with N is still the subject of continuing research that has yet to be carried through to fruition.

4.3 Conclusion

The modification of YBCO's electronic structure by interfacial charge transfer from LCMO was explored through a combination of DC transport and x-ray spectroscopy experiments. A definitive perspective of the reconstructed electronic states are obtained from the ultrathin SLs, where spurious signals from u.c. deeper in the layer, found in thicker SLs, do not contribute. The depleted carriers were confirmed to directly enter the CuO_2 planes leading to an imbalance in the standard carrier arrangement found in a typical YBCO u.c. However, the carrier concentration within the planes and the superconducting transition temperatures from the SLs still followed the conventional $YBa_2Cu_3O_{7-\delta}$ phase diagram. These findings reinforce the popular conception that the electronic structure of the conducting planes is the central factor in high-T_c superconductivity. Furthermore, the loss of both superconductivity and ferromagnetism at the interface in YBCO/LCMO stemmed from charge transfer. Competition between the singlet structure of cooper pairs and parallel spin alignment within a ferromagnet was not found to be directly relevant.

While ultrathin SLs provide a framework to map out emergent phases, a breakdown in the charge transfer process interrupted this experiment short of achieving electron-doped superconductivity in YBCO. A systematic decrease in the Mn valence after $N = 3$ is observed by XAS. The rise in Mn $3d$ count coincides with previous limits placed on the area of electronic alteration which suggest that the discrepancy between the chemical potentials of YBCO and LCMO at the interface was negated with charge transfer near $N = 3$. The exact charge profile in the manganite layers of thicker SLs (e.g., $N = 15, 20, 30$) could not be obtained from the inherently spatially averaged data

set and remains an open area of research.

As the Mn valence decreased, magnetic correlations emerged within the heterostructures. With a combination of Mn^{3+} and Mn^{4+} ions present, double exchange between the different Mn species yielded a ferromagnetic ground state in the LCMO layers. In turn, coupling between adjacent Mn and Cu ions near the interface triggered reconstructions in the Cu spins. As previously reported, the magnitude of spin reconstructions scaled with the magnetic signal from Mn and the coupling was antiferromagnetic. A second contribution to the Cu XMCD signal was found that masks detection of the reconstructed spins in large magnetic fields. The extra signal originated from asymmetric exchange between Cu atoms, which were not directly adjacent to the interface. Also, the magnetization within LCMO was found to be strongly field dependent, which is consistent with phase-separated phenomena. The impact of phase separation in LCMO on interfacial Cu ions is unknown and requires further investigation.

Chapter 5

Interface Driven Modifications in Cuprate-Titanate Heterostructures

In this chapter, we explore the interfacial structure and electronic properties of $YBa_2Cu_3O_7/SrTiO_3$ superlattices. The initial research into cuprate heterostructures focused on garnering a greater understanding of the paring mechanism behind high T_c superconductivity. Central to this work was the degree of coupling between planes and dimensionality. Therefore, we begin with a brief review of the proposed models, which underly the mechanism of high T_c, and then proceed to review the literature over past heterostructure research. Current research interests have shifted to the role of the interface in affecting both the overall structure of the unit cell and electronic properties of the crucial CuO_2 planes. In this context, our research into $YBa_2Cu_3O_7/SrTiO_3$ superlattices uncovers dramatic changes within the electronic structure that stem from the unique atomic configuration at the interface.

5.1 Introduction

The essence of high-temperature superconductivity (HTSC) in the hole-doped cuprates arises from the properties of the copper oxide (CuO_2) plane, which is the unifying structural element across the diverse cuprate families. Band structure calculations have shown that the $pd\sigma$-band, consisting of $d(x^2\text{-}y^2)$ states of Cu^{2+} and $p_\sigma(x, y)$ states of O^{2-}, is the primary contribution to the density of states near the Fermi surface [154, 72], and most leading HTSC theories only consider the t-J Hamiltonian describing the CuO_2 plane [155]. Furthermore, experiments on quasi 2D copper oxides have confirmed these states to be the lowest energy excitations [71]. Reflecting this univer-

sality, the cuprates follow an empirical rule for the superconducting transition temperature, T_c, as a function of the hole doping, ρ, within the CuO_2 plane.

$$T_c/T_{c,max} = 1 - 82.6(p - .16)^2 \qquad (5.1)$$

However, equation 1.1 also reveals an underlying flaw in the above paradigm. Naively assuming the CuO_2 planes throughout the cuprates are electronically isomorphic, there exists irreconcilable variations in the material dependent $T_{c,max}$ (i.e. the T_c at optimal doping). This disparate behavior presents in two notable ways. Given a fixed number of CuO_2 layers, n, the optimal T_c depends strongly on the material's family. For instance, $T_{c,max}$ is roughly 40 K in the $La_{2-x}Sr_xCuO_4$ series, while single-layer $HgBa_2CuO_4$ reaches $\sim$94 K. Second, $T_{c,max}$ correlates with an increase in n within a homologous series. Clearly, the ideal array of independent 2D planes is erroneous.

Instead, more realistic models incorporate elements perpendicular to the planes as well, however the work in this area diverges substantially. The earliest models conjectured that the entire pairing mechanism stemmed from interlayer tunneling between weakly coupled planes [42]. However, $T_{c,max}$ decreases or oscillates within a family after $n \simeq 4$, and interlayer Josephson coupling in single-layer cuprates is too weak to account for the pair condensation energy [156]. Current interlayer theories argue that tunneling merely enhances pairing and is not the sole mechanism [157], which is supported by the n dependency of the Josephson plasmon mode in mercurial cuprates [158]. The mainstream view is that the electronic structure of the CuO_2 plane differs in each material. Specifically, the level of disorder within the planes could vary. Another approach relates the copper-apical bond distance to alterations in T_c, which in turn alters the structure of the Fermi surface [159, 160, 161]. Other strategies attempt to incorporate the charge reservoir layers (CRLs) as a means of influencing the pairing mechanism [147].

Engineered heterostructures offer a unique opportunity to address the open hypotheses from above. Previous work focused on YBa$_2$Cu$_3$O$_7$/PrBa$_2$Cu$_3$O$_7$ (YBCO/PBCO) multilayers, where T_c is suppressed as the thickness of the YBCO layers decreases or the thickness of the PBCO layers increases [162]. For all YBCO layer thicknesses, down to 1 unit cell (u.c.), T_c saturates above a non-zero value. To explain the observed behavior, an assortment of models were advanced. For example, the two-dimensionality inherently present in YBCO and the multilayers led many researcher to focus on explanations in terms of a Kosterlitz-Thouless (KT) transition [163, 164, 165]. According to the Mermin-Wagner Theorem, continuous symmetries cannot be broken at finite temperatures in systems with short range forces and limited to one or two dimensions. However, quasi long range ordering of topological excitations, vortex-antivortex pairs, can occur below a finite temperature, T_{KT}. Above T_{KT}, the disassociation of bound vortex-antivortex pairs leads to a phase slip, which causes a finite voltage drop across the sample. Others appealed to a breakdown in the aforementioned interlayer tunneling, where weaker coupling between planes in the heterostructures suppresses T_c [166, 167]. However, each of these scenarios treat the heterostructures as ideal YBCO layers embedded in an innocuous PBCO matrix, which simply creates a semiconducting barrier. Instead, several studies have considered the interaction between the YBCO layers and PBCO layers at the interface. The incorporation of Pr is detrimental to transition temperatures within the LnBa$_2$Cu$_3$O$_{7-\sigma}$ family, and interlayer charge transfer and hole filling may suppress T_c in YBCO/PBCO multilayers [168, 169]. Furthermore, the incorporation of misfit strain causes structural changes with negative impacts on superconductivity e.g. disorder, changes in bond lengths, and doping deficiencies [170, 171].

In this work, we investigate T_c suppression in ultrathin YBa$_2$Cu$_3$O$_7$/SrTiO$_3$ (YBCO/STO) superlattices (SLs). Two series of samples were synthesized: [YBCO$_m$/STO$_1$] with m = 1, 2, 4 u.c. and [YBCO$_2$/STO$_n$] with n = 1, 2, 3, 4 u.c. These series will be referred to as the m-series and

n-series in the following discussions. Recent, transmission electron microscopy (TEM) studies on YBCO/STO SLs attributed the loss of superconductivity to missing chains at the interface and disorder within the CuO_2 planes [173]. While the loss of CRLs and disorder qualitatively explains T_c suppression with decreasing YBCO thickness, those studies were incapable of addressing the ramifications of structural modifications on the local electronic structure. Furthermore, the behavior with increasing STO thickness is not accounted for within this framework. Our analysis will resolve these open questions and place the dialogue on a quantitative footing. A combination of Hall angle and x-ray linear dichroism (XLD) measurements successfully establish and track the degree of disorder and modulations in the carrier concentration both within the CuO_2 planes and the CRLs (chains). For the m-series, a systematic reduction in doping throughout the unit cell and an increase in disorder are observed; these alterations in the electronic structure are connected to the unique configuration of the interface. While a wholly different mode of T_c suppression occurs for the n-series. In this case, the doping within the CuO_2 planes (as measured by XAS) and level of disorder remain constant. However, the Hall angle measurements suggest a decrease in carrier concentration which must be unrelated to doping within the CuO_2 planes. This paradox is resolved by examining the electronic properties of the CRLs. The chapter concludes with an investigation of the previously theoretical proposition of pre-doping at the YBCO/STO interface.

5.2   Results and Disucssion

5.2.1   Structure

The properties of ultrathin SLs are inherently linked to the structure of the interface. Specifically, the termination at the interface can lead to profound changes in doping. The YBCO u.c. is composed of both infinite layers (ILs) i.e. CuO_2 planes and CRLs (Cu-O chains) (see Fig. 1.1(a)). As
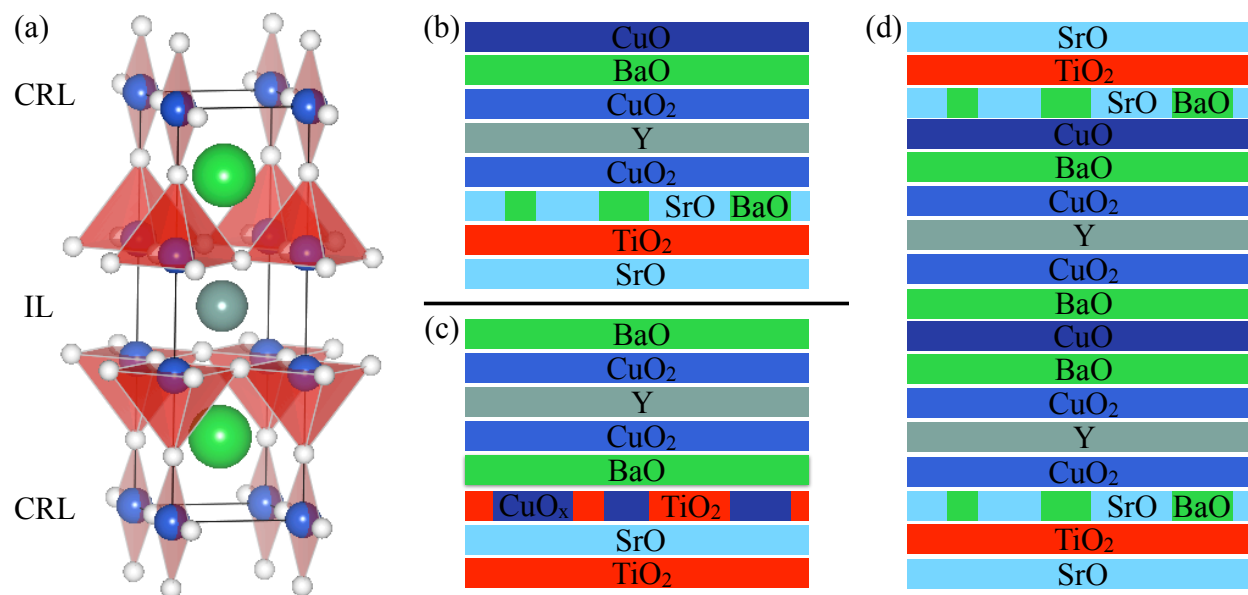
Figure 5.1: **Block schematics of possible YBCO/STO stacking configurations. (a)** YBa$_2$Cu$_3$O$_7$ unit cell with annotations differentiating ILs and CRLs. **(b)** TiO$_2$—BaO interface with SrO and BaO intermixing. **(c)** SrO—CuO interface with TiO$_2$ and CuO intermixing. **(d)** 2 u.c. of YBCO in a YBCO/STO superlattice for the case of asymmetric interfaces.

described in the previous chapters, oxygen doping of the CRLs supplies the charge carriers that dope the ILs and induce superconductivity. When approaching the unit cell limit, missing CRLs at the interface are expected to have dramatic effects on T_c.

Based on the principles of chemical matching, A and B perovskite type alterations across the interface are expected. This leads to six possible stacking configurations and four unique interfaces: SrO—CuO, SrO—CuO$_2$, TiO$_2$—BaO, and TiO$_2$—Y. However, previously published results only support two possible configurations (see Figures 1.1(b, c)) [172, 173]. All studies have concluded that the TiO$_2$—BaO interface is either the only one present or simply the most probable with a minority of SrO—CuO patches. In Figures 1.1(b, c), the interfaces are presented with mixed terminations, which reflects the underlying qualities of the substrate and the realities of film growth. SrO and BaO mix readily at the interface, since both ions share a 2^+ charge state and similar oxygen coordination, while CuO$_x$ and TiO$_2$ mixing requires variations in oxygen content to preserve

the proper Cu charge state. Given a majority of TiO$_2$—BaO interfaces, the chains can be presen-t/missing as shown in the top/bottom interface of Figure 1.1(d). The presence of chains necessitates an extra BaO layer in this case.

Structural analysis of the SLs through high-angle x-ray diffraction and reciprocal space mapping was carried out at beamline 33-BM-C of Argonne National Labs (see Figure 1.2). Specular x-ray reflectivity along the (00L) crystal truncation rod combined with a series of simulations picked out a unique interfacial stacking and allowed for the determination of c-axis structural parameters. In Figure 1.2(a), the experimental specular diffraction pattern of the $n = 1$ sample is graphed along with three simulations, which are displaced vertically for clarity. The experimental pattern displays the expected Bragg peaks (labeled) for a c-axis oriented film. Also, reflections stemming from the super-period appear between the Bragg peaks. The simulated patterns were produced using the reflectivity fitting program GenX [141]. The GenX software allows users to create atomic models to fit reflectivity spectrums. Three distinct atomic models were built and tested: symmetric with chains missing at the top and bottom interfaces (S0C), asymmetric with chains missing at one interface (A1C), and symmetric with chains present at the top and bottom interfaces (S2C). Only the S2C simulation was able to reproduce the experimental pattern. Differences between the simulation and experimental pattern are due to interfacial roughness and modulations in the super-period, which were not accounted for within the S0C model (shown schematically as an inset to Figure 1.2(a)). A magnified view around the STO (003) rod is shown in Figure 1.2(b). The YBCO (009) peak and two superlattice reflections are visible as well. Keissig fringes are present within the pattern. Based on the fringes and location of superlattice reflections, there are exactly 20 repeats in the SL with a period $\Lambda = 22.7801$ Angstroms. The location of the YBCO (009) rod gives a c-axis parameter $c = 11.6552$ Angstroms. In the bulk, the c-axis parameter of YBCO evolves as a function of doping and correlates closely with T_c [174]. The value of c obtained for the SL is slightly
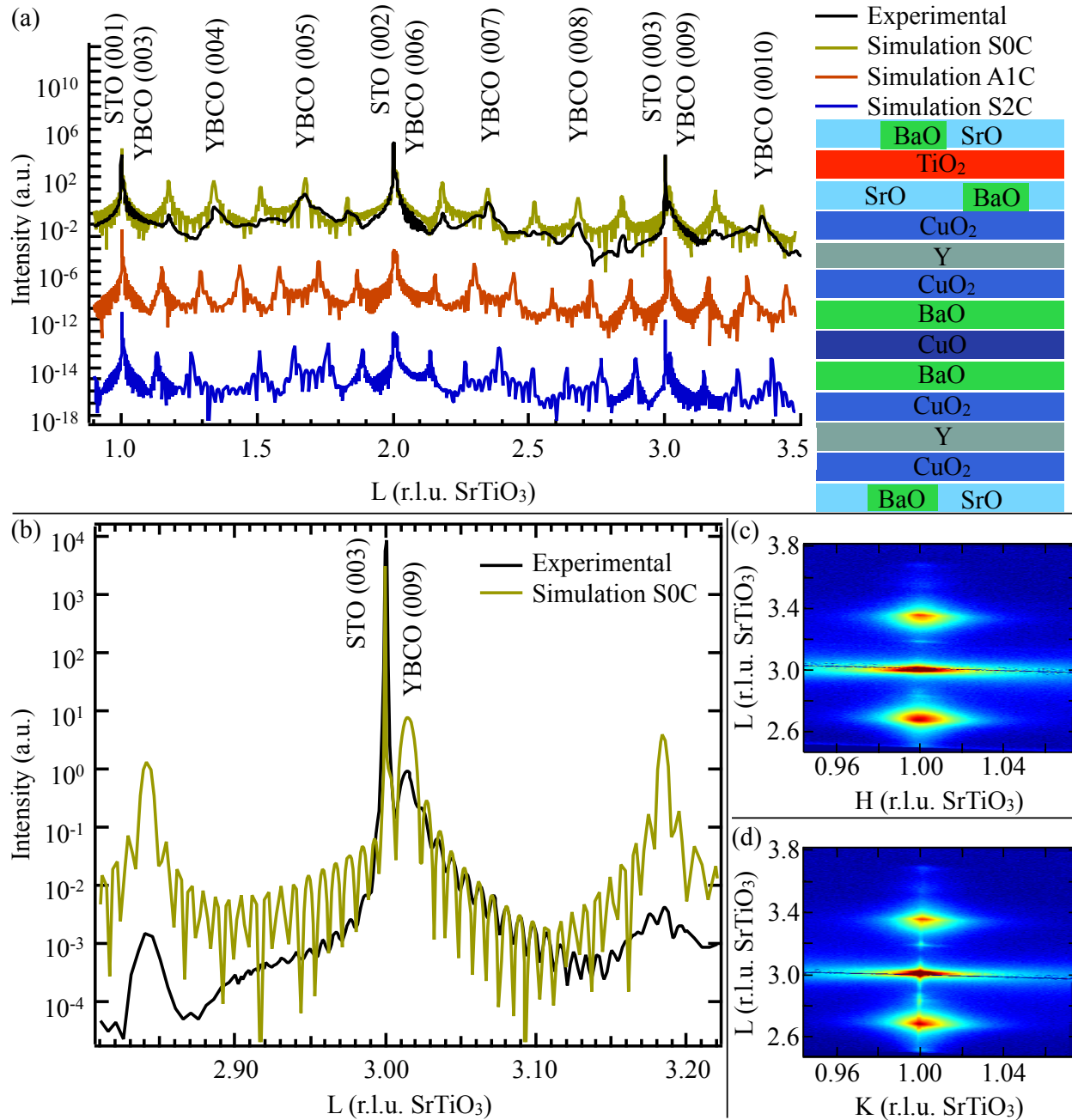
Figure 5.2: **Structural analysis of the [YBCO (2 u.c.)/STO (1 u.c.)]x20 SL. (a)** Specular x-ray reflectivity along the (00L) crystal truncation rod (black curve). Simulations of the reflectivity data for symmetric interfaces with chains missing at top and bottom interfaces (S0C), asymmetric interfaces with chains missing at one interface (A1C), symmetric with chains present at top and bottom interfaces (S2C). Simulations displaced vertically for clarity. Inset: Block schematic of S2C model. **(b)** Specular x-ray reflectivity around the STO (003) and simulation SNC. **(c)** Reciprocal space map around STO (103) **(d)** Reciprocal space map around STO (013).

smaller than expected in over-doped samples, however the role of epitaxial strain still needs to be considered.

In heteroexpitaxy, the growing film locks into atomic registry with the substrate, which generates epitaxial strain. The degree of strain depends upon the mismatch between in-plane lattice parameters. STO has a cubic lattice with $c = 3.9045$ Angstroms, while YBCO has an orthorhombic lattice with in-plane parameters $a = 3.8227$ and $b = 3.8872$ Angstroms. Epitaxy will result in the YBCO lattice undergoing tensile strain. In Figures 1.2(c, d), reciprocal space maps around the STO (103) and (013) rods, respectively, show that the $n = 1$ SL is coherently strained. In both figures, the YBCO (108)/(018), (109)/(019), and (1010)/(0110) rods are in line with their respective substrate peaks. The (109) and (019) rods overlap with the substrate reflections. Furthermore, the reduced YBCO c-axis parameter may be the result of accommodating epitaxial strain. Typically, a unit cell undergoing in-plane tensile strain will be compressed out of plane to conserve constant volume.

5.2.2 Electronic Transport

The temperature dependence of the resistivity is presented in Figures 1.3(a, b) for the two series of YBCO/STO SLs. The sheet resistance, R_S, was measured in van der Pauw geometry, and a parallel resistor model was used to calculate the in-plane resistivity, ρ_{ab}, according to equation 1.2,

$$\rho_{ab} = R_S \times t_{YBCO}. \tag{5.2}$$

STO is an oxide semiconductor with a band gap of 3.2 eV; the resistivity of the STO layers within the SLs exceed the YBCO layers by several orders of magnitude. The current is shunted to the YBCO layers, and the resistivity remains a function of the combined thickness, t_{YBCO}, of all YBCO

layers in the SL. Here, we have assumed identical resistors in parallel. In fact, the large resistance of thick STO layers caused significant problems during sample characterization e.g. charging effects. Therefore, we limit the focus to samples with *n* not exceeding 4 u.c., where all samples could be fully characterized.

In both series, T_c varies with *m* or *n*. For the m-series, a superconductor to insulator transition occurs, when the YBCO layer thickness decreases to 1 u.c (see Figure 1.3(a)). However, the m = 1 sample displays metallic behavior down to 107 K before upturning. This observation runs contrary to the model of missing chains at the interface. For 1 u.c. of YBCO, the lack of chains at both top and bottom interfaces should result in an antiferromagnetic insulator. This leads to two possibilities. The prevalence of SrO—CuO patches is high enough to slightly dope the CuO_2
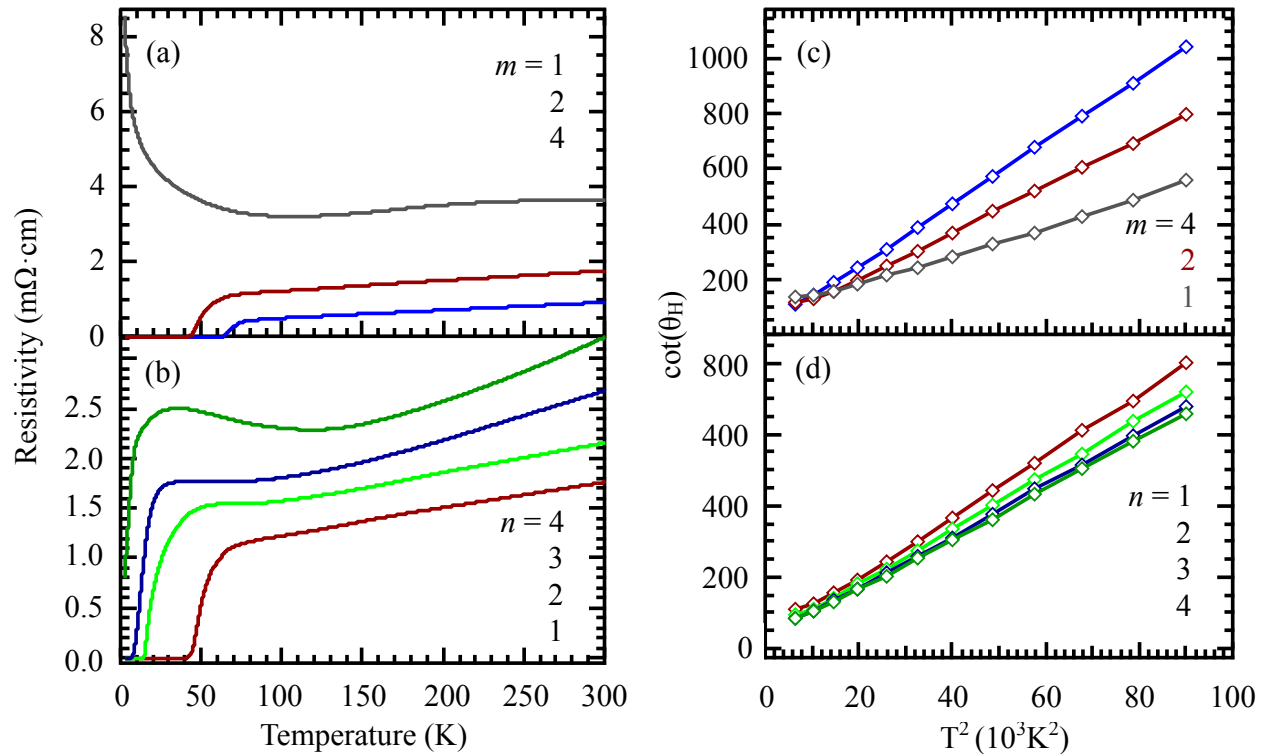

Figure 5.3: **DC transport and Hall angle measurements.** **(a)** Electronic transport from 2-300 K for m-series data. **(b)** Electronic transport from 2-300 K for n-series. **(c)** Hall angle from 2-300 K plotted against T^2 for the m-series. **(d)** Hall angle from 2-300 K plotted against T^2 for the n-series.

planes. Second, the incomplete copper oxide unit cell requires an interface-induced pre-doping, where hole carriers distribute across the CuO_2, TiO_2, and SrO planes to resolve a polar discontinuity [175]. The issue of interface pre-doping will be addressed further in the spectroscopy section. For now, we will continue to examine the trend of diminishing superconductivity with decreasing YBCO thickness and increasing STO thickness. As seen in Figure 1.3(b), T_c is suppressed within the n-series as the STO thickness increases. Above n = 4 (not shown), superconducting transitions are not observed, and the SLs become increasingly insulating with *n*.

To elucidate the origin of T_c suppression within the series, we have performed Hall transport measurements (see Figures 1.3(c, d)). For all samples, a strong T^2 dependence prevails in the normal state transport data except at the lowest temperatures (80 - 100 K), where the data flattens out. The divergence from linearity at low temperatures is a widespread feature of the cuprates and grows stronger with decreasing transition temperatures.

Both the m- and n-series' Hall data contain trends that clarify the role of disorder and carrier doping. Before discussing these issues, we will elaborate on the type of information, which can be extracted, and the current interpretation of the unusual T^2 dependence of the Hall angle. While the anomalous temperature dependence of the normal state transport properties of high-T_c superconductors continues to perplex the community i.e. the linear T-dependence of both the in-plane resistivity and Hall number and their deviation from linearity upon doping, substitution, etc.[176], a phenomenological model has been developed based on the universal T^2-dependence of the Hall angle.

$$cot(\theta_H) = \frac{\rho_{ab}}{R_H B} = \alpha T^2 + C \tag{5.3}$$

Equation 1.3 provides a quantitative measure of two distinct mechanisms of T_c suppression: (1) a *reduction in carrier density* as measured by the slope, α and (2) a *reduction in carrier mobility* as

measured by the intercept, C. These assignments are best explained in terms of the test systems, which formed the basis for their development. In the $YBa_2Cu_3O_{7-\delta}$ series, C remains constant and α varies [177]. The results of altering δ are twofold: it controls both the carrier concentration and the exchange interaction, J. While for Cu-site doped $YBa_2Cu_{3-x}A_xO_7$, C increases systematically with doping and α remains constant [66]. The degradation of superconductivity in the Cu-site doped system is brought about by increased impurity scattering, which hinders carrier mobility and is pair breaking. It is worth noting that in $Pr_xY_{1-x}Ba_2Cu_3O_7$ both α and C vary with Pr doping [178]. The variation in C with Pr doping implies that the increased disorder couples to the electronic states in the CuO_2 planes. Furthermore, the change in α helped confirmed the concept of hole filling within the series.

As mentioned earlier, the normal state properties of high T_c continue to be the subject of on-going research, however it is instructive to consider the possible theoretical models. Theoretical endeavors into this field have taken two main courses. Either the conventional Fermi liquid theory is abandoned, or the typical Fermi scattering rates are significantly modified to reproduce the correct temperature dependence. Here we present two of the leading models, one from each approach.

Anderson was the first to successfully capture the T^2-dependence within a theoretical framework [35]. For the normal state, the Luttinger-liquid model predicts the existence of two distinct quasiparticle excitations, holons and spinons, that naturally leads to two separate relaxation times in the electronic transport. The longitudinal conductivity σ_{xx} is proportional to the transport scattering time $\tau_{tr} \sim 1/T$, whereas the Hall conductivity σ_{xy} is proportional to the multiple of the transport scattering time and the transverse (Hall) scattering time $\tau_H \sim 1/T^2$.

$$cot(\theta_H) = \frac{1}{\omega_c \tau_H} = \frac{1}{\omega_c}\left(\frac{T^2}{W_s} + \frac{1}{\tau_{imp}}\right) \tag{5.4}$$

The Hall angle (see equation 1.4) is now a function of the spinon bandwidth $W_s \sim J$ and an additive impurity term $1/\tau_{imp}$ according to Matthiessen's rule. C from the phenomenological model can be related to the impurity scattering rate, while $\alpha B = k_B^2 \phi_0 n / W_s^2$ with n the two dimensional carrier density, ϕ_0 the flux quantum, and k_B the Boltzmann constant.

Despite the successes of the Luttinger-liquid model, a clear consensus has not been reached. Other models have attempted to explain the T^2-dependence within the conventional Fermi-liquid theory. The cold-spot model of Ioffe and Millis starts from the ansatz in equation 1.5 with τ_{FL} the Fermi-liquid scattering time and T_0 an adjustable parameter,

$$\Gamma(\theta, T) = \Gamma_0 \theta^2 + \frac{1}{\tau_{FL}} = \Gamma_0 \theta^2 + \frac{T^2}{T_0} + \frac{1}{\tau_{imp}} \tag{5.5}$$
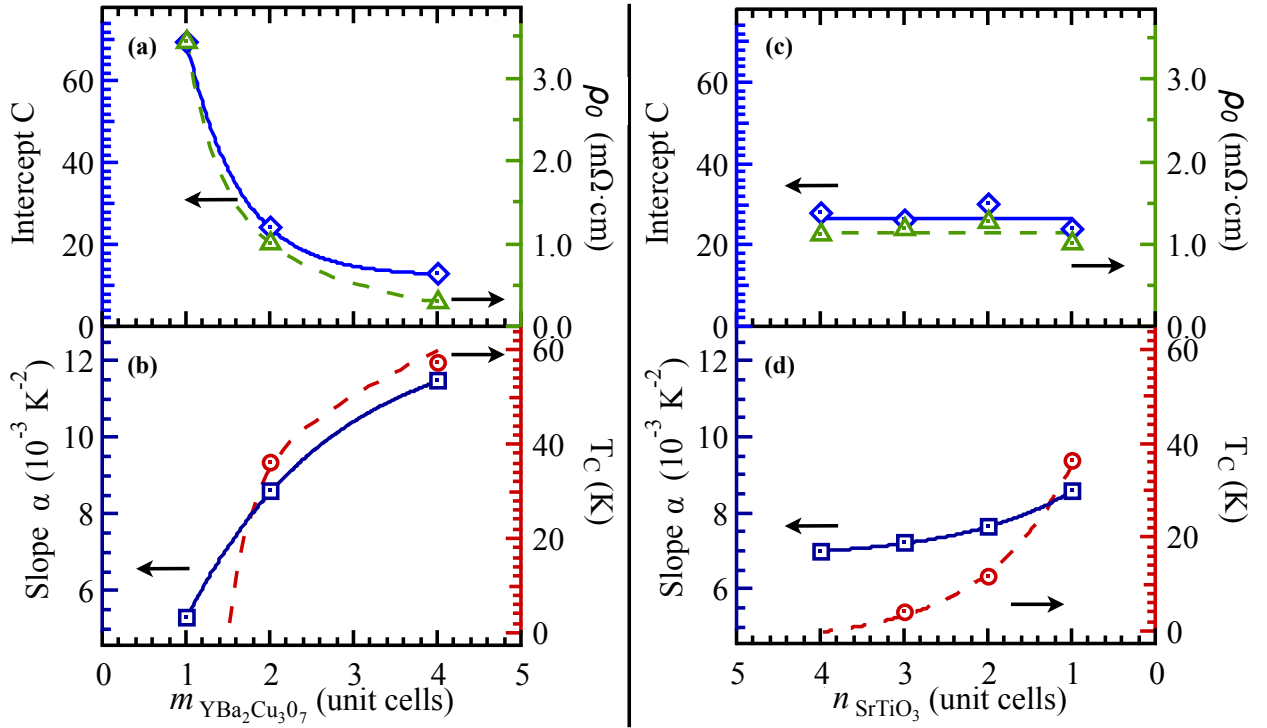
Figure 5.4: **Application of phenomenological model to Hall angle data.** Hall angle analysis for the m-series: **(a)** Left - Intercept C (diamonds). Right - Residual resistivity ρ_0 (triangles). **(b)** Left - Slope α (squares). Right - T_c (circles). Hall angle analysis for the n-series: **(c)** Left - Intercept C (diamonds). Right - Residual resistivity ρ_0 (triangles). **(d)** Left - Slope α (squares). Right - T_c (circles).

where Γ the scattering rate is assumed to have a strong angular dependence [179]. This unusual angular dependence stems from small regions near the Brillouin zone diagonal with significantly longer lifetimes than elsewhere on the Fermi surface. Numerical calculations show that the cold-spot model successfully fits experimental Hall angle data for different doping levels [180]. However, the cold-spot model strongly violates Matthiessen's rule, when impurity scattering is introduced.

Now we return to the Hall angle data for the YBCO/STO SLs, where in Figure 1.4 the phenomenological model has been applied. For the m-series (see Figures 1.4(a, b)), both α and C are evolving as a function of the YBCO layer thickness. The strong correlation between the simultaneous rise in C and the residual resistivity ρ_0 with decreasing m indicates that increased scattering contributes to the suppression of T_c, while the reduction in α signifies a decline in carrier concentration. Given the loss of chains at the interface, the decrease in carrier concentration is expected. The consequences of the missing CRLs should rapidly increase as the number of complete YBCO layers dwindles. Upon approaching the 1 u.c. limit, no chain segments should be present, and the layer is in fact only a partial YBCO unit cell (mainly CuO_2 planes). Therefore, the CuO_2 planes within these ultrathin YBCO/STO SLs are under-doped as demonstrated by the transport data. Furthermore, the increased scattering can naturally be attributed to both: the incomplete YBCO unit cell and the rise in interfacial scattering.

In the n-series' Hall angle data (see Figures 1.4(c, d)), a different set of trends emerge from the application of the phenomenological model. C and ρ_0 fluctuate but remain flat as a function of n. Hence, disorder is an unlikely candidate for T_c suppression within the series. A shallow downswing in α is present, however the absolute change with n is smaller than seen in the m-series. Furthermore, a connection between an increase in STO layer thickness and a decrease in carrier concentration has not been presented.
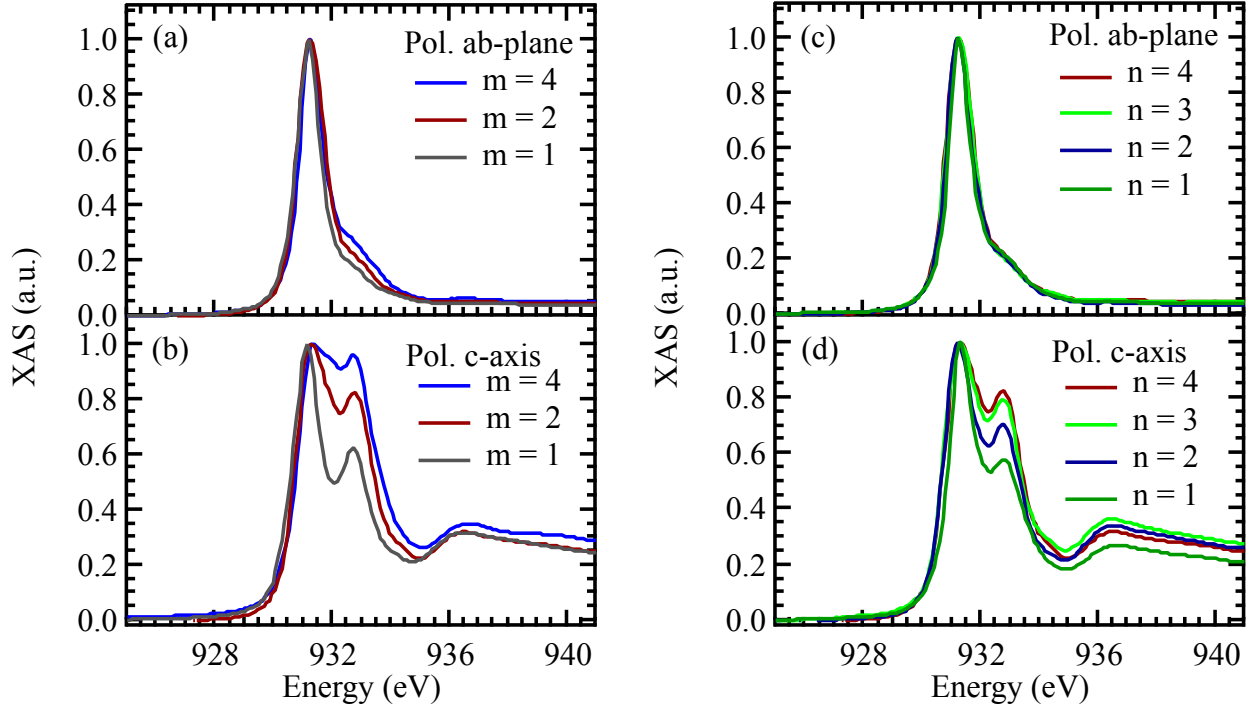
Figure 5.5: **X-ray Linear Dichroism at the Cu L$_3$-Edge normalized to spectrum max.** Spectra were aligned by simultaneously measuring a reference sample in the diagnostic section of the beamline. m-series data: **(a)** Polarization in ab-plane. **(b)** Polarization along c-axis (70° out of plane). n-series data: **(c)** Polarization in ab-plane. **(d)** Polarization in c-axis (70° out of plane).

5.2.3 X-ray Absorption Spectroscopy

A deeper understanding of the electronic structure is required to confirm the assessment of T_c suppression within the m-series and properly interpret the Hall data in the n-series. To this end, linear polarized x-ray absorption spectroscopy (XAS) at the Cu L edge was used to measure the evolution in hole content throughout the YBCO u.c (see Figure 1.5). The Cu atoms within the planes are decorated by ligands in a square pyramidal geometry. This non-isotropic environment leads to a splitting in the e$_g$ states, where the hole preferentially occupies the $d_{x^2-y^2}$ orbital. In accordance, a strong dichroism is observed, however the spectra in figure 1.5 are normalized to peak max for clarity. Linear polarized light allows for the differentiation between two inequivalent Cu sites. Whe the electric field vector (**E**) is parallel to the ab-plane, the in plane absorption signal

(I_{ab}) picks out states of $3d_{x^2-y^2}$ orbital character from Cu(2) in the CuO$_2$ planes. While **E** parallel to the c-axis detects (I_c) detects unoccupied states with $3d_{z^2-y^2}$ orbital character from Cu(1) in the CuO chains [143]. The Cu L$_3$-edge in YBCO is made up of several peaks, but here we focus on the two strongest features: the white line (WL) and the Zhang-Rice peak (ZR). For I_{ab}, the WL is assigned to Cu(2) $3d^9$ → Cu(2) $2\underline{p}3d^{10}$ transitions near 931.2 eV with a shoulder on the high-energy side at 932.53 eV designated ZR from Cu(2) $3d^9\underline{L}$ → Cu(2) $2\underline{p}3d^{10}\underline{L}$ transitions, where $\underline{L}$ denotes a hole on neighboring oxygen sites. For I_c, the lower-energy contribution at about 931 eV is associated with mainly Cu(1) $3d^9$ → Cu(1) $2\underline{p}3d^{10}$ transitions. The high energy satellite peak arises due to Cu(1) $3d^9\underline{L}$ → Cu(1) $2\underline{p}3d^{10}\underline{L}$ transitions [44]. In the m-series, the intensity of the ZR (I_{ab}) and the satellite peak (I_c) diminish as m approaches 1, while for the n-series there is no change in the ab-plane polarization with n. However, the satellite peak decreases in intensity, as the STO layer thickness increases.

The peaks associated with the ligand hole are doping dependent features that can be used to track the hole content within the planes and CRLs. As described in the previous chapter, the ligand hole weight n_h provides a measure of the hole doping ρ within the CuO$_2$ plane,

$$n_h = \frac{A_{ZR}}{A_{WL} + A_{ZR}} \tag{5.6}$$

where A_{WL}/A_{ZR} is the area under the WL/ZR peak. In Figure 1.6, the hole doping through the m and n-series is plotted on the bulk YBCO phase diagram. The doping within the m-series (red circles) decreases with T_c and moves through the YBCO phase diagram, however the trend (red arrow) is shifted with respect to the bulk curve. The shift in T_c is expected in accordance with increased disorder within the m-series. For the n-series (blue diamonds), the doping fluctuates around $\rho = 0.095$, as T_c decreases for increasing n. The observation of constant doping contradicts
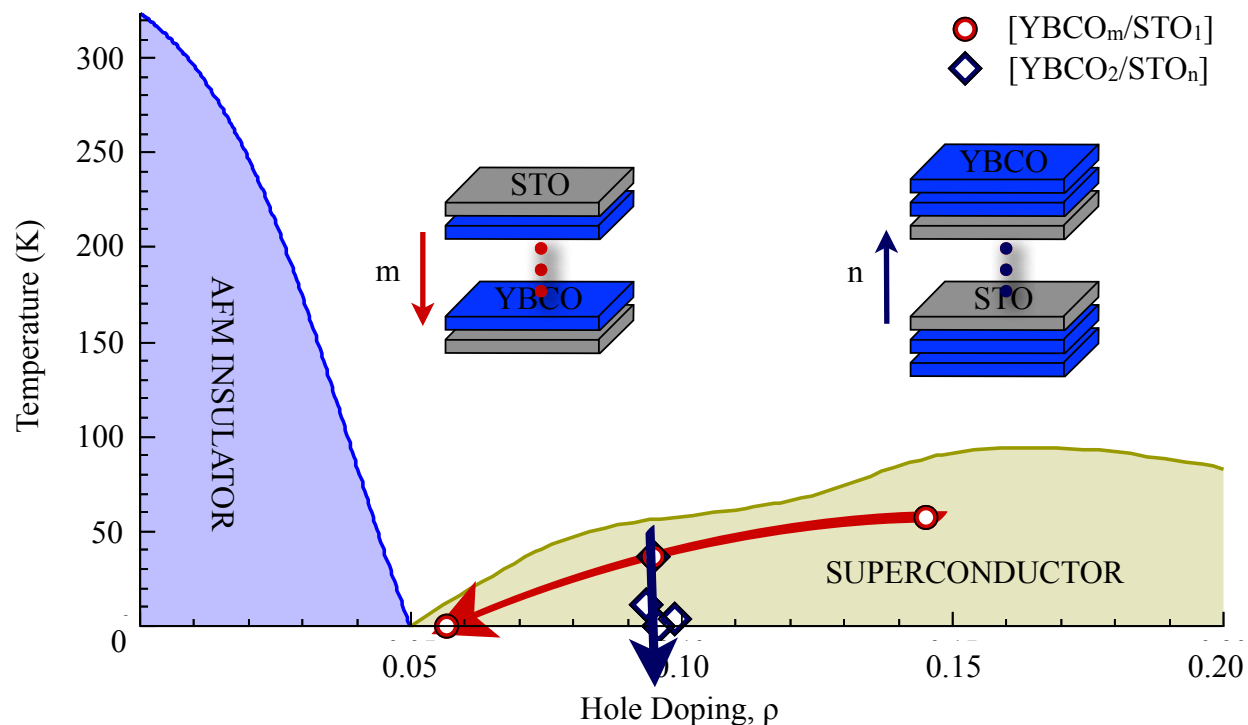
Figure 5.6: **Transition temperature versus CuO$_2$ plane hole doping for the m and n-series plotted on the bulk YBa$_2$Cu$_3$O$_{7-\delta}$ phase diagram**. m-series data (red circles) with trend outlined by red arrow. n-series data (blue diamonds) with trend outlined by blue arrow.

the Hall angle data, where a reduction in the carrier concentration was seen. The discrepancy between the Hall angle and XAS data can be resolved by considering the chain contribution to the Hall conductivity [181]. In the XAS data, the reduction in c-axis ligand weight for the n-series (see Figure 1.5 (d)) signifies a reduction in hole concentration within the CRLs and subsequently decreased chain conductivity. Therefore, the chain contribution to the Hall angle data explains the variation in α.

To address the question of pre-doping at the TiO$_2$—BaO interface, XAS measurements were taken at the Ti L$_{2,3}$ absorption edges for the n-series data (see Figure 1.7 (a)). The spectra were recorded in TEY mode and aligned by the absorption edge energy, E_0. E_0 was determined by taking the derivative of the XAS spectrum. XAS measurements were made for the m-series data at the Ti L edge (not shown) as well and are similar in line shape to the $n = 1$ sample. In SrTiO$_3$,

Ti is in octahedral coordination with a 4+ valence state, and the L edge involves $3d^0 \rightarrow 2\underline{p}3d^1$ transitions. The four main peaks originate from the spin-orbit splitting of the Ti 2p level and the crystal-field splitting of the five degenerate d-orbitals into t_{2g} and e_g states for each spin-orbit component [183]. Reference samples Ti^{3+} (LaTiO$_3$) and Ti^{4+} (SrTiO$_3$) are plotted in Figure 1.7 (b) along with the $n = 1$ sample for comparison. The $n = 1$ sample resembles the SrTiO$_3$ standard, however the spectrum is shifted by 0.6 eV. Shifts of this magnitude are typical in carrier doped samples of SrTiO$_3$ [184]. Furthermore, the t_{2g} peak at the L$_3$ edge is split into two separate peaks separated by 0.6 eV. The smaller peak is not fully resolved and appears as a shoulder on the low energy side. The position of the shoulder matches the t_{2g} maximum of the reference.

The energy shift in the SLs Ti L-edge spectra provides direct evidence for interfacial doping.
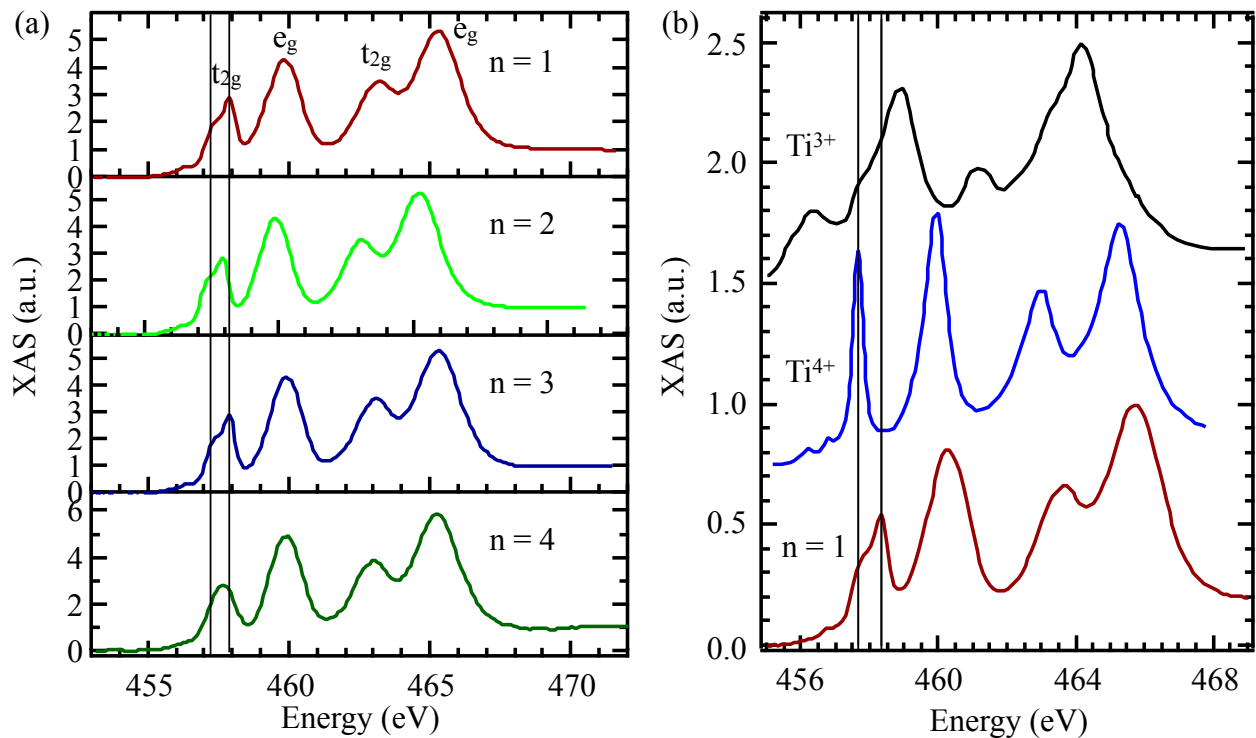
Figure 5.7: **X-ray absorption spectroscopy at the Ti L-Edge with edge jump continuum normalized to unity.** (a) Spectra for the n-series. Black vertical lines indicate energy shift and location of peak centers from fits. (b) Ti^{3+} (LaTiO$_3$) , Ti^{4+} (SrTiO$_3$), and the $n = 1$ SL spectra displaced vertically for clarity. LaTiO$_3$ and SrTiO$_3$ spectra taken from Ref. [81, 182], respectively. Black vertical lines indicate energy shift. The $n = 1$ samples has been normalized for clarity.

In the pre-doping scenario, holes are doped into the interface which maintain charge neutrality [175]. These holes are distributed to the CuO_2 planes and the interfacial SrO and TiO_2 layers. For the $n = 1$ sample, the energy shift of 0.6 eV gives a rough estimate of $0.3e$ per Ti ion, where we have assumed $0.76e$/eV. The low energy shoulder, which coincides with bulk $SrTiO_3$, makes up 35 % of the t_{2g} spectral weight, and the interfacial doping estimate has been reduced accordingly. Furthermore, the electronic reconstruction appears to be confined to the interfacial layers. The XAS signal is cumulative and therefore should evolve with the thickness of the STO layers, if the electronic reconstruction arises from interfacial Ti. In the $n = 4$ sample, the maximum of the t_{2g} peak has shifted closer to the reference, and the splitting is less pronounced.

5.3 Conclusion

Disorder and a reduction in carrier density were shown to be the root of T_c suppression with decreasing YBCO thickness. Calculations based on Hall angle and XLD measurements provide a quantitative measure of disorder and the hole content within the CuO_2 planes. A systematic decreases in carrier concentration is observed on approaching the u.c. limit, where the loss of CRLs at the interface dramatically impacts the charge distribution of the YBCO layers. However, the introduction of disorder is required to completely explain the loss of superconductivity.

For one YBCO u.c., CRLs are expected to be completely absent in the heterostructure. Unexpectedly, the $m = 1$ samples does not display a full reduction in hole doping. Theoretical calculations have suggested that a pre-doping of the interface with holes might be required to resolve a potential polarity mismatch. Ti L-edge spectroscopy lends credence to this scenario. A shift in the t_{2g} peak is observed which is consistent with past reports of doped STO samples. The t_{2g} peaks displays a splitting as well. This spectral feature has not been observed before to the best of our knowledge. The origin of the splitting may be unique to this specific interfacial arrangement or

could stem from a combination of two different Ti sites. The evolution in spectral features with STO thickness indicates that the electronic reconstruction is confined to the interface.

The origin of T_c suppression for increasing STO spacer thickness remains ambiguous. Hall angle data insinuates a relationship between variations in carrier concentration and a loss of superconductivity. However, XAS data reveals that the hole content is constant as a function of n. This discrepancy stems from alterations in chain conductivity that influences the Hall angle data. XAS provides direct evidence for the modification in the local electron structure of the chains. It is unclear why the thickness of the STO layer impacts the hole content within the CRLs. Perhaps, the answer will require a further investigation of the pre-doping scenario. However, a clear link between the modified CRLs and T_c suppression has been established within this study. As stated in the introduction, the diversity in T_c throughout the cuprate families has sparked investigations into the extended structure of the u.c., where the CRLs have been shown to exert control over T_c. Our findings offer further support to this point of view. Another possibility is to consider the role of dimensionality and the breakdown in interlayer coupling, however these arguments remain speculative and require further experimentation for confirmation.

Chapter 6

Summary and Future Prospects

6.1 Conclusion

We began by developing a layer-by-layer growth within a mutually compatible growth regime for $YBa_2Cu_3O_7$ (YBCO) and $La_{2/3}Ca_{1/3}MnO_3$ (LCMO). The selection of deposition conditions (i.e., temperature and ambient O_2 pressure) are constrained by narrow optimal growth windows on the YBCO $P(O_2)$-T phase diagram, despite this interval deposition has been used to stabilize 2D LCMO films with the proper cation stoichiometry. Multilayers grown with interval deposition displayed marked increases in the strength of magnetic dichroic signal and degree of chemical shifts at the Cu L edge signaling an enhancement in the electronic and spin reconstructions at the interface. Sum rules calculation applied to the XMCD spectra for the first time find that the orbital moment is quenched, and the spin component is 0.3079 μ_B/Cu.

We start with establishing a mutually compatible growth regime, in which interval deposition is used to achieve a layer-by-layer growth mode with optimal stoichiometry and sharp interfaces. The multilayers demonstrate a marked enhancement in electronic and spin reconstructions, as compared to previous experimental results. An application of the sum rules shows that the orbital moment is quenched and an uncompensated spin is present on Cu at the interface.

The modification of YBCO's electronic structure through interfacial charge reconstruction was further exploited in ultrathin YBCO/LCMO multilayers. The u.c thick YBCO layers provide an opportunity to view the development of spin and electronic reconstructions without the admixture of bulk-like signals. The depleted carriers were confirmed to directly enter the CuO_2 planes, in

this way the phase diagram of YBCO could be mapped out in a search for emergent phases. However, the charge transfer process breaks down, and the Mn oxidation returns to the formal valence with increasing layer thickness. With a return to formal Mn valency, magnetic correlations emerge within the heterostructure, and coupling between Mn and Cu ions near the interface triggers reconstructions in the Cu spin degree of freedom.

The strong coupling between spin and electronic degrees of freedom in YBCO/LCMO heterostructures at the interface are expected to completely mask all other competing interactions which leaves open the role of weaker players such as reduced dimensionality, broken translational symmetry, interlayer coupling, etc. in the electronic structure of the interface. To this end, $SrTiO_3$ (STO) was inserted as a spacer material in ultrathin YBCO/STO multilayers. Upon approaching the unit cell limit, a decrease in carrier concentration is observed, and found to correlate with missing charge reservoir layers at the interface. The incomplete YBCO unit cells are confirmed to be underdoped, as expected. While disorder plays a smaller role, its introduction is necessary to explain the degree of T_c suppression observed.

6.2 Future Work

With the conclusion of this work, a clearer picture of the reconstructions present at the YBCO/LCMO interface has formed, especially in terms of charge and spin. However, there is still a great deal of work to be done in understanding the evolution in the orbital degree freedom in ultrathin multilayers. A deeper understanding will require further experimental and theoretical investigation. Furthermore compared to the wealth of information available at the interface, very little is known about the electronic and magnetic structure perpendicular to the interface. TEM and scanning probe techniques have been helpful in understanding the charge profile but deliver no insight into the magnetic and orbital profile. While neutron scattering studies are helpful in the former

case, the orbital degree of freedom, once again, remains poorly understood. Currently, we are working on a soft x-ray resonant scattering project which will hopefully shed light onto this problem. However, this task requires a clearer understanding of the interfacial structure which is one of the goals of this dissertation to provide.

In the case of YBCO/STO multilayers, this work may have opened more questions, than it sought and can answer. There is strong evidence for charge transfer between Ti and Cu at the interface, however more research will be required to confirm the pre-doping scenario proposed theoretically. The origin of peak splitting in the Ti L edge spectroscopy is ambiguous. It may be the result of the unique interfacial configuration or a combination of two Ti sites. Another open question is the suppression in critical temperature with STO layer thickness. Hole doping within the plane remains unaffected by the STO layer, however the hole concentration of within the chains is not. It is generally believed that the cation structure, in which the CuO_2 planes are embedded, augment the electronic structure of the superconducting planes. In this sense, the observed suppression in T_c can be understood, however a consensus on the underlying mechanisms involved remains elusive.

References

[1] R. D. Shannon and C. T. Prewitt. *Acta Crystallographica B*, 25:925, 1969.

[2] F. J. Morin. *Bell System Technical Journal*, 37:1047, 19ˇ58.

[3] P. A. Cox. *Transition Metal Oxides*, Oxford: Clarendon Press, 1992.

[4] D. Feng and J. Guojun. *Introduction to Condensed Matter Physics*, Singapore: World Scientific, 2005.

[5] M. Imada, A. Fujimori, and Y. Tokura. *Review of Modern Physics*, 70:1039, 1998.

[6] J. Zaanen, G. A. Sawatzky, and J. W. Allen. *Physical Review Letters*, 55:418, 1985.

[7] R. D. Leapman, L. A. Grunes, and P. Fejes. *Physical Review B,* 26:614, 1982.

[8] F. W. Lytle. *Journal of Applied Physics*, 35:2212, 1964.

[9] Lixin Cao, E. Sozontov, and J. Zegenhagen, *Physica Status Solidi*, 181:387, 2000.

[10] L. F. Mattheiss. *Physical Review B*, 6:4718, 1972.

[11] T. F. Soules, E. J. Kelly, D. M. Vaught, and J. W. Richardson. *Physical Review B*, 6:1519, 1972.

[12] P. Pertosa and F. M. Michel-Calendini. *Physical Review B*, 17:2011, 1972.

[13] J. F. Schooley, W. R. Hosler, and M. L. Cohen. *Physical Review Letters*, 12:474, 1964.

[14] E. R. Pfeiffer and J. F. Schooley. *Physical Review Letters*, 29A:589 1969.

[15] W. Gong, H. Yun, Y. B. Ning, J. E. Greedan, W. R. Datars, and C. V. Stager. *Journal of Solid State Chemistry*, 90:320, 1991.

[16] A. Urushibara, Y. Moritomo, T. Arima, and Y. Tokura. *Physical Review B*, 51:14103, 1995.

[17] J. Mira, J. Rivas, L. E. Hueso, F. Rivadulla, M. A. Lopez Quintela, M. A. Rodriquez, and C. A. Ramos. *Physical Review B*, 65:024418, 2001.

[18] P. G. Radaelli, M. Marezio, H. Y. Hwang, and S-W. Cheong. *Journal of Solid State Chemistry*, 122: 444, 1996.

[19] M. Abbate, F. M. F. de Groot, J. C. Fuggle, A. Fujimori, O. Strebel, F. Lopez, M. Domke, G. Kaindl, G. A. Sawatzky, M. Takano, Y. Takeda, H. Eisaki, S. Uchida. *Physical Review B*, 46:4511, 1992.

[20] A. Chainani, M. Matthew, and D. D. Sarma. *Physical Review B*, 47:15397, 1993.

[21] T. Saitoh, A. E. Bocquet, T. Mizokawa, H. Namatame, A. Fujimori, Y. Abbate, Y. Takeda, and M. Takano. *Physical Review B*, 51:13942, 1995.

[22] S. Satpathy, Z. S. Popović, and F. R. Vukajlović. *Physical Review Letters*, 76:960, 1996.

[23] G. Zampieri, F. Prado, A. Caneiro, J. Briático, M. T. Causa, M. Tovar, B. Alascio, M. Abbate, and E. Morikawa. *Physical Review B*, 58:3758, 1998.

[24] W. E. Pickett and D. J. Singh. *Physical Review B*, 53:1146, 1996.

[25] J. B. Goodenough. *Physical Review*, 100:564, 1955.

[26] J. Kanamori. *Progress in Theoretical Physics*, 30:275, 1963.

[27] E. O. Wollan, and W. C. Koehler. *Physical Review*, 100:545, 1955.

[28] I. Solovyev, N. Hamada, and K. Terakura. *Physical Review Letters*, 76:4825, 1996.

[29] M. Uehara, B. Kim, S.-W. Cheong. *Personal Communciation*, 2000.

[30] M. B. Salamon and M. Jaime. *Review of Modern Physics*, 73:583, 2001.

[31] P. Schiffer, A. P. Ramirez, W. Bao, and S.-W. Cheong. *Physical Review Letters*, 75:3336, 1995.

[32] J. F. Mitchell, D. N. Argyriou, C. D. Potter, D. G. Hinks, J. D. Jorgensen, and S. D. Bader. *Physical Review B*, 54:6172, 1996.

[33] S-W. Cheong and H. Y. Hwang. *Colossal Magnetoresitive Oxides*, Amsterdam: Gordon and Breach, 2000.

[34] C. Zener. *Physical Review*, 82:403, 1951.

[35] P. W. Anderson and H. Hasegawa. *Physical Review B*, 100:675, 1955.

[36] A. J. Millis, P. B. Littlewood, and, B. I. Shraiman. *Physical Review Letters*, 74:5144, 1995.

[37] M. Uehara, S. Mori, C. H. Chen, and S.-W. Cheong. *Letters to Nature*, 399:560, 1999.

[38] J. G. Bednorz and A. Müller. *The Journal of Physical Chemistry B*, 64:189, 1986.

[39] C. N. R. Rao and A. K. Ganguli. *Acta Crystallographica B*, 51:604, 1995.

[40] R. M. Hazen. *Physical Properties of High Temperature Superconductors II*, Singapore: World Scientific, 1990.

[41] S. Chakravarty. *European Physical Journal B*, 5:337, 1998.

[42] P. W. Anderson. *The Theory of Superconductivity in the High-T_c Cuprates*. Princeton: Princeton University Press, 1997, and references therein.

[43] S.-L. Drechsler, J. Málek, and H. Eschrig. *Physical Review B*, 55:606, 1997.

[44] N. Nücker, E. Pellegrin, P. Schweiss, J. Fink, S. L. Molodtsov, C. T. Simmons, G. Kaindl, W. Frentrup, A. Erb and G. Müller-Vogt. *Physical Review B*, 51:8529, 1995.

[45] H. Alloul, T. ohno, and P. Mendels. *Physical Review Letters*, 63:1700, 1989.

[46] C.-J. Mei, and G. Stollhoff. *Physical Review Letters*, 43:3065, 1991.

[47] C. Bernhard, R. Henn, A. Wittlin, M. Kläser, Th. Wolf, G. Müller-Vogt, C. T. Lin, and M. Cardona. *Physical Review Letters*, 80:1762, 1998.

[48] J. M. Trandquada, A. H. Shirane, B. Keimer, S. Shamoto, and M. Sata. *Physical Review B*, 40:4503, 1989.

[49] J. Rossat-Mignod, L. P. Regnault, M. J. Jurgens, C. Vettier, P. Burlet, J. Y. Henry, and G. Laperot. *Physica B*, 163:4, 1990.

[50] S. Shamoto, M. Sato, J. M. Tranquada, B. J. Sternlieb, and G. Shirane. *Physical Review B*, 48:13817, 1993.

[51] J. Rossat-Mignod, L. P. Regnault, P. Bourges, P. Burlet, C. Vettier, and J. Y. Henry. *Selected Topics in Supercondcutivity*, Singapore: World Scientific, 1993.

[52] A. G. Loeser, Z.-X. Shen, D. S. Dessau, D. S. Marshall, C. H. Park, P. Fournier, and A. Kapitulnik. *Science*, 273:325, 1996.

[53] H. Ding, T. Yokoya, J. C. Campuzano, T. Takahashi, M. Randeria, M. R. Norman, T. Mochiku, K. Kadowaki, and J. Giapintzakis. *Nature*, 382:51, 1996.

[54] M. R. Norman, D. Pines, and C. Kallin. *Advances in Physics*, 54:715, 2005.

[55] M. Randeria, Nandi Trivedi, Adriana Moreo, and Richard T. Scalettar. *Physical Review Letters*, 69:2001, 1992.

[56] V. J. Emery and S. A. Kivelson. *Nature*, 374:434, 1995.

[57] S. Chakravarty, R. B. Laughlin, D. K. Morr, and C. Nayak. *Physical Review B*, 63:094503, 2001.

[58] T. Hanaguri, C. Lupien, Y. Kohsaka, D.-H. Lee, M. Azuma, M. Takano, H. Takagi, and J. C. Davis. *Nature*, 430:1001, 2004.

[59] W. D. Wise, M. C. Boyer, K. Chatterjee, T. Kondo, T. Takeuchi, H. Ikuta, Y. Wang, and E. W. Hudson. *Nature Physics*, 4:696, 2008.

[60] H. Kamimura, T. Hamada, and H. Ushio. *Physical Review B*, 66:054504, 2002.

[61] P. Prelovsek and A. Ramsak. *Physical Review B*, 65:174529, 2002.

[62] K. Tanaka, W. S. Lee, D. H. Lu, A. Fujimori, T. Fujii, Risdiana, I. Terasaki, D. J. Scalapino, T. P. Devereaux, Z. Hussain, and Z.-X. Shen. *Science*, 314:1910, 2006.

[63] T. Kondo, T. Takeuchi, A. Kaminski, S. Tsuda, and S. Shin. *Physical Review Letters*, 98:267004, 2007.

[64] K. Terashima, H. Matsui, T. Sato, T. Takahashi, M. Kofu, and K. Hirota. *Physical Review Letters*, 99:017003, 2007.

[65] W. S. Lee, I. M. Vishik, K. Tanaka, D. H. Lu, T. Sasasgawa, N. Nagaosa, T. P. Devereaux, A. Hussain, and Z.-X. Shen. *Nature*, 450:81, 2007.

[66] T. R. Chien, Z. Z. Wang, and N. P. Ong. *Physical Review Letters*, 67:2088, 1991.

[67] A. Kaminski, S. Rosenkranz, H. M. Fretwell, Z. Z. Li, H. Raffy, M. Randeria, M. R. Norman, J. C. Campuzano. *Physical Review Letters*, 90:207003, 2003.

[68] N. E. Hussey. *Journal of Physics: Condensed Matter*, 20:123201, 2008.

[69] D. M. Broun. *Nature Physics*, 4:170, 2008.

[70] J. Fink, N. Nücker, H. A. Romberg, and J. C. Fuggle. *IBM Journal of Research and Development*, 33:372, 1989.

[71] A. Damascelli, Z. Hussain, and Z.-X. Shen. *Review of Modern Physics*, 75:473, 2003.

[72] W. E. Pickett. *Review of Modern Physics*, 61:433, 1989.

[73] S. Uchida, T. Ido, H. Takagi, T. Arima, Y. Tokura, and S. Tajima. *Physical Review B*, 43:7942, 1991.

[74] P. W. Anderson. *Science*, 235:1196, 1987.

[75] V. J. Emery. *Physical Review Letters*, 58:2794, 1987.

[76] F. C. Zhang and T. M. Rice. *Physical Review B*, 37:3759, 1988.

[77] H. Eskes and G. A. Sawatzky. *Physical Review Letters*, 61:1415, 1988.

[78] P. Zubko, S. Gariglio, M. Gabay, P. Ghosez, and J.-M. Triscone. *Annual Review of Condensed Matter Physics*, 2:141, 2011.

[79] A. Ohtomo, D. A. Muller, J.L. Grazul, and H.Y. Hwang. *Nature*, 419:378, 2002.

[80] J. M. Rondinelli, M. Strengel, N. A. Spaldin. *Nature Nanotechnology*, 3:46, 2008.

[81] M. Haverkort. *Spin and orbital degrees of freedom in transition metal oxides and oxide thin films studied by soft x-ray absorption spectroscopy*, Köln: University of Köln, 2005.

[82] F. de Groot. *Coordination Chemistry Reviews*, 249:31, 2005.

[83] J. Stöhr and Y. Wu. *New Direction in Research with Third-Generation Soft X-Ray Synchrotron Radiation Sources*, Netherlands: Kluwer Academic Publishers, 1994.

[84] J. W. Freeland, J. C. Lang, G. Srajer, R. Winarski, D. Shu, and D. M. Millis. *Review of Scientific Instruments*, 73:1408, 2002.

[85] D. B. Chrisey and G. K. Hubler. *Pulsed Laser Deposition*, New York: John Wiley and Sons, 1994.

[86] R. Kelley and A. Miotello. *Applied Physics A*, 69:67 1999.

[87] A. Kareev. *Personal communication*, 2012.

[88] J. Tchakhalian. *Personal communication*, 2012.

[89] T. Michely and J. Krug. *Islands, Mounds and Atoms*, Berlin: Springer-Verlag, 2004.

[90] Z. Zhang and M. Lagally. *Science*, 276:377, 1997.

[91] G. Ehrlich and F. G. Hudda. *Journal of chemical Physics*, 44:1039, 1996.

[92] R. L. Schwoebel. *Journal of Applied Physcis*, 40:614, 1968.

[93] W. Hong, H. N. Lee, M. Yoon, H. M. Christen, D. H. Lowndes, and Z. Zhang. *Physical Review Letters*, 95:095501, 2005.

[94] J. G. Amar, F. Family, and P.-M. Lam. *Physical Review B*, 50:8781, 1994.

[95] J. Klein. *Epitaktische Heterostrukturen aus dotierten Manganaten*, Cologne: University of Cologne, 2001.

[96] Relativistic correction amounting to roughly 1 % have been ignored.

[97] R. H. Hammond and R. Bormann. *Physica C*, 703:162, 1989.

[98] A. I. Buzdin. *Review of Modern Physics*, 77:935, 2005.

[99] Z. Sefrioui, D. Arias, V. Pena, J. E. Villegas, M. Varela, P. Prieto, C. Leon, J. L. Martinez, and J. Santamaria. *Physical Review B*, 67:214511, 2003.

[100] T. Holden, H.-U. Habermeier, G. Cristiani, A. Boris, A. Pimenov, J. Humliček, O.I. Lebedev, G. Van Tendeloo, B. Keimer, and C. Bernhard. *Physical Review B*, 69:064505, 2004.

[101] F. S. Bergeret, A. F. Volkov, and K. B. Efetov. *Physical Review Letters—*, 86:4096, 2001.

[102] F. S. Bergeret, A. F. Volkov, and K. B. Efetov. *Physical Review B*, 69:174504, 2004.

[103] J. Stahn, J. Chakhalian, Ch. Niedermayer, J. Hoppler, T. Gutberlet, J. Voigt, F. Treubel, H-U. Habermeier, G. Cristiani, B. Keimer, and C. Bernhard. *Physical Review B*, 71:140509, 2005.

[104] J. Chakhalian, J. W. Freeland, G. Srajer, J. Strempfer, G. Khaliullin, J. C. Cezar, T. Charlton, R. Dalgliesh, C. Bernhard, G. Cristiani, H.-U. Habermeier, and B. Keimer. *Nature Physics*, 2:244, 2006.

[105] J. Chakhalian, J. W. Freeland, H.-U. Habermeier, G. Cristiani, G. Khaliullin, M. van Veenendaal, and B. Keimer. *Science*, 318:1114, 2007.

[106] J.W. Freeland, J. Chakhalian, H.-U. Habermeier, G. Cristiani, and B. Keimer. *Applied Physics Letters*, 90:242502, 2007.

[107] X. Yang, A. N. Yaresko, V. N. Antonov, and O. K. Anderson. *arXiv*, 0911.439, 2009.

[108] R. Werner, C. Raisch, A. Ruosi, B. A. Davidson, P. Nagel, M. Merz, S. Schuppler, M. Glaser, J. Fujii, T. Chasse, R. Kleiner, and D. Koelle. *Physical Review B*, 82:224509, 2010.

[109] Y. Kalcheim, T. Kirzhner, G. Koren, and O. Millo. *Physical Review B*, 83:064510, 2011.

[110] G. Koster, G. J. H. M. Rijnders, D. H. A. Blank, and H. Ragalla. *Applied Physics Letters*, 74:3729, 1999.

[111] R. Liang, D. A. Bonn, and W. N. Hardy. *Physical Review B*, 73:180505, 2006.

[112] O. I. Lebedev, G. van Tendeloo, and S. Amelinckx. *Physical Review B*, 58:8065, 1998.

[113] J. Aarts, S. Freisem, R. Hendrikx, and H.W. Zandbergen. *Applied Physics Letters*, 72:2975, 1998.

[114] C. T. Chen, F. Sette, Y. Ma, M. S. Hybertsen, E. B. Stechel, W. M. C. Foulkes, M. Schulter, S-W. Cheong, A. S. Cooper, L. W. Rupp, Jr., B. Batlogg, Y. L. Soo, Z. H. Ming, A. Krol, and Y. H. Kao. *Physical Review Letters*, 66:104, 1991.

[115] F.M.F. de Groot. *Journal of Electron Spectroscopy and Related. Phenomena*, 67:529, 1194.

[116] Jian Liu, B. J. Kirby, B. Gray, M. Kareev, H.-U. Habermeier, G. Cristiani, J. W. Freeland, and J. Chakhalian. *Physical Review B*, 84:092506, 2011.

[117] B. T. Thole, P. Carra, F. Sette, and G. vad der Laan. *Physical Review Letters*, 68:1943, 1992.

[118] P. Carra, B. T. Thole, M. Altarelli, and X. Wang. *Physical Review Letters*, 70:694, 1993.

[119] C. T. Chen, Y. U. Idzerda, H.-J. Lin, N. V. Smith, G. Meigs, E. Chaban, G. H. Ho, E. Pellegrin, and F. Sette. *Physical Review Letters*, 75:152, 1995.

[120] Satoshi Okamoto and Andrew J. Millis. *Nature*, 428:630, 2004.

[121] S. Yunoki, A. Moreo, E. Dagotto, S. Okamoto, S. S. Kancharla, and A. Fujimori. *Physical Review B*, 76:064532, 2007.

[122] M. Bibes, J. E. Villegas, and A. Barthélémy. *Advances in Physics*, 60:5, 2011.

[123] A. Ohtomo and H. Y. Hwang. *Nature*, 427:423, 2004.

[124] D. N. Basov, R. D. Averitt, D. van der Marel, M. Dressel, and K. Haule. *Review of Modern Physics*, 83:471, 2001.

[125] E. Dagotto. *Science*, 309:257, 2005

[126] F. S. Bergeret, A. F. Volkov, and K. B. Efetov. *Review of Modern Physics*, 77:1321, 2005.

[127] J. Hoppler. *Nature Materials*, 8:315, 2009.

[128] N. Driza. *Nature Materials*, 11:675, 2012.

[129] V. Pena, Z. Sefrioui, D. Arias, C. Leon, J. Santamaria, M. Varela, S. J. Pennycook, and J. L. Martinez. *Physical Review B*, 69:224502, 2004.

[130] D. K. Satapathy. *Physical Review Letters*, 108:197201, 2012.

[131] A. Hoffman, et al. *Physical Review B*, 72: 140407(R), 2005.

[132] T. Y. Chien, L. F. Kourkoutis, J. Chakhalian, B. Gray, M. Kareev, N. P. Guisinger, D. A. Muller, and J. W. Freeland. *Nature Communications*, 4:2336, 2013.

[133] The expression in equation 1.1 has been simplified. Identical YBCO layers have been assumed, and the square geometry of the substrate and arrangement of the electrical contacts causes dimensional terms to cancel out. Also, the standard geometric correction ($R_S = \frac{\pi R}{ln(2)}$) has been applied.

[134] Y. Iye. *Physical Properties of High-Temperature Superconductors III*, edited by D. M. Ginsberg, pg. 285, (1993).

[135] T. Ito, K. Takena, and S. Uchida. *Physical Review Letters*, 70:3995, 1993.

[136] L. Zhang, C. Israel, A. Biswas, R. L. Greene, and A. de Lozanne. *Science*, 298:805, 2002.

[137] J. C. Loudon, N. D. Mathur, and P. A. Midgley. *Nature*, 420:797, 2002.

[138] Z. L. Zhang, U. Kaiser, S. Soltan, H.-U. Habermeier, and B. Keimer. *Applied Physics Letters*, 95:242505, 2009.

[139] C. Visani, J. Tornos, N. M. Nemes, M. Rocci, C. Leon, J. Santamaria, S. G. E. te Velthuis, Yaohua Liu, A. Hoffman, J. W. Freeland, M. Garcia-Hernandez, M. R. Fitzsimmons, B. J. Kirby, M. Varela, and S. J. Pennycook. *Physical Review B*, 84:060405, 2011.

[140] V. K. Malik, I. Marozau, S. Das, B. Doggett, D. K. Satapathy, M. A. Uribre-Laverde, N. Biskup, M. Varela, C. W. Schneider, C. Marcelot, J. Stahn, and C. Bernhard. *Physical Review B*, 85:054514, 2012.

[141] M. Björck and G. Andersson. *Journal of Applied Crystal Growth*, 40:1174, 2007.

[142] Ruixing Liang, D. A. Bonn, and W. N. Hardy. *Review of Modern Physics*, 77:721, 2005.

[143] Nücker. *Physical Review B*, 39:6619, 1989.

[144] M. Merz, N. Nücker, P. Schweiss, S. Schuppler, C. T. Chen, V. Chakarian, J. Freeland, Y. U. Idzerda, M. Kläser, G. Müller-Vogt, and Th. Wolf. *Physical Review Letters*, 80:5192, 1998.

[145] C. Aruta, G. Ghiringhelli, C. Dallera, F. Fracassi, P. G. Medaglia, A. Tebano, N. B. Brookes, L. Braicovich, and G. Balestrino. *Physical Review B*, 78:205120, 2008.

[146] N. Merrien, F. Studer, G. Poullain, C. Michel, A. M. Flank, P. Lagarde, and A. Fontaine. *Journal of Solid State Chemistry*, 105:112, 1993.

[147] S. Raghu, R. Thomale, and T. H. Geballe. *Physical Review B*, 86: 094506, 2012.

[148] J. Chang. *Nature Physics*, 8:871, 2012.

[149] M. Salluzzo, G. Ghiringhelli, J. C. Cezar, N. B. Brookes, G. M. De Lucca, F. Fracassi, and R. Vaglio. *Physical Review Letters*, 100:056810, 2008.

[150] X. Leng, J. G.-Barriocanal, S. Bose, Y. Lee, and A. M. Goldman. *Physical Review Letters*, 107:027001, 2011.

[151] G. M. De Luca, G. Ghiringelli, M. Moretti Sala, S. Di Matteo, M. W. Haverkort, H. Berger, V. Bisogni, J. C. Cezar, N. B. Brookes, and M. Salluzzo. *Physical Review B*, 82:214504, 2010.

[152] The lack of spatial resolution in XAS leaves the distribution of charge within the thicker LCMO layers uncertain.

[153] M. Grioni, J. B. Goedkoop, R. Schoorl, F. M. F. de Groot, J. C. Fuggle, F. Schäfers, E. E. Koch, G. Rossi, J.-M. Esteva, and R. C. Karnatak. *Physical Review B*, 39:1541, 1989.

[154] L.F. Mattheiss. *Physical Review Letters*, 58:1028, 1987.

[155] N. Plakida. *High-Temperature Cuprate Superconductors*. New York: Springer, 2010.

[156] A. A. Tsvetkov, D. van der Marel, K. A. Moler, J. R. Kirtley, J. L. de Boer, A. Meetsma, Z. F. Ren, N. Koleshnikov, D. Dulic, A. Damascelli, M. Grüninger, J. Schützmann, J. W. van der Eb, H. S. Somal, and J. H. Wang. *Nature (London)*, 395:360, 1998.

[157] S. Chakravarty, H.-Y. Kee, and K. Völker. *Nature (London)*, 428:53, 2004.

[158] Y. Hirata, K. M. Kojima, M. Ishikado, S. Uchida, A. Iyo, H. Eisaki, and S. Tajima. *Physical Review B*, 85:054501, 2012.

[159] E. Pavarini, I. Dasgupta, T. Saha-Dasgupta, O. Jepsen, and O. K. Anderson. *Physical Review Letters*, 87:047003, 2001.

[160] H. Sakakibara, H. Usui, K. Kuroki, R. Arita, and H. Aoki. *Physical Review Letters*, 105:057003, 2010.

[161] K. Kuroki. *Journal of Physics and Chemistry of Solids*, 72:307, 2011.

[162] Q. Li, X. X. Xi, X. D. Wu, A. Inam, S. Vadlamannati, W. L. Mclean, T. Venkatesan, R. Ramesh, D. M. Hwang, J. A. Martinez, L. Nazar. *Physical Review Letters*, 64:3086, 1990.

[163] D. Ariosa and H. Beck. *Physical Review B*, 43:344, 1991.

[164] Y. Matsuda, S. Komiyama, T. Onogi, T. Terashima, K. Shimura, and Y. Bando. *Physical Review B*, 48:498, 1993.

[165] M. Rasolt, Taner Edis, and Zlatko, Tešanović. *Physical Review Letters*, 66:2927, 1991.

[166] W. K. Park and Z. G. Khim. *Physical Review B*, 61:1530, 2000.

[167] A. K. Rajagopal and S. D. Mahanti. *Physical Review B*, 44:210, 1991.

[168] Marta Z. Cieplak, S. Guha, S. Vadlamannati,T. Giebultowicz, and P. Lindefeld. *Physical Review B*, 50:876, 1994.

[169] R. F. Wood. *Physical Review B*, 50:688, 1994.

[170] M. Varela, D. Arias, Z. Sefrioui, C. Leon, C. Ballesteros, and J. Santamaria. *Physical Review B*, 62:509, 2000.

[171] M. Varela, D. Arias, Z. Sefrioui, C. Leon, C. Ballesteros, S. J. Pennycook, and J. Santamaria. *Physical Review B*, 66:134517, 2002.

[172] C. M. Schlepütz, M. Björck, E. Koller, S. A. Pauli, D. Martoccia, Ø. Fischer, P. R. Willmot. *Physical Review B*, 81:174520, 2010.

[173] J. Garcia-Barriocanal, A. M. Perez-Muñoz, Z. Sefrioui, D. Arias, M. Varela, C. Leon, S. J. Pennycook, and J. Santamaria. *Physical Review B*, 87:245105, 2013.

[174] Ruixing Liang, D. A. Bonn, and W. N. Hardy. *Physical Review B*, 73:180505 2006.

[175] N. Pavlenko, I. Elfimov, T. Kopp, and G. A. Sawatzky. *Physical Review B*, 75:140512, 2007.

[176] D. M. Ginsberg. *Physical Properties of High Temperature Superconductors III*.Singapore: World Scientific, 1992.

[177] B. Wuyts, E. Osquiguil, M. Maenhoudt, S. Libbrecht, Z. X. Gao, and Y. Bruynseraede. *Physical Review B*, 47:5512, 1993.

[178] P. Xiong, G. Xiao, X. D. Wu. *Physical Review B*, 47:5516, 1993.

[179] L. B. Ioffe and A. J. Millis. *Physical Review B*, 58:11631, 1998.

[180] Bao-Qiang Cao, Chang-De Gong, Jun Li, and Yong-Jun Liu. *Physical Review B*, 62:15237, 2000.

[181] Kouji Segawa and Yoichi Ando. *Physical Review B*, 69:104521 2004.

[182] C. Ulrich, G. Ghiringhelli, A. Piazzalunga, L. Braicovich, N. B. Brookes, H. Roth, T. Lorenz, and B. Keimer. *Physical Review B*, 77:113102 2008.

[183] M. Abbate et al. *Physical Review B*, 44:5419 1991.

[184] T. Higuchi. *Physics of Solid State Ionics*, India: Research Signpost, 2006.

Appendix A

Ligand Weight Analysis

XAS measurements probe the unoccupied density states, and peak intensities are directly related to the number of unoccupied states involved. The dominant contribution to the unoccupied density of states in YBCO remains transitions from Cu(2) of $3d_{x^2-y^2}$ orbital character (WL), however a portion of this spectral weight is redistributed to the ZR shoulder, which is a doping dependent features [44]. Dopant holes form on neighboring oxygen sites instead of Cu in the planes, since the creation of Cu^{3+} requires paying an 8 eV coulomb penalty (charge-transfer model). Due to covalancy between Cu d and O p orbitals, the hole on a neighboring oxygen site will interact strongly with the localized hole in the Cu(2) $3d_{x^2-y^2}$ orbital leading to the ZR line. Subsequently the ZR peak makes up a greater proportion of the area under the L_3 edge at higher oxygen (hole) concentrations. The total spectral weight of the WL and ZR peaks is approximately constant providing a means of normalization. Hence we can successfully track changes in hole-content within the CuO_2 planes and in an analogous way for the CuO_3 chains.

The first step was to develop a reliable measurement method of the Zhang-Rice contribution to the L edge absorption spectra. The area under the L_3 edge includes contributions from mainly the WL and ZR as shown in Figure 1.8(a). Two smaller peaks need to be considered as well. The peaks near 934.0 and 936.5 eV stem from monovalent Cu(1) in the chains, and the former is present in most monovalent Cu compounds [153]. All four peaks were fitted with Voigt functions. Before fitting the data, the post edge was normalized to unity, and then the edge jump was subtracted using an arcsin function. The first derivate of the spectra was used to identify E_0. The ligand hole weight
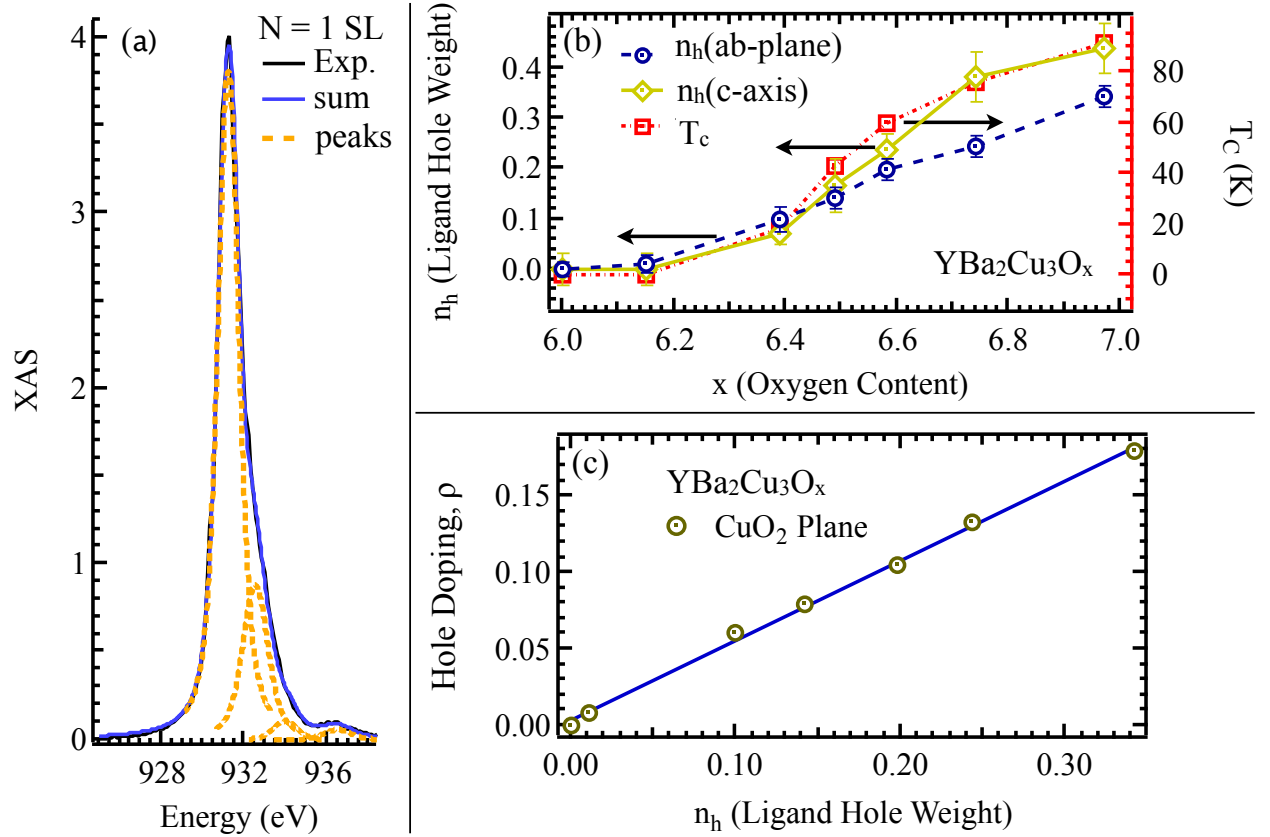
Figure A.1: **Ligand Weight Analysis.** **(a)** Cu L_3 edge ab-plane polarized XAS (black curve) for the $N = 1$ superlattice. Post edge normalized to unity, and the edge-jump has been removed. Peaks were fitted with Voigt functions (dashed curve). The sum of the fit is graphed in blue. **(b)** Ligand hole weight and T_c for $YBa_2Cu_3O_7$ single crystals from reference [44]. **(c)** Hole-doping versus ligand hole weight for single crystals.

n_h was calculated according to equation 1.2, where A_{WL} and A_{ZR} represent the areas under the

$$n_h = \frac{A_{ZR}}{A_{WL} + A_{ZR}} \tag{A.1}$$

WL and ZR peaks, respectively. While n_h alone provides a relative measure to judge hole density

[145], further analysis establishes a metric for hole doping.

The ligand hole weight was converted into a metric of ab-plane hole content by applying the

above analysis to suitable reference samples. As shown in figure 1.8(b), n_h has been calculated

for the series of single crystals in reference [44]. There is a strong relationship between both the

in-plane and c-axis ligand hole weight and T_c (see Figure 1.8(b)). From T_c, the CuO$_2$ plane doping content of the single crystals has been computed using a YBa$_2$Cu$_3$O$_x$ specific variation on equation 1.3 [142].

$$T_c/T_{c,max} = 1 - 82.6(p - 0.16)^2 \qquad \text{(A.2)}$$

In Figure 1.8(c), the ab-plane hole-doping has been plotted against n_h, and their relationship is well approximated to first order by a linear fit, where $p \simeq n_h/2$.

Appendix B
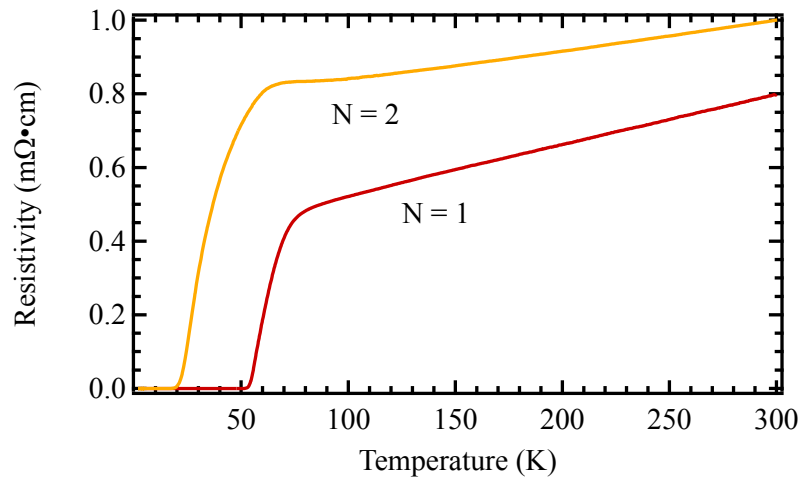
Supplemental Figures

Figure B.1:   **Electronic transport measurements with linear plots.** Four point probe electrical transport measurements of superlattices with $N = 1, 2$. T_0 shifts from 202 to 132 K as N increases from 1 to 2. Changes in normal state transport properties are consistent with decreased carrier concentration.
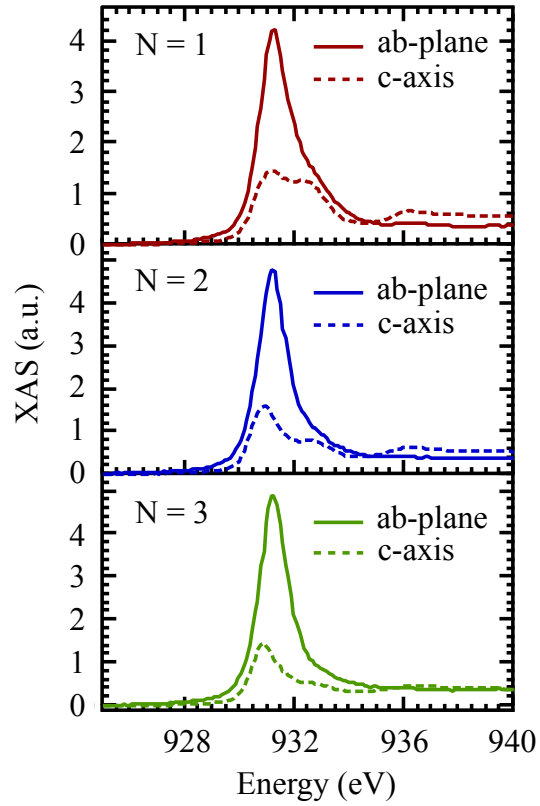
Figure B.2: **Cu XLD with post edge normalization.** Cu L_3 edge XLD for the $N = 1, 2, 3$ superlattices. The post edge has been normalized unity. The c-axis spectra were extrapolated using: $I(\theta) = I(0°)cos^2(\theta) + I(90°)sin^2(\theta)$.